SOVIET ATOMIC ENERGY

АТОМНАЯ ЭНЕРГИЯ

(ATOMNAYA ÉNERGIYA)

TRANSLATED FROM RUSSIAN

$\frac{c}{b}$ CONSULTANTS BUREAU, NEW YORK

SOVIET ATOMIC ENERGY

Soviet Atomic Energy is abstracted or indexed in Chemical Abstracts, Chemical Titles, Pollution Abstracts, Science, Research Abstracts, Parts A and B, Safety Science Abstracts Journal, Current Contents, Energy Research Abstracts, and Engineering Index.

CONSULTANTS BUREAU, NEW YORK AND LONDON

SOVIET ATOMIC ENERGY

Volume 54, Number 1   January, 1983

CONTENTS

Engl./Russ.

CONTENTS

TEMPORAL EVOLUTION OF THE NEUTRON SPECTRUM IN A COHERENTLY SCATTERING
CRYSTALLINE MODERATOR OF SMALL SIZE

Sh. Kenzhebaev

UDC 621.039.51.12

The damping constant λ_0 of the neutron distribution from a pulse source in limited volumes (assemblies) of uniform material at an asymptotically long time t after a neutron pulse cannot exceed [1]

$$\lambda^* = \min w(v) = \lim_{v \to 0} w(v),$$

where w(v) is the total probability of interaction of neutrons with velocity v in the material. For semicrystalline coherently scattering moderators this limit is attained in comparatively large assemblies, e.g., for beryllium with a geometric parameter $B^2 = B^{*2} \equiv 0.03$ cm^{-2}. At the same time, a practically exponential decay of the neutron flux with an effective constant $\lambda \approx (2-3)\lambda^*$ has been observed experimentally [2] in moderator assemblies of significantly smaller sizes.

A number of papers [3-17] have been devoted to the experimental and theoretical investigation of the evolution of neutrons in beryllium, in which it has been noted, e.g., that not a true asymptotic neutron distribution was observed [2], but some intermediate relatively stable distribution which has received the designation of "quasiasymptotic." In particular, it has been shown experimentally [5] that in a beryllium assembly with $B^2 = 0.075$ cm^{-2} the neutron spectrum has still not become asymptotic at t = 649 μsec.

The onset of the quasiasymptotic distribution and its subsequent transition to an asymptotic distribution has been discussed theoretically in [12, 14, 16, 17]. In particular, it has been shown [17] that in beryllium assemblies with geometric parameters $B^2 > 2B^{*2}$ a stable quasiasymptotic distribution is not established in general. This phenomenon has been investigated experimentally and calculated theoretically in [18]. The calculation was done by the multigroup method using a realistic model of the scattering kernel. The experimental decay rate of the quasiasymptotic distribution turned out to be appreciably lower than the theoretical rate. One of the possible reasons for this may be associated with not taking sufficiently accurate account, in the multigroup calculations, of the region of extremely small velocities (e.g., see [18]), at which the singular part of the asymptotic spectrum is formed.

This question has been investigated in this paper on the basis of the simple model of the scattering kernel of Corngold–Durgun [12], who propose an analytic investigation of the neutron spectrum as v → 0. This model satisfies the principle of detailed equilibrium and gives a correct total scattering cross section.

Statement of the Problem. We shall discuss the temporal evolution of the velocity distribution of the neutrons in a small assembly ($B^2 > B^{*2}$) of beryllium generated by a pulse source. After cessation of the pulse, the neutron distribution N(v, t) is described in the diffusion approximation by the equation

$$\left(\frac{\partial}{\partial t} + \hat{A}\right) N(v, t) = 0; \qquad -\int_0^\infty w_s(v' \to v) N(v', t)\, dv';$$

$$\hat{A} N(v, t) \equiv [w(v) + D(v) B^2] N(v, t)\, w(v) = w_a(v) + w_{in}(v) + w_{el}(v), \tag{1}$$

where $w_a(v)$ = const, $w_{in}(v)$, and $w_{el}(v)$ are the probabilities of absorption, inelastic, and elastic scattering, respectively; D(v), diffusion coefficient of the neutron (in the general case $w_{el}(v)$ and D(v) are nonmonotonic functions with a finite number of bounded discontinuities); and $w_s(v' \to v)$, scattering kernel — the probability of the fact that a neutron with

1

velocity v' falls into a unit velocity interval near v per unit time as a result of collisions with moderator nuclei.

Following Corngold and Durgun [12], we represent the scattering kernel of Eq. (1) in the form

$$w_s(v' \to v) = bw_{ln}(v) w_{ln}(v') M(v) + w_{el}(v) \delta(v'-v),$$ (2)

where $b^{-1} = \int_0^\infty w_{ln}(v) M(v) dv$, $M(v) = 4/\sqrt{\pi} v^2 \times \exp(-v^2)$; $v = \sqrt{E/kT}$.

We used the inelastic scattering and transport cross sections from [19] in the calculations, which describe completely satisfactorily the interaction of neutrons in beryllium both above and below the Bragg limit.

We solved Eq. (1) by the time-step method [20-22]. To this end it was rewritten with the expression (2) taken into account in the form

$$N(v, t+\Delta t) = \{1 - \Delta t [w_{ln}(v) + D(v) B^2]\} N(v, t) + \Delta t b w_{ln}(v) M(v) \int_0^\infty w_{ln}(v') N(v', t) dv'.$$ (3)

We determined the effective damping constant $\lambda(t)$ from the formula

$$\lambda(t) = -dN(t)/N(t) dt,$$

where $N(t) = \int_0^\infty N(v, t) dv$.

We did the calculations for B^2 = 0.075, 0.076, and 0.101 cm^{-2}. We took the following as the initial velocity distribution of the neutrons:

the experimental spectrum of **Gaertner et al.** [5] at t = 176 μsec in a beryllium assembly with B^2 = 0.075 cm^{-2}; and

a Maxwellian distribution with temperature 600°K and B^2 = 0.076 and 0.101 cm^{-2} (beryllium assemblies with dimensions of 15 × 19 × 20 and 15 × 15 × 15 cm). The steps in t and v were chosen equal to Δt = 1 μsec and $\Delta v = 0.05 v_T$ for $0 \leqslant v \leqslant 3.5$ where $v_T = \sqrt{2kT/m}$.

Comparison of the Theory with Experiment and Discussion of the Results. The results obtained are presented in Figs. 1-3, correspondingly, at relatively short and long times after a neutron pulse. The measured spectra of Gaertner et al. [5] and the computational results based on multigroup diffusion theory produced by Ghatak et al. [23] using the first term of the expansion of the scattering kernel of Plachek and the transport cross section taken from Goyal's research [24]* are presented in Fig. 1.

It is evident from Fig. 1 that on the whole, notwithstanding the rather complicated form of the spectra at a relatively short time after a pulse, the calculations performed in this paper using a dimple model of the scattering kernel are in satisfactory agreement both with experiment and with theoretical calculations performed using a more realistic model. The calculations satisfactorily describe the position and amplitude of the maxima and minima of the neutron spectra, which are located at the positions of the maxima and minima of $\sigma_{tr}(E)$, and in particular the fact that as the time increases there occurs an accumulation in the neutron spectrum at an energy corresponding to the maximum peak of the elastic scattering cross section. Such agreement is evidently explained by the use of the actual total inelastic scattering cross section and the transport cross section.

The accumulation of neutrons in the region of small energies (in the so-called Corngold "trap") predominates at large times in accordance with the prediction of theory [16] that in a small moderator volume an energy spectrum of neutrons asymptotic in the time has a singularity at E = 0 of the δ-function type. This is evident from Fig. 2 for B^2 = 0.101 cm^{-2}.

However, one should note that the shape of the neutron distribution in this energy region, according to our calculations and the calculations of Japanese physicists [18] (Fig. 3),

---

*Since the spectra in [5] were normalized arbitrarily, their normalization was chosen from the condition that they agree with experiment at E = 500°K for comparison with our results.

2
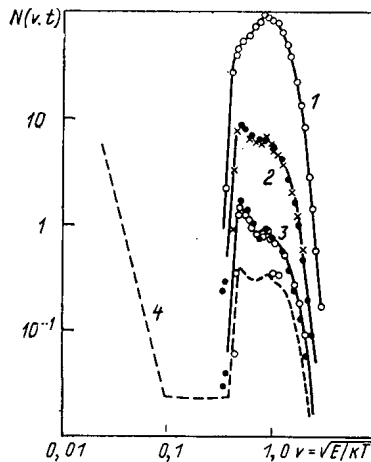
Fig. 1

Fig. 2

Fig. 1. Time-dependent neutron spectra at a short time after a pulse in a beryllium assembly with $B^2 = 0.075$ cm^{-2} at t = 176 (1), 378 (2), 477 (3), and ∞ (4) μsec; O, ×) experiment of [5]; -----, ———) calculation of [23]; ●) calculation of the present paper.
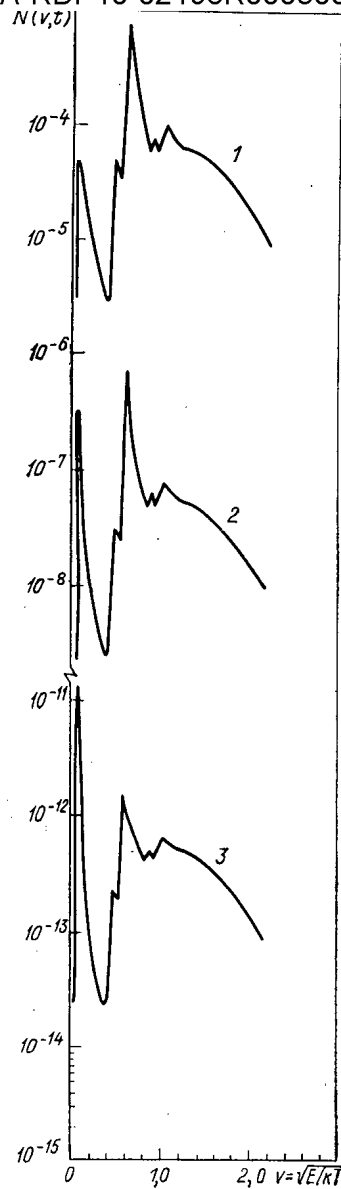
Fig. 2. Time-dependent neutron spectra at a long time after a pulse in a beryllium assembly with $B^2 = 0.101$ cm^{-2}, based on the calculations of the present paper at t = 1 (1), 2 (2), and 4 (3) msec.

differs appreciably. This may be related both to the inaccuracy of the multigroup calculation in [18] and to the approximate nature of the scattering kernel used in our calculation. Notwithstanding this discrepancy, the time dependence of the effective damping constant $\lambda(t)$ of the neutron flux according to our calculations and the calculations of the Japanese physicists [18] proved to be similar. This is evident from Fig. 4, in which the results of both calculations are presented as well as the experimental data of [18]. It is evident that according to the calculations and the experiment with $B^2 = 0.076$ cm^{-2} there exists a rather broad time interval after a pulse during which $\lambda(t) \approx$ const $> \lambda^*$. In this interval an almost stable quasiasymptotic neutron spectrum is formed. At large times the quasiasymptotic distribution decays, changing into a purely asymptotic one, and $\lambda(t)$ slowly decreases, tending to λ^* — its own limit.

3
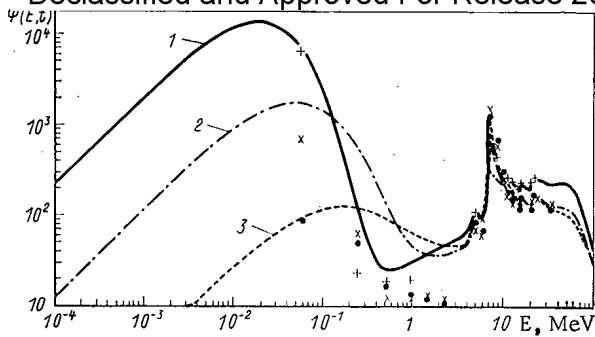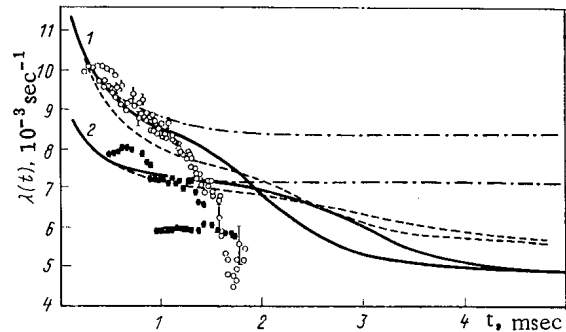
Fig. 3   Fig. 4

Fig. 3. Comparison of the time-dependent neutron spectra at a long time after a pulse in a beryllium assembly with $B^2 = 0.101$ cm^{-2} at t = 4 (1), 2 (2), and 1 (3) msec: -----, -•-•-•-, ———) calculation of [18]; ●, ×, +) calculation of the present paper (both calculations are normalized at E = 0.049 eV).

Fig. 4. Time dependence of the effective damping constant of the neutron flux in comparison with experiment (○,●) and calculation [18] for beryllium assemblies with the dimensions 15 × 15 × 15 (1) and 15 × 19 × 20 (2) cm: ———, -•-•-•-) calculation of [18]; -----) calculation of the present paper.

The results obtained show that taking correct account of only the behavior of the neutron distribution in the energy region close to zero evidently can scarcely explain the observed discrepancy between the theoretical and experimental decay rates of the quasiasymptotic neutron spectrum. This discrepancy is most likely explained by the incorrectness of the diffusion approximation to describe the nonsteady transport of neutrons in small assemblies of beryllium below the Bragg limit.

LITERATURE CITED

1. N. Corngold, Nucl. Sci. Eng., 19, 80 (1964).
2. I. F. Zhezherun, At. Energ., 16, No. 3, 224 (1964).
3. E. Silver, in: Proc. BNL Conf. on Neutron Thermalization, BNL-719, Vol. 3, 981 (1962).
4. R. Fullwood et al., Nucl. Sci. Eng., 18, 138 (1964).
5. R. Gaertner et al., in: Pulsed Neutron Research, Vol. 1, IAEA, Vienna (1965), p. 483.
6. V. I. Mostovoi et al., ibid., 1, 623 (1965).
7. L. Kothari, Nucl. Sci. Eng., 23, 402 (1965).
8. A. Ghatak et al., J. Nucl. Energy, A/B, 19, 679 (1965).
9. I. Goyal et al., J. Nucl. Energy, A/B, 20, 667 (1966).
10. J. Wood, J. Nucl. Energy, A/B, 20, 649 (1966).
11. R. Lee and P. Daitch, Nucl. Sci. Eng., 28, 247 (1967).
12. N. Corngold and K. Durgun, Nucl. Sci. Eng., 29, 354 (1967).
13. J. Wood, J. Nucl. Energy, 22, 525 (1968).
14. M. V. Kazarnovskii et al., in: Proc. Symp. on Neutron Thermalization and Reactor Spectra, Vol. 2, IAEA, Vienna (1968), p. 331.
15. I. F. Zhezherun, ibid., p. 379.
16. M. V. Kazarnovskii et al., in: Theoretical and Experimental Problems of Nonsteady Neutron Transport [in Russian], Atomizdat, Moscow (1972), p. 46.
17. R. Conn and N. Corngold, Nucl. Sci. Eng., 37, 85, 94 (1969).
18. O. Aizawa et al., Nucl. Sci. Eng., 50, 38 (1973).
19. R. Bhandari, J. Nucl. Energy, 6, 104 (1957).
20. E. Barnard et al., in: Proc. Brookhaven Conf. on Neutron Thermalization, Vol. 3, 805 (1962).
21. M. Ohanian and P. Daitch, Nucl. Sci. Eng., 19, 343 (1964).
22. A. Ghatak and H. Honeck, Nucl. Sci. Eng., 21, 227 (1965).
23. A. Ghatak et al., in: Proc. Symp. on Neutron Thermalization and Reactor Spectra, Vol. 1, IAEA, Vienna (1968), p. 223.
24. I. Goyal, J. Nucl. Energy, A/B, 19, 103 (1965).

4

TRANSFER AND DEPOSITION OF RADIOACTIVE NUCLIDES IN A CONVECTION FLOW OF SODIUM

A. S. Zhilkin, A. P. Kondrashov, E. S. Kononov,   UDC 621.039.553.36
A. A. Kutuzov, and O. V. Starkov

The problem of the mass transfer of radioactive corrosion products in a sodium circuit has been revealed and finally formulated within the last decade. If the reactor operates with pressurized fuel elements, then the radiation environment during maintenance operations is determined by the radioactivity of the steel corrosion products. The radioactivity of ^{54}Mn is predominant for all operating fast reactors. The ^{60}Co radioactivity also makes a significant contribution to the dose intensity in the vicinity of the plant of the primary circuit.

For such fission products as cesium and iodine, various means of purification have been developed and introduced, but at the present time it is not exactly clear how to localize or remove the corrosion products from the circuit. It should be mentioned that considerable attention is being paid in the Soviet Union and abroad to this problem, and investigations are being conducted in loops and reactors in order to study the mass transfer process and methods of purifiying the primary circuit of the reactor from steel corrosion products.

A procedure and the results of experiments on the mass transfer of manganese and cobalt in a convection sodium loop (CL) are described in the present paper. The results are compared with the results in other papers.

INVESTIGATIONAL PROCEDURE

A diagram of the convection loop designed for studying the mass transfer in sodium of the radioactive corrosion products ^{54}Mn and ^{60}Co is shown in Fig. 1. Two experiments with ^{54}Mn and ^{60}Co were conducted (Table 1). Each experiment consisted of two stages: in the first stage, a radioactive source was installed in the loop circuit; in the second stage, the source was removed, the loop was operated without the source, and the redistribution of these isotopes throughout the loop circuit was recorded.

The sources were prepared in the following way. Specified portions of solutions of manganese and cobalt chlorides, containing ^{54}Mn and ^{60}Co, were applied to plates of stainless steel and nickel with a size of $30 \times 10 \times 0.5$ mm. Diffusion annealing of these plates, coupled in pairs by the active sides, led to penetration into them of manganese and cobalt to a depth of ~10 μm.

In order to study the dynamics of the removal of manganese and cobalt from the source in sodium, and their deposition in the circuit during operation of the loop, the activity of the source and the deposits of manganese and cobalt were measured in individual sections of the circuit, including the SOCT. After shutting down the loop, the distribution of manganese and cobalt over the length of the circuit, and also their content in samples of sodium, were determined in detail. A γ-emission spectrometer, based on a NaI(Tl) scintillator with a size of 40×40 mm, was used for the measurements. The total error of the measured quantities amounted to 10–15%.

An important characteristic of the deposition and erosion processes in sodium circuits is the content of oxygen in the sodium. In the experiments being described, it was estimated starting from the temperature of the coldest section of the circuit, the SOCT, and the solubility of oxygen in the sodium. For the first and second experiments, it amounted to 12.0 and $6.3 \cdot 10^{-6}$, respectively.

The results of the experiments are given with a correction for the radioactive decay of ^{54}Mn and ^{60}Co. Nonlinear effects in the time dependences can be caused by both a change of

TABLE 1. Conditions for Conducting the Experiments

Conditions	First experiment (^{54}Mn and ^{60}Co in stainless steel)	Second experiment (^{54}Mn in nickel)
Temperature at heater outlet, ℃	700	700
Temperature drop over length of the circuit, ℃	165	160
Protective gas	Argon	Argon
Duration of experiment with source, h	954	1536
Duration of experiment without source, h	1360	1056
Material of loop pipeline	12Kh18N10T	12Kh18N10T
Sodium flow velocity, m/sec	0,0300	0,0300
Loss of source activity, MBq	3,1100 (^{60}Co)	0,7930 (^{54}Mn)
Volume of sodium (total), m^3	0,0030	0,0022
Volume of sodium in sodium oxide cold trap (SOCT), m^3	0,0009	0,0001
Volume of sodium in compensation tank, m^3	0,0010	0,0010
Total length of loop circuit pipeline, m	3,5000	3,5000
Diameter of pipeline, m	0,0200	0,0200

Fig. 1

Fig. 2
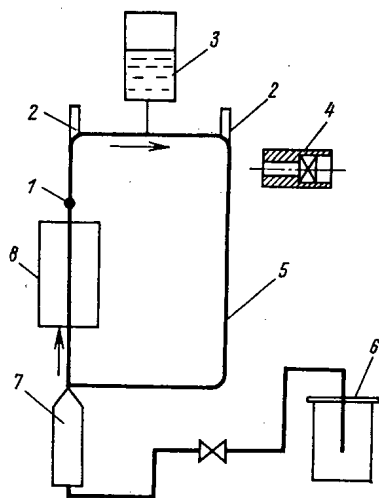
Fig. 1. Diagram of the convection loop: 1) source; 2) hermetic valve for inserting the source and the sample-observers into the loop circuit; 3) compensation tank; 4) detector with lead shielding; 5) loop circuit; 6) overflow tank; 7) sodium oxide cold trap; 8) heater.
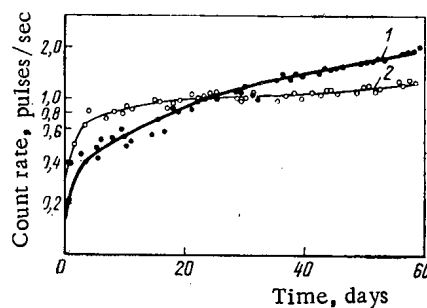
Fig. 2. Dependence of variation of ^{54}Mn deposition on the time at a point at a distance of 0.85 m from the source (1) and in the SOCT (2) for the second experiment (with source).

the rate of removal of the nuclides from the source, and by their redistribution as a result of erosion of the deposits from the walls of the circuit.

RESULTS OF THE EXPERIMENTS AND THEIR DISCUSSION

The rate of deposition of manganese decreases as a function of time (Fig. 2). The time derivative of the buildup curve is large in the initial period of the experiment (250–1000 h),

6

TABLE 2. Relative Content of ^{54}Mn in Different Structural Components of the Convection Sodium Loop (CL) when Sodium is Drained Off

Content of ^{54}Mn	First experiment	Second experiment
Total	1	1
On the surface of the pipeline	0,23	0,62
On the surface of the compensation tank	0,16 *	0,019
in the SOCT	0,05	0,02
In the sodium overflow tank	0,16	0,27
In other structural components	Not measured	0,095

*In this experiment a grid of stainless steel was installed in the compensation tank.
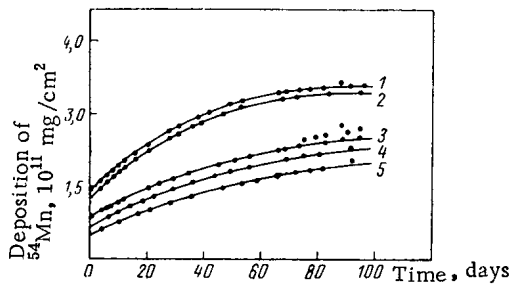
Fig. 3

Fig. 4

Fig. 3. Dependence of the variation of ^{54}Mn deposition on the time, for the conditions of the experiments described in [1] (T = 650°C): 1-5) points at different distances from the source.
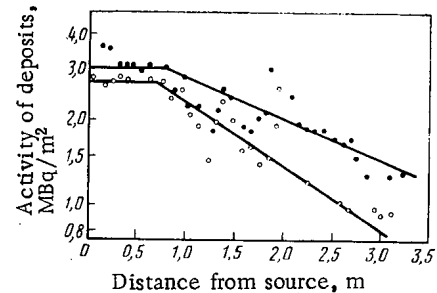
Fig. 4. Distribution of ^{60}Co deposits throughout the convection sodium (CL) circuit (first experiment with source (●) and without source (○)).

but tends to a constant value. The results of the measurements can be described by a parabolic function. A qualitatively similar time dependence of the buildup of ^{54}Mn in the circuit was also observed in other papers [1, 2] (Fig. 3).

The dynamics of the buildup of ^{60}Co in the loop circuit were not investigated in the present paper, but in [2] it was noted that there exists a certain "induction period" of ~1000 h, after which the deposition of cobalt on the walls of the loop circuit increases sharply.

It can be seen from Figs. 4 and 5 that the distribution of ^{54}Mn and ^{60}Co throughout the loop circuit is nonuniform. An increased deposition of manganese is observed in the vicinity of installation of the device for introducing the source and samples into the loop circuit, where the temperature of the wall is lower than in adjacent sections of the circuit. The deposits of cobalt on the walls of the circuit gradually decrease on the whole in the direction of the sodium stream. When the sodium is drained from the loop, 27% of the manganese is removed. The residual quantity of manganese remains in the deposits on the walls of the circuit, the compensation tank, and other components (Table 2).

Knowing the surface area of the circuit and the volume of sodium, the distribution coefficient K can be estimated, which occurs as a constant parameter in the radioactive mass transfer equation for a uniform circuit [3]. For the quasisteady case, this coefficient can be defined as the ratio of the concentration of the isotope being studied on the surface of the loop, to its concentration in the sodium. For the material of the pipeline of the CL (stainless steel), the distribution coefficients of manganese and cobalt amounted to: in the first experiment with the source, 1.6 for ^{54}Mn and 0.9 for ^{60}Co, and without the source, 3.2

7
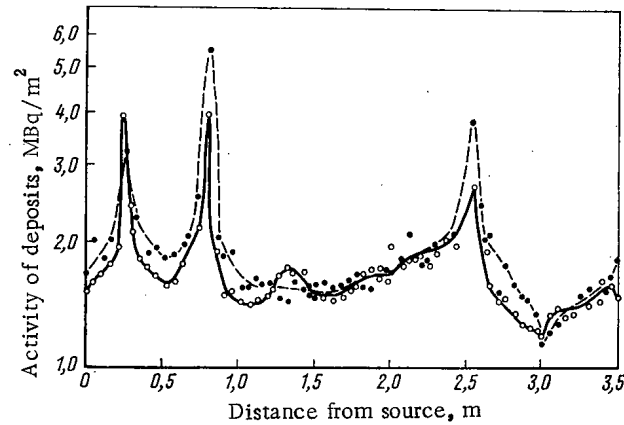
Fig. 5. Distribution of ^{54}Mn deposits through-
out the convection sodium loop (CL) circuit
(second experiment with source (●) and without
source (○)).

for ^{54}Mn and 1.2 for ^{60}Co; in the second experiment with the source, 1.7 for ^{54}Mn, and with-
out the source 5.0 for ^{54}Mn. It can be seen that the value of K for ^{54}Mn is almost independ-
ent of the oxygen concentration in the sodium during operation of the loop without the source.
This, probably, is explained both by the method of preparing the source and by the conditions
of the experiment in the CL. The increase of the distribution coefficient in the case of
operation of the loop without the source, by comparison with the experiment conducted with
the source, is related, apparently, with the fact that with the removal of the sodium from the
loop circuit into the overflow tank, a considerable part of the ^{54}Mn is deposited in the lat-
ter, and the sodium, filling the loop circuit in the experiment without the source, is de-
pleted in this isotope. The increase of K in the second experiment without the source can be
explained by the fact that in this experiment the concentration of ^{54}Mn is less by a factor
of 1.5 than in the first experiment, because of the more intense deposition of ^{54}Mn on the
walls of the overflow tank. The ^{54}Mn distribution coefficient on samples of stainless steel
was measured in [4]. Although the conditions of the experiment were different (the measure-
ments were conducted on the KNK reactor at 200-400°C), the results nevertheless coincide with
those obtained in the present paper.

An analysis of the results obtained in the present paper and in other similar papers
[1, 2, 5, 6] indicates the tendency of the rate of deposition of sodium to increase in the
loop conditions in regions with a negative temperature gradient. Moreover, the manganese is
deposited also immediately behind the source. The cobalt is deposited predominantly immed-
iately behind the source, and then its concentration on the wall decreases, having tended to
a constant value. It was noted in [2] that the distribution of the cobalt deposits along the
length of the loop can be described by an exponential relation. It can be seen from Fig. 4
that the results of the experiment in the conditions of the CL also can be described approx-
imately by an exponent, with the exception of the section of the circuit in the vicinity of
the location of the source, where the distribution of the deposits is almost uniform over the
length of the section.

Consideration of the measurement results in the experiments without the source (Fig. 5)
show that the content of manganese on the wall of the circuit is reduced in the hot section
of the loop but is increased slightly in the cold section. However, variations in the values
of the deposits during operation without the source are small for the CL and, as a rule, do
not exceed 10%. In the compensation tank and the SOCT, increases of the manganese content
were observed by factors of 2.3 and 1.1, respectively.

Thus, the results of the experiments carried out showed the following:

1. Deposits of ^{54}Mn on the walls of the sodium loop depend on the duration of the ex-
periment. In the initial period of the experiment (up to 250-1000 h), the rate of deposition
is large, but then it is reduced to a constant value. Obviously, the redistribution of the
deposits during the experiment depends slightly on the time dependence of the rate of removal
of radioactive nuclides from the source. If this is so, then the behavior of manganese can
be characterized as a diffusion process. In this case, in the initial period of the experi-
ment, the rate of removal of this isotope is large, in consequence of its large concentration

8

gradient at the steel—sodium interface; then with reduction of the concentration gradient, the rate of removal is slowed down. As the experiment shows, the rate of removal of ^{54}Mn from the source with time generally can be stopped, which, obviously, is related with the formation of a depleted layer in which the duration of diffusion of this nuclide is greater than the half-life.

2. Manganese has a tendency to increase the rate of deposition in regions with a negative temperature gradient. At the same time, it is deposited also at the site of location of the source. Cobalt is deposited predominantly immediately beyond the source. Its concentration on the wall later decreases.

The experiments without the source, conducted after the experiments with the source, showed that the manganese content on the wall of the circuit is somewhat less in the hot part of the loop and is increased in the cold part. However, these variations are small and, as a rule, do not exceed 10%. At the same time, increases of the manganese content by factors of 2.3 and 1.1, respectively, were observed in the compensation tank and in the SOCT.

3. The distribution coefficient, determined as the ratio of the concentration of the nuclide on the surface of the loop circuit to its concentration in the sodium, during operation of the loop does not vary with increase of the oxygen concentration in the sodium by a factor of two.

LITERATURE CITED

1. A. Thorley et al., in: Proceedings of the Second International Conference on Liquid Metal Technology in Energy Production, Richland (1980), p. 13-1.
2. J. Newson et al., in: Proceedings of the Second International Conference on Liquid Metal Technology in Energy Production, Richland (1980), p. 17-11.
3. A. S. Zhilkin and I. A. Kuznetsov, in: Radiation Safety and Protection of Nuclear Power Stations [in Russian], No. 5, Atomizdat, Moscow (1981), p. 78.
4. M. Stamm et al., in: Proceedings of the Second International Conference on Liquid Metal Technology in Energy Production, Richland (1980), p. 17-58.
5. W. Brehm et al., "Techniques for studying corrosion and deposition of radioactive materials in sodium loops," in: Data of an International Conference on the Behavior of Fission and Corrosion Products in the Primary Circuit of Fast Reactors [Russian translation], Dimitrovgrad (1975), p. 172.
6. N. Sekiguchi et al., "Behavior of corrosion products from irradiated stainless steel in flowing sodium," in: Data of an International Conference on the Behavior of Fission and Corrosion Products in the Primary Circuit of Fast Reactors [Russian translation], Dimitrovgrad (1975), p. 82.

ANGULAR DISTRIBUTION OF A BROAD BEAM OF FAST ELECTRONS REFLECTED FROM
A SEMIINFINITE MEDIUM IN THE CASE OF GRAZING INCIDENCE

V. S. Remizovich   UDC 539.12.72

When thick layers of a material are irradiated with a flux of fast electrons, a signifi-
cant fraction of the electrons is reflected at the medium. The relative number of reflected
electrons increases substantially with decreasing angle ζ_0 between the velocity vector of the
incident electrons and the target surface.

But the existing theories of electron albedo [1-3] describe grazing incidence only inade-
quately when $\zeta_0 \ll 1$. The reason is that the main assumption on which the above work has been
based implies that the main contribution to reflection is provided by single scattering at
relatively large angles $\vartheta \gtrsim 1$. Multiple scattering of electrons before their entry into the
medium and before large-angle scattering events, as well as after such scattering and before
the backward exit of an electron from the material, were completely disregarded in [1] and
were considered second-order processes in [2, 3], with the processes "smearing out" the over-
all pattern of angular scattering and energy scattering of the reflected electrons. It is
quite clear that in "grazing" incidence of a particle beam on the surface of a material, the
multiple scattering is not a second-order process at $\zeta_0 \ll 1$, but is the main process, because
in this case the greater portion of the electrons can be reflected from the material without a
single large-angle scattering event. The greater part of the electrons can be simply reflec-
ted by multiple scattering under relatively small angles. Disregarding this fact implies a
substantial disagreement between the theory [2, 3] and the experimental results [4]. We con-
sider below the problem of calculating the angular distribution of reflected electrons in the
irradiation of a semiinfinite inhomogeneous target medium by a broad flux of fast monoenerge-
tic electrons propagating in a single direction. We restrict our considerations to the case
of purely elastic scattering. This situation is encountered in reality when a large fraction
of the electrons has time to leave the medium before losing some noticeable part of the ini-
tial energy, i.e., when $w \sim 1$ applies for the total reflection coefficient.

Assume that a broad monoenergetic beam of fast electrons is incident under a small angle
ζ_0 onto the surface of a plane layer of an inhomogeneous material. Assume the z axis to be
parallel to the normal to the surface and the XOZ plane to coincide with the velocity vector
of the incident particles. The direction of particle motion is defined by the angles ζ and
φ; ζ denotes the angle between the velocity vector and the XOY plane and φ denotes the azi-
muthal angle, i.e., the angle between the velocity vector and XOZ plane. Values $\zeta > 0$ corres-
pond to particles moving into the material, whereas values $\zeta < 0$ correspond to particles mov-
ing in the opposite direction. In our case of grazing incidence, the considerations can be
restricted to the small-angle approximation of [5, 6] when we assume that $|\zeta|$ and $|\varphi| \ll 1$.
In this approximation the projections of the velocity unit vector $\mathbf{\Omega}$ are related to the angles
ζ and φ by the formulas $\Omega_x = \cos \zeta \cos \varphi \approx 1$; $\Omega_y = \cos \zeta \sin \varphi \approx \varphi$; $\Omega_z = \sin \zeta \approx \zeta$; the angle
of single scattering from the state $\mathbf{\Omega}(\zeta; \varphi)$ into the state $\mathbf{\Omega}'(\zeta'; \varphi')$ is given by the formula
$\vartheta'' = \arccos (\mathbf{\Omega}', \mathbf{\Omega}) \approx \sqrt{(\zeta' - \zeta)^2 + (\varphi' - \varphi)^2}$. In the case of fast electrons, the probability
of single scattering is given by the following formula of [7]:

$$I(\mathbf{\Omega}' \to \mathbf{\Omega}) = \frac{1}{\sigma} \frac{d\sigma}{d\Omega} \approx \frac{\vartheta_{\text{eff}}^2}{\pi (\vartheta_{\text{eff}}^2 + (\zeta' - \zeta)^2 + (\varphi' - \varphi)^2)^2} \; ; \; \vartheta_{\text{eff}}^2 \approx \frac{1.2 \cdot 10^{-5} Z^{2/3}}{E_0 (1 + E_0)} , \tag{1}$$

where ϑ_{eff} denotes the "effective" angle of single scattering, related to the Moliere shield-
ing parameter by the formula $\vartheta_{\text{eff}}^2 = 4\eta$; Z denotes the atomic number of the material of the
scatterer; and E_0 denotes the electron energy (MeV).

In view of the above considerations, we obtain the following form of the transfer equa-
tion of the electron flux density $N(\tau, \zeta, \varphi)$ at the depth $\tau = \sigma \int_0^z n_0(z') \, dz'$ (where τ is the

---

"optical depth, σ, total cross section of elastic scattering, and n_0, density of the material at the depth z):

$$\zeta \frac{\partial N}{\partial \tau} \frac{\vartheta_{eff}^2}{\pi} \int\limits_{-\infty}^{\infty} d\zeta' \int\limits_{-\infty}^{\infty} d\varphi' \frac{N(\tau; \zeta'; \varphi') - N(\tau; \zeta; \varphi)}{[\vartheta_{eff}^2 + (\zeta' - \zeta)^2 + (\varphi' - \varphi^2)]^2} \cdot \qquad (2)$$

Additional conditions to be satisfied by transfer equation (2) are

$$N(\tau = 0; \zeta > 0; \varphi) = N_0 \delta(\zeta - \zeta_0)\, \delta(\varphi); \quad N(\tau; \zeta; \varphi) = 0 \text{ if } \tau \to \infty; \zeta^2 + \varphi^2 \to \infty, \qquad (3)$$

where N_0 denotes the particle flux density in the incident beam. The second of conditions (3) is the requirement that the solution must remain finite in the depth and over the angles.

The angular distribution of the particles reflected at the material (for such particles the angle is $\zeta < 0$) is described with the reflection function $S(|\zeta|, \varphi; \zeta_0)$, which is related to the particle flux density at the boundary of the material through the formula

$$N(\tau = 0; \zeta < 0, \varphi) = N_0 \frac{S(|\zeta|, \varphi; \zeta_0)}{|\zeta|}. \qquad (4)$$

There $N_0 S(|\zeta|, \varphi; \zeta_0)$ determines the number of particles leaving a unit surface area of the medium per unit time in the angular interval $|\zeta| - |\zeta| + d|\zeta|; \varphi - \varphi + d\varphi$. Since the number of particles incident per unit time on a unit surface area of the medium is $\zeta_0 N_0$, the differential reflection coefficient d^2w is associated with the reflection function by the simple formula $d^2w = \zeta_0^{-1} S d|\zeta| d\varphi$. The reflection function S fully describes the angular spectrum of the reflected electrons and must be determined during the solution of the problem.

Since the transfer equation is linear, in the case of a semiinfinite homogeneous scattering medium the flux of electrons moving toward the boundary, i.e., for $\zeta < 0$, is at any depth τ a linear functional of the flux of particles moving into the bulk of the medium, i.e., for particles with $\zeta > 0$. The kernel of the functional must be independent of depth:

$$|\zeta| N(\tau; -|\zeta|; \varphi) = \int\limits_{-\infty}^{\infty} d\varphi' \int\limits_0^{\infty} d\zeta' S(|\zeta|; \varphi' - \varphi; \zeta') N(\tau; \zeta'; \varphi'). \qquad (5)$$

We took into consideration that after introducing the optical depth τ in place of z, Eq. (2) does not differ from the corresponding equation for a homogeneous medium. By assuming $\tau = 0$ in Eq. (5) and recalling the definition given in Eq. (4), we observe that the kernel of the functional (5) coincides precisely with the reflection function if $\zeta' = \zeta_0$ and $\varphi' = 0$. Therefore, the kernel is denoted by the same letter S.

Important in our subsequent considerations will be the fact that the general solution of transfer equation (2) can be easily found in the case under consideration if the Fourier transform over the angular variables ζ and φ is used. A solution of transfer equation (2), which is limited over both the depth τ and the angular variables, has the form

$$N(\tau; \zeta; \varphi) = \frac{1}{(2\pi)^2} \int\limits_0^{\infty} \lambda C(\lambda)\, d\lambda \int\limits_{-\infty}^{\infty} d\omega\, dp \exp\left\{ -\lambda \frac{\tau}{\vartheta_{eff}} + i\omega \frac{\zeta}{\vartheta_{eff}} + ip \frac{\varphi}{\vartheta_{eff}} - \frac{i}{\lambda} \int\limits_0^{\infty} dq \left[1 - \sqrt{q^2 + p^2}\, K_1(\sqrt{q^2 + p^2}) \right] \right\}, \qquad (6)$$

where K_1 denotes the MacDonald function. The unknown coefficients $C(\lambda)$ can be determined from the first condition (3), which defines the flux of electrons incident on the boundary of the medium. Having determined $C(\lambda)$ with Eq. (6), the angular distribution of the particles at any depth τ can be calculated. But when the angular distribution only of the reflected particles is to be determined in the solution of the albedo problem, it is more convenient and simpler to immediately solve Eq. (5) for the reflection function.

Since the calculation of the total angular distribution of the reflected electrons over the polar angle ξ and the azimuthal angle φ is an extremely complicated and so far unsolved problem, we restrict our considerations to the much simpler problem of calculating the angular distribution of the reflected particles $S(|\zeta|; \zeta_0)$ only over the polar angle $|\zeta|$:

$$S(|\zeta|; \zeta_0) = \int\limits_{-\infty}^{\infty} S(|\zeta|; \varphi; \zeta_0)\, d\varphi. \qquad (7)$$

11

By integrating Eq. (5) over φ and recalling the explicit form of the general solution of transfer equation (6), and, furthermore, taking into account that Eq. (5) is valid for any depth τ, we obtain the following integral equation for determining the reflection function $S(|\zeta|; \zeta_0)$:

$$|\zeta| \int_0^\infty d\omega \cos\left\{\omega \frac{|\zeta|}{\vartheta_{eff}} + \frac{1}{\lambda} \int_0^\omega [1 - qK_1(q) \, dq\right\} = \int_0^\infty d\zeta' S(|\zeta|; \zeta') \int_0^\infty d\omega \cos\left\{\omega \frac{\zeta'}{\vartheta_{eff}} - \frac{1}{\lambda} \int_0^\infty [1 - qK_1(q)] \, dq\right\} ; \ (\lambda \geqslant 0). \ (8)$$

Let us note as an important point that although the fundamental relationship (5) (which is also the basis of the "invariant inclusion method") was used in deriving Eq. (8) for the reflection function S, the equation obtained is linear, whereas the analogous equation for the reflection function (equation obtained with the invariant inclusion method) is significantly nonlinear [1, 7].

When we proceed to the solution of Eq. (8), we note that in the case of electrons with an energy of tens of kilovolts and more, the effective angles of single scattering are extremely small. For example, we obtain from Eq. (1) for 100 keV electrons that $\vartheta_{eff} \approx 10^{-2}$ for Z = 1 and $\vartheta_{eff} \approx 4 \cdot 10^{-2}$ for Z = 64. When the particle energy increases, the ϑ_{eff} values decrease even further. Therefore, when the grazing angle ζ_0 is such that the inequality

$$1 \gg \zeta_0 \gg \vartheta_{eff} \tag{9}$$

is satisfied, we obtain in the angular range $|\zeta| \sim \zeta_0$ of greatest interest that the effective ω_{eff} values are $\omega_{eff} \ll 1$ and that the function $qK_1(q)$ on both sides of Eq. (8) can be expanded in a series by assuming $qK_1(q) \approx 1 + q^2 (\ln q^2 + 2C - 1)$, where C = 0.577 denotes the Euler constant. We then obtain in the region $\omega_{eff} \lesssim 1$:

$$\int_0^\infty dq [1 - qK_1(q)] \approx \frac{\omega^3}{3} \ln\left(\frac{1.8}{\omega^2}\right) \approx \frac{\omega^3}{3} |\omega|^{-\alpha}, \tag{10}$$

where α denotes an approximation parameter varying in this problem within the interval $0 \leqslant \alpha \leqslant 1$. The particular α values can be determined either by comparing the results of the calculation with experimental results or theoretically by employing some additional concepts which, e.g., can be obtained from the condition that the functions $\omega^3 \ln (1.8/\omega^2)$ and $\omega^{3-\alpha}$ coincide on the average within the interval $0 \leqslant \omega \leqslant 1$. We obtain $\alpha = 4/7$ in this determination. By substituting Eq. (10) into Eq. (8) and introducing the new variables $\omega' = \omega\lambda^{\alpha-3}$; $\varepsilon = 1/\zeta'$; $\zeta' = (1/\vartheta_{eff})\lambda^{1/(3-\alpha)}$, we obtain the following equation for the function $\tilde{S} = \zeta' S (|\zeta|; \zeta')$:

$$\int_0^\infty d\omega \cos\left(\omega\lambda|\zeta| + \frac{1}{3} \omega^{3-\alpha}\right) = \int_0^\infty \frac{d\varepsilon}{\varepsilon} \frac{\tilde{S}(|\zeta|; \varepsilon)}{|\zeta|} \int_0^\infty d\omega \cos\left(\omega \frac{\lambda}{\varepsilon} - \frac{1}{3} \omega^{3-\alpha}\right). \tag{11}$$

Even when the integrals of Eq. (11) are not taken over ω, it turns out that the equation is exactly solved, with the solution being expressed through elementary functions. Indeed, the Melin transform over the variable λ can be used for the solution of the equation [8]. By multiplying both sides of Eq. (11) with $\lambda^{S-1} d\lambda$ and by integrating over λ within the limits $0 \leqslant \lambda \leqslant \infty$ with the aid of the convolution theorem, we obtain an expression for the Melin image of the reflection function $S(|\zeta|; s)$. Then, using the conversion equation (8), we obtain for the reflection function

$$S(|\zeta|; \zeta_0) = \frac{\beta}{\pi} \frac{\sin(\pi\beta)}{2\cos(\pi\beta) - \left[\left(\frac{|\zeta|}{\zeta_0}\right)^\beta + \left(\frac{\zeta_0}{|\zeta|}\right)^\beta\right]} ; \tag{12}$$

$$\beta = 2 \frac{3-\alpha}{4-\alpha}.$$

When α varies from zero to unity, the parameter β varies within the limits $4/3 \leqslant \beta \leqslant 3/2$, i.e., by a total of 11%. Thus, the form of the angular spectrum of the elastically reflected electrons does not very strongly depend upon α. This fact a posteriori justifies to some extent the use of the approximation (10).

Let us note some general properties of our solution represented by Eq. (12):

12
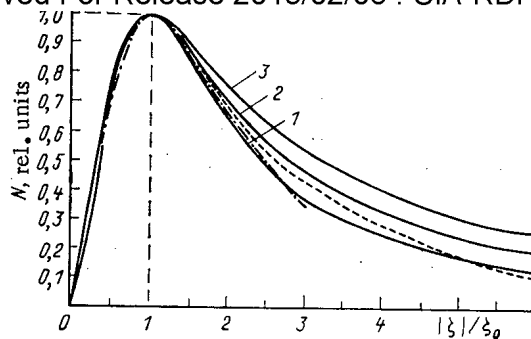
Fig. 1. Angular distribution of reflected electrons: ———)
calculations made with Eq. (14) for the α values 0 (curve 1),
4/7 (curve 2), and 1 (curve 3); -----) result of experiment [4]
on 25 MeV electron scattering at lead with the grazing angle
ζ_0 = 20°; -•-•-•-) the same, grazing angle ζ_0 = 40°.

1. For any α the reflection function of Eq. (12) is normalized by the condition

$$\int_0^\infty S\,(|\zeta|;\ \zeta_0\ \alpha)\,d\,|\zeta| = \zeta_0;\ \text{i.e.,}\ w = \frac{1}{\zeta_0}\int_0^\infty S\,d|\zeta| = 1. \tag{13}$$

This condition expresses the obvious fact that the total reflection coefficient w is equal to unity in the case of purely elastic scattering.

2. Regardless of α, the angular distribution of the reflected electrons has a sharp maximum at $|\zeta|$ = ζ_0, which corresponds to the "mirror" law of reflection. The reflection function maximum is S_{max} = —β/2 ctg πβ/2, so that the formula for the reflection function normalized to unity at its maximum is

$$S_{norm} = \frac{S\,(|\zeta|;\ \zeta_0)}{S\,(\zeta_0;\ \zeta_0)} = \frac{4\sin^2\frac{\pi\beta}{2}}{4\sin^2\frac{\pi\beta}{2} + \left[\left(\frac{|\zeta|}{\zeta_0}\right)^\beta + \left(\frac{\zeta_0}{|\zeta|}\right)^\beta - 2\right]}. \tag{14}$$

3. When we assume in Eq. (12) that α = 0 (β = 3/2), we obtain

$$S\,(|\zeta|;\ \zeta_0;\ \alpha = 0) = \frac{3}{2\pi}\left[\left(\frac{|\zeta|}{\zeta_0}\right)^{3/2} + \left(\frac{\zeta_0}{|\zeta|}\right)^{3/2}\right]^{-1}. \tag{15}$$

Equation (15) coincides exactly with the formula which Firsov obtained in [5] using the diffusion approximation over the angles for calculating the reflection function.

4. We obtain from Eq. (12) for α = 1 (β = 4/3):

$$S\,(|\zeta|;\ \zeta_0;\ \alpha = 1) = \frac{2}{\pi\sqrt{3}}\left[1 + \left(\frac{|\zeta|}{\zeta_0}\right)^{4/3} + \left(\frac{\zeta_0}{|\zeta|}\right)^{4/3}\right]^{-1}. \tag{16}$$

This formula fully agrees with another formula obtained in a later work by the same author [6], which describes angular spectra of elastically scattered particles when the interaction of the particles with the atoms of the material is approximated by a potential inversely proportional to the square of the distance ($U(r) \sim r^{-2}$).

5. The angular spectrum of the reflected particles is independent of the form in which the density of the medium changes as a function of depth in the medium, i.e., it is independent of $n_0(z)$.

6. Formulas (12) and (14), which we obtained for the reflection function, are universal functions of the angular ratio $|\zeta|/\zeta_0$ and are independent of the energy E_0 of the incident electrons for any α and are also independent of the atomic number Z of the material of the scatterer.

All these features of the angular distribution of the reflected electrons are in good agreement with the experimental results [4, 9] for grazing incidence on a thick target. Figure

13

1 shows reflection functions, which are reduced to unity at their maximum and which were cal-
culated with Eq. (14) for various α values of the interval $0 \leqslant \alpha \leqslant 1$. Figure 1 also shows
the results of an experiment of [4] on the angular distribution of reflected electrons over
the polar angle $|\zeta|$; the results were obtained with a lead target at grazing angles $\zeta_0 = 20°$
and $\zeta_0 = 40°$. Though the measurements were made on the plane of incidence of the primary
beam, i.e., for $\varphi = 0$, the spectrum differs only slightly from the spectrum of the reflected
electrons averaged over the azimuthal angle, as noted in [9, 10].

In conclusion, the author thanks O. B. Firsov and M. I. Ryazanov for their interest in
the present work and for useful remarks. The author thanks Sh. A. Shekhmamet'ev for his help
in the calculations and the drafting of the present paper.

LITERATURE CITED

1. R. Dashen, Phys. Rev., 134, No. 4A, 1025 (1964).
2. N. P. Kalashnikov and V. A. Mashinin, Zh. Eksp. Teor. Fiz., 59, No. 6, 2025 (1970).
3. N. P. Kalashnikov and V. A. Mashinin, Zh. Tekh. Fiz., 43, 2229 (1973).
4. V. P. Kovalev, V. V. Gordeev, and V. I. Isaev, At. Energ., 39, No. 3, 215 (1975).
5. O. B. Firsov, Dokl. Akad. Nauk SSSR, 169, No. 6, 1311 (1966).
6. O. B. Firsov, Zh. Tekh. Fiz., 40, 83 (1970).
7. N. P. Kalashnikov, V. S. Remizovich, and M. I. Ryazanov, Collisions of Fast Charged
   Particles in Solids [in Russian], Atomizdat, Moscow (1980).
8. G. Bateman and A. Erdely, Tables of Integral Transforms, McGraw-Hill (1966).
9. I. M. Bronshtein, V. M. Stozharev, and V. P. Pronin, Fiz. Tverd. Tela, 13, No. 11, 3359
   (1971).
10. H. Kanter, Ann. Phys., 20, 144 (1957).

EFFECTS OF RADIAL DIFFUSION ON THE POSSIBLE EROSION OF AN OPEN-TRAP

PLASMA

V. G. Petrov   UDC 621.039.624

In the design of a reactor having an adiabatic trap with double plugs, it is necessary
to overcome the erosion of the lateral surface of the plasma in the end traps by the surround-
ing neutral gas, this surface being parallel to the magnetic field. Preliminary estimates
show that to prevent this phenomenon the gas-atom concentration should not exceed 10^8–10^9 cm^{-3}
[1, 2], which is technically difficult to achieve. In these estimates we have neglected the
transverse diffusion and the thermal conductivity of the plasma, and the condition for stop-
ping the erosion amounted to the number of injected fast neutral particles ionized in the sur-
face layer of the plasma exceeding the loss of ions arising from charge transfer at cold neu-
tral particles in the surrounding gas, while the input of heat with the ionized fast neutral
particles should exceed the energy loss due to ions, electrons, and charge-transfer neutral
particles. The position is serious because the cold neutral particles undergo charge trans-
fer and are ionized in the thin peripheral layer, whereas the source of hot ions is fairly
uniformly distributed throughout the plasma volume. Under these conditions, the plasma may
be disrupted layer by layer beginning with the periphery.

Plasma erosion can evidently be offset by increasing the transverse diffusion coefficient
and thermal conductivity in a sufficiently narrow peripheral region of the plasma in order
that ion and heat balances should occur throughout the region of elevated transport coeffi-
cients, not merely in the region penetrated by the cold neutral particles. Here we consider
the diffusion coefficient required for this and the thickness of the region with high trans-
port coefficients provided that the density of the neutral particles is given at the outer
boundary of the region, where it is assumed that $x = 0$.

When the thickness of the radial-diffusion region is small, the plasma in it can be des-
cribed by

$$-D\frac{d^2 n}{dx^2} = A \exp\left(-\sigma \int_0^x n\, dx\right) n - \frac{n}{\tau},$$
(1)

where n is the plasma density; D, elevated diffusion coefficient, which is taken as constant;

τ, ion lifetime in the trap; $A \exp\left(-\sigma \int_0^x n\, dx\right) n$, rate of production of hot ions in the layer on

ionization of the injected beam of fast netural particles (the exponential factor incorporates the reduction in the beam density on passing through the layer); and $\sigma = K_0/v_0$ (K_0 is the overall ionization constant for the fast neutral particles caused by ions and electrons, while v_0 is the speed of the neutral particles in the beam). The layer is assumed to be optically thin for the fast neutral particles, and the parameters can be found by assuming that the

value of $\exp\left(-\sigma \int_0^x n\, dx\right)$ is one. The ion lifetime in the trap before entry to the loss cone is

determined by the collisional frequency and is inversely proportional to the plasma density: $\tau = n_c/An$ (n_c is the plasma density at which the rates of ion generation and loss at the end become equal). It is assumed that the ion temperature varies little in the layer.

The radial flow of plasma from the central regions is small because of the smallness of the diffusion coefficient; at the inner boundary of the layer at $x = x_c$, where the diffusion coefficient increases sharply, we can put

$$dn/dx \approx 0.$$
(2)

We consider the conditions at the outer boundary of a layer. We first note that the cold ions produced by ionization and charge transfer from the cold neutral particles are not retained in the trap, but are repelled by the ambipolar electric field and automatically enter the loss cone. They do not have time to interact with the hot ions and their concentration is small.

We assume that there is a sharp transition from the plasma to the neutral gas having the minimum possible thickness, which is approximately equal to the cyclotron radius ρ for the ions. This requires that the mutual penetration depth for the neutral particles (before ionization or charge transfer) and the ions due to displacement of the leading center (before charge transfer) is much less than ρ. The criteria for this are

$$l_n = \frac{v_r}{2n_0(k_i + k_c)} \ll \rho;$$
(3)

$$l_i = \sqrt{\frac{D}{n_x k_c}} \ll \rho,$$
(4)

where l_n and l_i are the characteristic dimensions for the changes in neutral and plasma densities; v_r, random velocity of the cold neutral particles; n_r, n_0, densities of the neutral particles at the outer side of the transition zone and of the plasma at the inner side; and k_i, k_c, ionization and charge-transfer constants.

Condition (4) means that we have to incorporate the finiteness of ρ in order to find the ion density distribution; the transition to this diffusion region occurs when

$$l_i = \frac{n}{dn/dx} = \rho.$$
(5)

We assume $x = 0$ at the point where this equation applies; in the transition zone $x < 0$, the ions may perform thousands of cyclotron rotations before charge transfer, and the width of the zone is approximately equal to ρ, and by virtue of (3) all charge-transfer and ionization processes for the neutral particles are completed in it. These processes are incoporated by means of the boundary condition for the diffusion region:

$$D\frac{dn}{dx} = \frac{n_x v_x}{4} \frac{k_c}{k_i + k_c} = \Gamma \quad \text{at} \quad x = 0.$$
(6)

This means that the boundary radial ion flux is equal to the number of charge transfers from plasma ions to cold neutral particles in unit time. Here we neglect the production of hot ions in the transition zone by ionization of fast neutral particles, which is unimportant be-

15

cause $A \langle n \rangle \rho$ is small ($\langle n \rangle$ is the mean plasma density in the transition zone). We therefore have a second-order equation in n with three boundary conditions, from which we can find x_c and n for a given D.

We integrate (1) once and substitute condition (2) at the inner boundary to get

$$\frac{D}{n_c^2}\left(\frac{dn}{dx}\right)^2 = A\left[\frac{n_i^2-n^2}{n_c^2} - \frac{2}{3}\left(\frac{n_i^3-n^3}{n_c^3}\right)\right], \tag{7}$$

where n_i is the plasma density at the inner boundary, $n_i \leqslant n_c$. We use (5) and (6) at the outer boundary in the form $dn/dx = \Gamma/D$, $n = n_0 = \rho\Gamma/D$ to relate n_i to D as

$$\frac{\Gamma^2}{n_c^2 D} = A\left[\frac{n_i^2}{n_c^2} - \left(\frac{\rho\Gamma}{n_c D}\right)^2 - \frac{2}{3}\frac{n_i^3}{n_c^3} + \frac{2}{3}\left(\frac{\rho\Gamma}{n_c D}\right)^3\right]. \tag{8}$$

The plasma density at the inner boundary is set at such a level that the difference between the rate of ion production in the layer and the rate of loss of them from the ends provides the given boundary flux Γ.

The layer thickness x_c can be found by solving (7):

$$x_c = \sqrt{\frac{D}{A}}\int_{n_0}^{n_i}\frac{dn}{\sqrt{n_i^2 - n^2 - \frac{2}{3n_c}(n_i^3-n^3)}}. \tag{9}$$

The inexplicit n(x) dependence is defined by the same formula with a variable upper limit of integration. Figure 1 shows the form of the $n(x/x_c)/n_c$ distribution.

To make estimates we used the parameters characteristic of the end traps in an ambipolar reactor [1]: magnetic field 12 T; plasma ion energy 700 keV; electron temperature T_e = 40 keV; $n_c = 2.5 \cdot 10^{14}$ cm^{-3}; $\tau(n_c) = A^{-1} = 1.3$ sec; $\sigma = 4 \cdot 10^{-17}$ cm^2; $\rho = 1.4$ cm; charge-transfer and ionization constants $4 \cdot 10^{-9}$ cm$^3 \cdot$sec^{-1} and $7.2 \cdot 10^{-8}$ cm$^3 \cdot$sec^{-1}, correspondingly; and $\Gamma = 2.5 \cdot 10^{14}$ cm$^{-2} \times$ sec^{-1} ($n_r = 10^{11}$ cm^{-3}, $v_r = 2 \cdot 10^5$ cm$\cdot$sec^{-1}).

Figure 2 shows how x_c, n_i, and $n_0 = \rho\Gamma/D$ are dependent on the given D. For $D \approx 4.9$ cm$^2 \cdot$sec^{-1}, $n_i/n_c = 1$, $x_c = \infty$, while for $D \leqslant 4.9$ cm$^2 \cdot$sec^{-1} there is no stationary solution and the plasma is eroded.

We consider the stability of a plasma layer adjoining a gas on the basis that the outer boundary of the layer initially at x = 0 can be displaced when the plasma density changes. The displacement speed V can be found by calculating the difference between the flux density for the hot ions at the boundary $-D(\partial n/\partial x)_{bo}$ and the rate of loss of these at the boundary due to charge transfer Γ. By virtue of the boundary condition $(\partial n/\partial x)_{bo} = n_{bo}/\rho$, we have

$$V = \frac{-D\left(\frac{\partial n}{\partial x}\right)_{bo} + \Gamma}{n_{bo}} = -\frac{D}{\rho} + \frac{\Gamma}{n_{bo}}. \tag{10}$$

Therefore, if n_{bo} at the boundary increases with time, the layer will expand. We introduce the new variables Y and T from $y = x + x'(t)/x_c + x'(t)$; and T = t (t is time) into the equation describing the plasma density change, so the outer boundary of the layer for any displacement $x' = -\int_0^t V\,dt$ will correspond to y = 0, while the inner boundary corresponds to y = 1. The equation for the plasma density in these variables is

$$\frac{\partial n}{\partial T} = \frac{y-1}{x_c+x'}\frac{\partial x'}{\partial T}\frac{\partial n}{\partial y} + \frac{D}{(x_c+x')^2}\frac{\partial^2 n}{\partial y^2} + An\left\{\exp\left[-\sigma(x_c+x')\int_0^y n\,dy\right] - \frac{n}{n_c}\right\}, \tag{11}$$

and the boundary conditions are

$$\frac{\partial n}{\partial y} = n\frac{x_c+x'}{\rho} \text{ at } y = 0; \quad \frac{\partial n}{\partial y} = 0 \text{ at } y = 1. \tag{12}$$

16
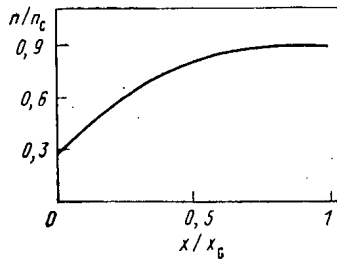
Fig. 1

Fig. 2

Fig. 1. Plasma density distribution in the layer for x_c = 7.6 cm and D = 5 cm$^2\cdot$sec^{-1}.
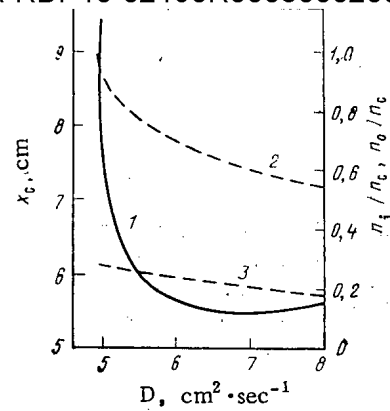
Fig. 2. Dependence of layer thickness (1) and plasma density at the inner boundary (2) and outer boundary (3) on the diffusion coefficient.

The attenuation of the fast neutral-particle beam in the plasma layer is important to the stability of the latter.

We represent n as the sum of a part n_1 independent of T and a small variable addition n'; $n_1(y)$ coincides with the above stationary solution $n(x/x_c)$. We substitute $n = n_1 + n'$ into (11) and into (12) and linearize these with respect to the small perturbations n' and x':

$$\frac{\partial n'}{\partial T} = \frac{y-1}{x_c}\frac{dx'}{dT}\frac{dn_1}{dy} + \frac{D}{x_c^2}\frac{d^2n'}{dy^2} - \frac{2Dx'}{x_c^3}\frac{d^2n_1}{dy^2} + An'\left(1-2\frac{n_1}{n_c}\right) - A\sigma n_1 x_c \left(\int_0^y n'\,dy + \frac{x'}{x_c}\int_0^y n_1\,dy + \frac{n'}{n_1}\int_0^y n_1\,dy\right). \quad (13)$$

The boundary conditions for n' are

$$\frac{\partial n'}{\partial y} = n_1(0)\frac{x'}{\rho} + \frac{x_c}{\rho}n' \quad \text{at} \quad y=0; \quad (14)$$

$$\frac{\partial n'}{\partial y} = 0 \quad \text{at} \quad y=1. \quad (15)$$

From (10) we have dx'/dT = $-V$ = (D/ρ) (n'(0)/n_1(0)); we represent n' as n' = exp(λT) k(y) and differentiate (14) with respect to T to get

$$k(0) = \frac{\lambda\rho^2}{D\left(1+\frac{\lambda\rho x_c}{D}\right)}\frac{dk}{dy}(0);$$

$$x' = \frac{\rho}{n_1(0)\left(1+\frac{\lambda\rho x_c}{D}\right)}\frac{dk}{dy}(0)\exp(\lambda T);$$

and substitute the expressions for n' and x' into (13) to get

$$\lambda k = \frac{\lambda\rho(y-1)}{x_c n_1(0)(1+\lambda\rho x_c/D)}\frac{dn_1}{dy}\frac{dk}{dy}(0) - \frac{2D\rho}{x_c^3 n_1(0)(1+\lambda\rho x_c/D)}\frac{d^2n_1}{dy^2}\frac{dk}{dy}(0) + \frac{D}{x_c^2}\frac{d^2k}{dy^2} \quad (16)$$

$$+ A\left(1-2\frac{n_1}{n_c}\right)k - A\sigma x_c\left(n_1\int_0^y k\,dy + \frac{\rho n_1}{x_c n_1(0)(1+\lambda\rho x_c/D)}\frac{dk}{dy}(0)\int_0^y n_1\,dy + k\int_0^y n_1\,dy\right).$$

It is difficult to solve this dispersion equation exactly and check whether there are no eigenvalues $\lambda > 0$; we use Galerkin's approximate method [3].

We choose the perturbation k in a form satisfying both boundary conditions:

$$k = C\left(\frac{\lambda\rho^2}{D(1+\lambda\rho x_c/D)} + y + Ry^2 - \frac{1+2R}{3}y^3\right), \quad (17)$$

17

where R and C are arbitrary constants.

The explicit $n_1(y)$ dependence is represented as an interpolation polynomial of fifth degree:

$$n_1(y) = \sum_{r=0}^{r=5} c_r y^r,$$

in which the coefficients c_r are chosen in such a way as to satisfy the exact values of $n_1(y)$ at six points. The expression for k is substituted into (16), which is multiplied by k and integrated from 0 to 1. We get a polynomial in powers of λ whose coefficients are dependent on R and R^2. The perturbation can only be a real function, so λ, R, and C must be real. We put $\lambda = 0$ to find the value of R such that the term independent of λ is

$$\int_0^1 \left[\frac{2\rho A n_1}{x_c n_1(0)} \left(1 - \frac{n_1}{n_c}\right) \frac{dk}{dy}(0) + A\left(1 - 2\frac{n_1}{n_c}\right)K + \frac{D}{x_c^2}\frac{d^2 k}{dy^2}\right] k\,dy - A\sigma x_c \int_0^1 \left[n_1 \int_0^y k\,dy + \right.$$

$$\left. + \frac{\rho n_1}{x_c n_1(0)}\frac{dk}{dy}(0)\int_0^y n_1\,dy + k\int_0^y n_1\,dy\right]k\,dy = 0. \tag{18}$$

The absence of real values of R that satisfy this condition means that the eigenvalue $\lambda = 0$ does not exist and that there is no transition from stability as R varies, i.e., the solution is stable. Calculations show that the plasma layer is stable for $D \lesssim 5$ cm$^2 \cdot$sec^{-1}, when $x_c \gtrsim 7.6$ cm.

This result, $D \approx 5$ cm$^2 \cdot$sec^{-1}, is about 40 times the classical value. The penetration depth l_i of the plasma into the gas and the same l_n for the neutral particles into the plasma are, respectively, 0.11 and 0.019 cm, and are much less than ρ, which confirms that the above boundary conditions are applicable. The value $\exp(-\sigma)\int_0^{x_c} n\,dx = 0.945$ can be replaced approximately by one in deriving the steady-state solution. According to (8) and (9), to retain n_i as Γ increases, the diffusion coefficient D should increase approximately as Γ^2, and x_c should increase as Γ.

There is additional energy dissipation in the surface layer by comparison with the central regions, because electron—ion pairs are produced by ionization of cold neutral particles and these are lost to the ends and take away energy $(eu + T_e)$, where u is the potential barrier to the electrons at the end. The following number of cold neutral particles is ionized per cm^2 of the side surface of the plasma:

$$\frac{n_r V_r}{4}\frac{k_i}{k_i + k_t} \approx \Gamma\frac{k_i}{k_t} \quad .$$

If we assume $eu = 8T_e$ for the purpose of estimation, then an additional power input of 260 W/cm^2 to the surface electrons is required to maintain the heat balance.

Therefore, by increasing the diffusion coefficient in a narrow peripheral region (e.g., by producing axial asymmetry or by disrupting the magnetic surfaces) and by supplying additional power to the electrons one can stabilize the side surface of the plasma in the end trap at a surrounding neutral-gas density of 10^{11} cm^{-3}. Such a vacuum is technically feasible.

LITERATURE CITED

1. N. Vasil'ev et al., "Tandem mirror hybrid reactor (TROL project)," Paper at the IAEA Working Conference on Particle and Energy Retention in Open Magnetic Traps, Novosibirsk (1981).
2. T. Fowler, Plasma Phys., 17, No. 7/8, 583 (1975).
3. L. V. Kantorovich and V. I. Krylov, Approximate Methods of Higher Analysis [in Russian], Fizmatgiz, Moscow (1962), p. 312.

18

EQUIPMENT COMPLEX FOR MONITORING THE NEUTRON FLUX OF THE CONTROL AND

SAFETY SYSTEM OF WATER–COOLED/WATER–MODERATED POWER REACTORS OF NUCLEAR

POWER STATIONS

G. F. Borovik, I. E. Burenko, A. M. Gusarov,   UDC 621.039.564
V. S. Zhernov, M. S. Kalenskii, I. S. Krasheninnikov,
V. A. Meshkov, Yu. B. Prokhorov, and A. G. Yakushev

Many years of experience in operating nuclear reactors have shown that the monitoring, protection, and control organization with respect to information about the thermal neutral flux density (neutron flux) differs in sufficient reliability, rapid response, and accuracy [1]. Soviet and international rules and recommendations have been developed for the construction of neutron–flux monitoring equipment, defining the requirements and conditions for ensuring the nuclear safety of nuclear power stations [2, 3]. Taking account of modern standards and recommendations at the start of the 1970s, the commercial issue of the third generation of neutron flux monitoring equipment (NFME) was developed and brought into use in the Soviet Union [4]. By means of this equipment, the safety and efficient operation of VVÉR–440 and VVÉR–1000 reactors are ensured in all their operating regimes, including fuel charging (recharging). The NFME complex (Fig. 1) shapes the signals which exceed the thresholds (settings) specified by the operator for the power and excursion period of the reactor, distributes signals to the control and safety system, and processes, records, and presents operative information at the control desk and panel of the nuclear power station and at the data computer.

Recently, a work cycle has been completed on the further improvement of the NFME for the purpose of increasing the reliability, lifetime, and economy, improvement of the operating characteristics, etc.

STRUCTURE AND OPERATING PRINCIPLES OF THE NFME

The NFME contains a number of subsystems which are functionally autonomous in operation [4]: fuel charging (recharging) monitoring (FCM), neutron flux monitoring for the reactor control and safety equipment, and neutron flux monitoring from the reserve control panel (RCP).

At the basis of construction of the complex is the so–called filar structure of the data measurement channels for shaping the scram system signals, the warning signaling, reactor control signals, etc.

The fuel recharging monitoring subsystem contains six detector units (DU), located for recharging in the reactor core shield. The detector unit signals are processed by two independent and identical subsystems, each of which contains three data measurement channels. The data are extracted at the unified control panel (UCP) in the central reactor hall and at the recharging machine control desk.

The detector units of the neutron flux monitoring subsystem for the reactor control and safety system are located in the ionization chamber channels (IC) of the biological shield of the reactor pit space. Two independent subsystems are provided, which process signals from the detector units located in pairs in adjacent ionization chamber channels. The assemblage of data takes place at three points of the reactor cross section, and ensures satisfactory representativeness of the data about the neutron flux for subsequent shaping of warning signals by "2 out of 3" logic [2]. The installed structural superfluity in the form of two subsystems, in case of necessity, allows the safety functions to be maintained and preventive operations to be carried out on the plant during the whole reactor operating period, and the installation of the main part of the equipment in different compartments makes it pos-
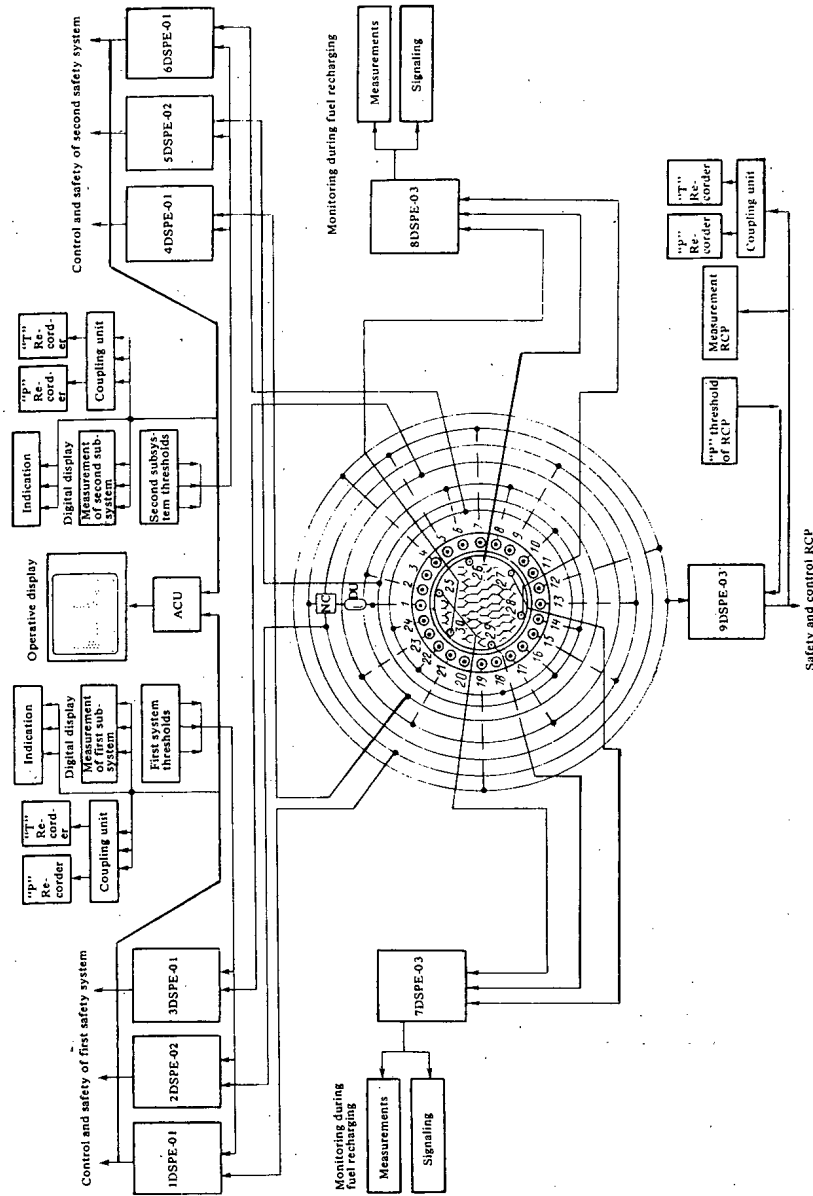
Fig. 1. Structure of the NFME complex.

DSPE = Data Storage and Processing Equipment;
NC = Normalizing Converters.

20

sible to ensure monitoring of the reactor in the case of an emergency situation (e.g., fire) in one of the compartments.

The range of measurements of the neutron flux density from the subcritical state of the reactor up to 120% reactor power amounts to 10-12 decimal orders of magnitude. For this the flux density in the IC for the VVER-440 varies within the limits 10^{-1} to $1.2 \cdot 10^{10}$ neutrons/ $(cm^2 \cdot sec)$, and for the VVER-1000 within the limits 10^{-1} to $6 \cdot 10^8$ neutrons/$(cm^2 \cdot sec)$. The whole range is divided arbitrarily into three subranges: source (SR), intermediate (IR), and power (PR). For reliability of carrying out the safety functions, overlapping measurement subranges are provided, from 1 to 1.5 decimal orders of magnitude.

A type KNK-15 fission chamber, operating in the pulsed regime, is used in the source range; a type KNK-4 helium ionization chamber is used in the intermediate range; and a type KNK-3 boron ionization chamber, operating in the current regime, is used in the power range. Each chamber operates in the current regime. The ionization is enclosed in the pressure vessel and is shielded with electromagnetic screens, insulated from the chamber and the outer vessel.

In order to increase the operating lifetime, provision is made for moving the IR and SR detector units by transfer mechanisms (TM IC) with automatic and manual control, and for a device for monitoring the position of the detector units (Fig. 2). The location of the detector units (DU) is shown on the unified control panel (UCP). The system of control with the transfer mechanisms automatically withdraws the detector units from the zone of substantial neutron fluxes during bringing of the reactor to power, and ensures their emergency insertion in the operating position in the case of transmission of a scram signal (SS) or a reduction of the reactor power. The manual control units provided for transfer of the detector units have priority over the automatic control. The power range detector units are not moved during reactor operation; their radiation stability is ensured by the corresponding parameters of the IC, and by the choice of structural materials and the communication line cable. In order to increase the noise-proofing of the data-measurement channels, the signals from the detector units are amplified and shaped in amplifier and conversion units (ACU), located near the outlet from the IC channels of the detector unit communication cable.

The signals, shaped according to duration and amplitude, are relayed along cables with a length of 150-200 m to the data storage and processing equipment (DSPE). Here the functional conversion of the data entering in pulsed form is effected in all the measurement subranges, and the discrete signals of the scram system (SS) and the warning signaling (WS), the discrete subrange switching signals, and also the analog signals for the reactor power controller and limiter (APC and RPL) are shaped, for recording on tape of the pen recorders for transfer to the computer and to the operator's console. Particular attention has been paid to total autonomy of the circuits for shaping the protection signals.

The setting of the level of protection with respect to power is formed by a preset unit from the operator's console. The settings are defined by a code switch. Provision is made for 10 settings in the source range and the intermediate range; in the power range the discreteness of the setting is equal to 1% of the nominal value of the reactor power. The settings with respect to period are defined autonomously in each channel within the DSPE. The settings of the scram system (SS) (10, 20, and 40 sec) automatically establish the settings of the warning signal (WS) (20, 40, and 80 sec, respectively).

In the case of faultiness or disconnection, for inspection or maintenance of any channel, a signal originates at its outlet, similar to the signal for exceeding the setting. The actuating units of the control and safety system function in the event of the appearance of signals for exceeding the setting in two channels operating in "triplet."

Data is presented to the operator on digital indicators (sampled over each channel), on the tape of a pen recorder (channelwise values or values averaged over three channels of the power or period), and on an operative display (CRT screen) in the form of histograms of the measurement data for all channels and a digital indication selectively for each of the channels. The centralized presentation of data about the power and period, with simultaneous display of the threshold settings on the display screen, helps the operator to understand the overall pattern for the whole complex and to determine nonfunctional channels, the margin prior to actuation of the setting for each channel, and the tendency to change of the operating cycle of the reactor. For the purpose of emergency, there are local devices for indicating the state of the measurement channels and of the essential measurement instruments in the DSPE.

21
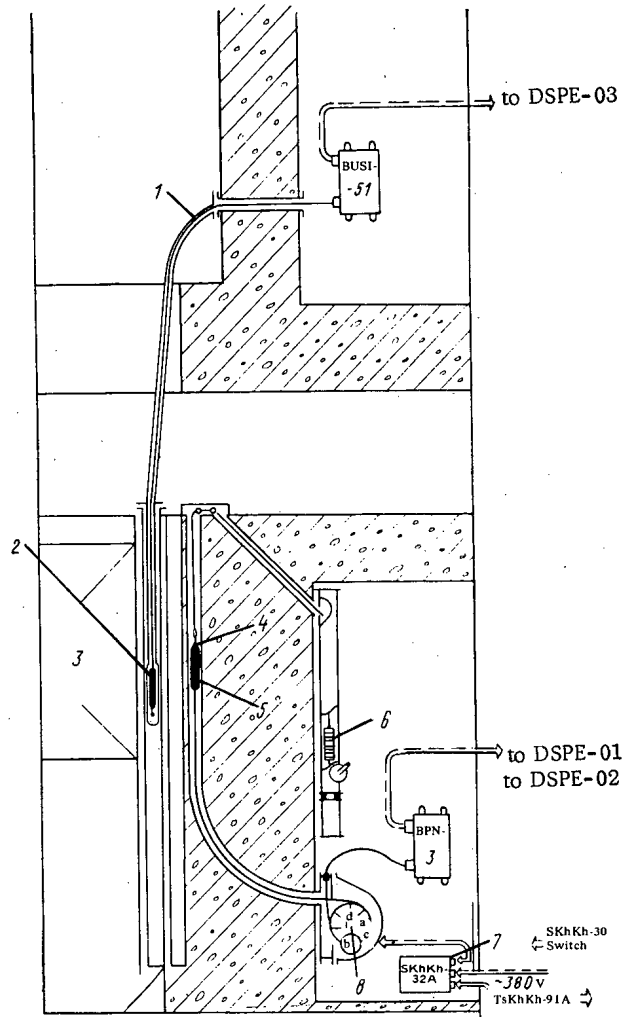
Fig. 2. Equipment for moving and monitoring the position of the
detector units: 1) mechanical part of the fuel charging monitor-
ing (FCM) (case, duct, etc.); 2) detector unit (BDPNZ-17A) for
monitoring the core during fuel recharging; 3) reactor core; 4)
clamp; 5) detector unit; 6) counterweight; 7) movement control; 8)
movement mechanism of detector unit (DU): SR and IR; a) reducer;
b) electric motor; c) selsyn detector; d) drum.

In order to ensure a high reliability of the complex, units are provided for monitoring
the serviceability of the data-measurement channels and the power supply equipment. These
functions in the structure of the NFME are effected by a number of automatic devices and in-
dividual units with manual control. The potentiality for calibrating the measurement circuits
with respect to both power and period, with verification of the principal parameters and the
transmission of scram signals, is set out in the monitoring units. Failure signals or devia-
tions from normal functioning are fed to the safety system and to the operator at the unified
control panel (UCP).

In the case of disruption of access to the compartment, neutron flux monitoring is ef-
fected with the equipment of the emergy control panel in the space, providing monitoring of
the shut-down reactor. The RCP measurement channels throughout the structure are unified with
the main subsystem for the control and safety of the reactor. There are three measurement
channels. The detector units are located in the IC channels of the reactor pit space.

When optimizing the design of the NFME complex, the following principles were fulfilled:

— output of warning signals in the case of any defects, right up to failure of the meas-
urement equipment;

— independence of warning signals on all other data and control signals;

— the assurance of priority of warning functions in relation to all others;

— the use of circuit and structural solutions, preventing the spread of damage to equipment;

— the use of the maximum possible measures for obtaining trustworthy data about the neutron flux of the reactor in the presence of noise (interference), radiation, temperature, and mechanical effects;

— the assurance of a high reliability index in the operating lifetime of the equipment;

— the presence of divided systems for monitoring the serviceability of the principal facilities of the complex, with automatic operating conditions and with separate units with manual control;

— convenience of operation and maintenance, with the capability of the rapid detection of faultiness and its elimination by replacement of the failed components and units.

PRINCIPAL CIRCUIT-TECHNICAL SOLUTIONS

When designing the input circuits of the data-measurements channels, particular attention was paid to noise screening and the achievement of a high sensitivity, and to the exclusion of the possible effect of a change of resistance of the communication cable insulation of the detector units from the amplification and conversion units, operating in complicated radiation and climatic conditions. In the SR and IR detector units, a special cable of the KAGÉ type is used, with three coaxial cores, enclosed in a common insulated screen of copper and steel. In the PR detector units a triaxial cable with magnesia insulation of the KNMS-2s type is used, which ensures prolonged operation in conditions of maximum neutron fluxes. The construction of the amplification and conversion units also has been calculated on the maximum noise attenuation and comprises electromagnetic screens connected with the screens of the cables without breaking the screening.

The pulsed signals from the SR chambers, with a repetition frequency of $0.05-10^5$ pulses/sec, are amplified, discriminated, and normalized in the preamplification units. The current from the IR and PR chambers is applied to the input of the current—frequency converter with a range of output signals within the limits of six decimal orders of magnitude. Thus, at the outputs of the amplification and conversion units, uniform signals are produced, which allows maximum unification of the circuit solutons of the functional processing equipment for all monitoring subranges.

In order to process the data with the measurement circuits of the functional processing units, analog circuit technique is used, which has a traditionally high reliability and requires minimum plant expenditure. The output analog signals with respect to power ($U_{out/max}$ = 5 V) in the range of six decimal orders of magnitude of the neutron flux variation in the SR and IR are represented in logarithmic scale. In the PR, variations of the output signal depend linearly on the neutron flux in the range 0.1–120% of the nominal value ($U_{out/max}$ = 6 V). The output signals with respect to the period are proportional to the quantity $1/T$, where T is the excursion period (10–200 sec), and $U_{out/max}$ = 5 V.

An additive pickup of medium frequency, with automatically varying integration time constant, has allowed the lower measurement limit of statistical signals in the SR to be extended to 0.02–0.05 pulses/sec, with an acceptable measurement delay; the stability of the circuit to the formation of warning signals with respect to period, with low values of the input frequency, is ensured by a device with a "memory," forecasting a change of power.

The data-measurement channels include threshold devices and they shape the command signals for the automatic range switching, with logic processing of the initial and final data over every range.

In the PR monitoring units, the output data are compared continuously by three measurement channels, with the formation of the alarm signal in the case of deviation of the readings of one of them from the average value of the upper permissible value.

The equipment of the complex is composed of unified standard designs (USD) [5], which allow the operating requirements on the technical means of ensuring the nuclear safety of the reactor to be satisfied, such as efficiency of servicing, convenience of operation, reliabil-

23

ity, and capacity for repair. The extensive unification of the basic components has helped to quite simply organize the series production of the equipment. The detector, amplification, and conversion units, designed for operation in specific conditions, are made in special hermetic designs.

ASSESSMENT OF EXPERIENCE

The first assembly of equipment for monitoring the neutron flux was installed in the "Lovisa-1" nuclear power station (Finland). It has operated since 1976 in normal conditions in the reactor control and safety system. At the power startup stage, an experimental calibration of the readings of the output systems of the NFME complex was carried out with respect to the value of the thermal power of the reactor. Further operating experience showed that the conformity established between the readings of the complex and the thermal power of the reactor are maintained over the range 30-100% of P_{nom}, with an error of not greater than ±2% of P_{nom} during the whole running period of the nuclear power station. The results obtained confirmed the feasibility of reading the thermal power of the reactor by the readings of the NFME complex. This allowed the efficiency of carrying out technological operations on controlling the reactor to be increased considerably.

The experience in operating the NFME in the "Lovisa-1" nuclear power station and, since 1980, in the "Lovisa-2" nuclear power station, has confirmed the high reliability of the equipment. On the average, during a single operating period no more than 1-2 faults occurred, which did not impair the functions of the system. This corresponds to a time of operation to failure of the equipment of ~4000-5000 h and confirms the calculated values.

The structure assumed for the NFME and the set of technical relationships have ensured flexibility of the system and have allowed it to be used in various nuclear power station projects and research reactors. The following modifications of the NFME were developed, differing in the constitution of the input systems, in order to satisfy specific requirements of one facility or another:

NFME-1 — a basic complex for VVER-440 reactors, operating in the "Lovisa" nuclear power stations in Finland;

NFME-2 — a complex with an equipment standby console, operating by means of the unified NFME technical systems NFME-1; the complexes are installed in the Rovensk, Köl'sk, Paksh (Hungary), and other nuclear power stations with VVER-440 reactors;

NFME-3 — a complex, differing in the arrangement of the power supplies; dual detector units are used in order to take account of xenon variations in the power generation range, and, correspondingly, additional processing units; it is being operated in the fifth unit of the Novovoronezh nuclear power station, and has been supplied to the southern Ukraine, Kalinin, and other nuclear power stations with VVER-1000 reactors;

NFME-5,6 — one subsystem of the equipment complex — the NFME-5 — is being used in the control and safety system of a research reactor, and the other — NFME-6 — is being used in the control and safety system of a critical assembly.

By the use of unified technical means in the NFME-5, the problem of intrareactor monitoring has been solved; additionally, a digital automatic regulator has been developed which provides automatic startup of the reactor with a period of 30 or 60 sec and automatic maintenance of a specified neutron flux in the range 1-100%. Data are superposed in the NFME-5 display about the running value of the neutron flux and about the position of the control rods. A digital linear—logarithmic gauge has been introduced into the NFME-6 for measuring the neutron flux over a range of six orders of magnitude, and for an automatic measurement of the scale of the pen-recording potentiometers.

The automatic change of the operating program of the complex, in order to ensure continuous measurements over all ranges of reactor operation, automation of the process for moving the detector units, the centralized extraction of data about all the measurement channels, and the presence of divided monitoring, have allowed the work of the operator with the equipment to be extremely simplified and the work of the maintenance personnel to be reduced.

ROUTES FOR IMPROVEMENT OF THE NFME

The experience of the manufacture and operation in nuclear power stations of third generation equipment for monitoring the neutron flux has shown the prospects for the accepted structure and the organization of the data-measurement channel links, as a result of which

24

the co_____ have been defined. The principal ones are:

— to increase the sensitivity and accuracy of the data-measurement channels;

— to increase the radiation stability and lifetime of the detector units;

— to reduce the number of ionization chambers in the biological shield of the reactor, and to eliminate the complex mechanisms for moving the detector units;

— to reduce labor consumption of manufacture and adjustment and to improve the metrologi- cal parameters of the equipment.

In order to improve the detector units, the following were taken into account: deficien- cies of the intermediate range helium ionization chambers, associated with an increase of the dark current during prolonged operation; limitation of the lifetime of the electronic compon- ents in the SR detector units; etc.

When improving the amplification and conversion units, particular attention was paid to increasing the sensitivity, accuracy, and linearity of conversion, and the stability of the parameters over a wide range of temperatures; obtaining reliable data in the presence of a high interference level; and significantly reducing the impedance of the cable insulation.

In the case of the data processing units, a search was conducted for solutions directed at increasing the measurement accuracy, reliability, and operating lifetime; reducing the power requirements; simplifying manufacture, adjustment, and operation; and ensuring stabil- ity in operation in the case of climatic and mechanical effects over wide limits.

In the data presentation facilities, solutions were derived for increasing the visual clarity and accuracy of presentation of the data, using video-monitoring equipment (VME) as- similated into industry.

In order to accelerate the first startup of the reactor, when the lowest value of the flux density amounts to 10^{-3} neutrons/(cm$^2 \cdot$sec) and the background γ emission and tempera- ture in the IC channels is insignificant, a slow neutron counter of the SNM-18 type was used as a detector.

Detector units can be installed in the standby IC channels of the reactor biological shield. In order to increase the sensitivity of this part of the equipment, a wide-range digital gauge was constructed, which allows the pulse repetition rate from the detector units to be monitored, starting from 0.01 Hz.

The first startup equipment (FSE) underwent testing during the physical startup of the fifth unit of the Novovoronezh nuclear power station and the first and second units of the Rovensk nuclear power station. The sensitivity of the FSE is approximately 300-500 times higher than the sensitivity of the SR channels of the standard NFME equipment.

The external functional processing unit with displaying digital indicators of the power and period is located at the UCP of the nuclear power station. The capability is provided for connecting the pen recorders and a sonic indicator. After the reactor reaches the minimum monitored power level, the detector units can be dismantled.

A further increase of the radiation resistance and lifetime, the reduction of the number of IC channels, and the elimination of the complicated mechanisms for moving the IC of the main NFME complex are determined mainly by the optimum choice of the IC and the cable links. When operating the NFME complex, an increase of the dark current of the KNK-4 (intermediate range) helium chamber with a large neutron fluence is observed, which requires additional measures for ensuring the necessary overlap of the subranges for measurements in the SR and IR.

The possibilities were investigated for reducing the ionization chambers (to two) with mon- itoring of the dynamic range of the neutron flux within the limits of $0.01-10^{11}$ neutrons/ (cm$^2 \cdot$sec) (Fig. 3). For the SI, by means of a standard fission chamber [6] in the pulsed switching range, the dynamic operating range is extended up to 10^6 neutrons/(cm$^2 \cdot$sec). The principal parameters of the fission chamber are: sensitivity in the pulsed regime $S_n = 0.1-$ 0.5 pulse/neutron$\cdot$cm^{-2}; sensitivity in the current regime $\delta_n = (1.8 \pm 0.4) \cdot 10^{-13}$ A/(neutron$\cdot$ cm$^{-2} \cdot$sec^{-1}); sensitivity to γ background $\delta\gamma = 1 \cdot 10^{-11}$ A/(R$\cdot$h^{-1});* initial dark current $1 \cdot 10^{-8}$ A^{-1}; and electrical capacity 340-360 pF.

_____
*1 R = $2.58 \cdot 10^{-4}$ C/kg.
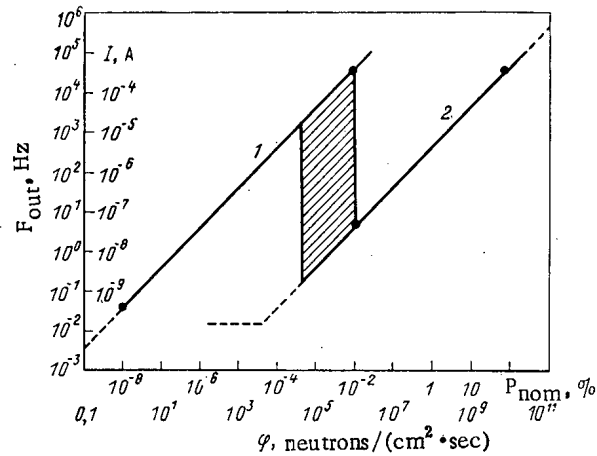
Fig. 3. Monitoring range: 1) startup range, KNK-15 chamber (S_n = 0.05-0.1 pulse/neutron/(cm^2·sec)); 2) working range, KNK-17 chamber (δ_n = 5 ·10^{-14} A/neutrons/(cm^2·sec), δ_γ = (0.5-1)· 10^{-13} A/R·h); conversion coefficient K_{con} = (1-2)·10^8 Hz/A.

A reduction of the cable-link leakage and background currents, and an increase of linearity, sensitivity, and stability of the converter in the normalizing conversion units, allowed a stable recording of the neutron flux to be obtained from 10^4 to 10^{11} neutrons/(cm^2·sec) for the IR and PR by means of a single compensated boron chamber in the current regime. The principal parameters of the boron chamber are: sensitivity to thermal neutrons 5·10^{-14} A·cm^2/neutron; sensitivity to γ background 1.6·10^{-13} A/(R·h^{-1}); dark current 5·10^{-12} A; and maximum current 4 mA. The starting point of the monitoring range of the boron chamber is determined with consideration of the inherent dark current and the current compensated by an order of magnitude from the background of the shut-down reactor (P_γ = 10^4 R/h):

$$I_b = I_d + 0.1 I_\gamma (10^4) = 1.6 \cdot 10^{-10} A.$$

If the condition is specified for an excess of the useful signal above background by one decimal order of magnitude, the minimum neturon flux to be monitored amounts to

$$\varphi_{min} = 10 I_b / S_n = 3 \cdot 10^4 \text{ neutrons}/(\text{cm}^2 \cdot \text{sec}).$$

In this case, an overlap with the SR is ensured, equal approximately to two decimal orders of magnitude.

The important advantage of the boron chamber is the considerable length of its sensitive part, which allows the best averaging of the measurement channel readings of the neutron flux over the height of the reactor core.

The lifetime of the SR and IR detector units in the NFME complex is determined also by the radiation resistance of the KAGÉ type communication cable. An increase of the lifetime up to the required values in the existing NFME is achieved by withdrawing these units, by means of the movement mechanisms, from the zone of high fluxes. The manufacture of these mechanisms is complicated and expensive. It is possible to exclude the necessity for the complex movement mechanisms and to significantly increase the lifetime by using a cable of the KNMS-2s type with inorganic insulation in the communication line for the translation of current and pulse signals from the ionization chambers. It should be taken into account for this that if the cable possesses the required parameters for the transmission of current signals, then for the transmission of pulsed signals its electrical properties are far from optimum. Therefore, when designing the pulse amplifiers it is necessary to solve a number of difficult and occasionally contradictory problems. The principal ones of these are to ensure the optimum input impedance and frequency characteristics, the best signal-to-noise ratio, and the stability and linearity of the parameters over a wide frequency range. Only special circuit-technical solutions will allow reliable data to be obtained in the presence of external electromagnetic and network interference. The problems of finishing structures, screening, and earthing, joining of input cables, and levels of circulating signals have required special attention.

A pulsed amplifier with a low-noise input cascade to a field transistor, acting through a charge-sensitive circuit (Fig. 4a), is recognized as the optimum. The following principal

26
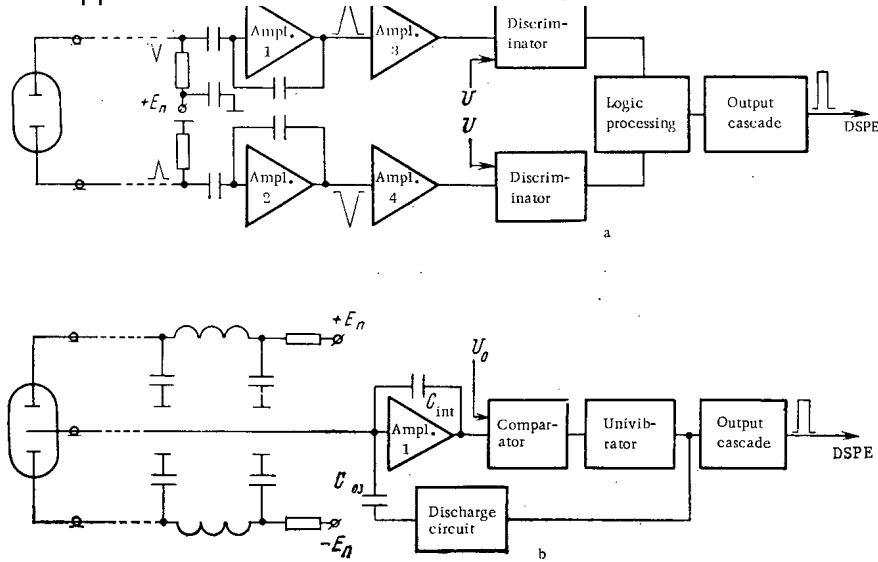
Fig. 4. Structural diagram of the startup range and working range normalizing converters: a, b) amplifier (KNK-15 chamber) and conversion (KNK-17) units, respectively.

parameters of the amplifier were obtained: cutoff amplification frequency ~$5 \cdot 10^6$ Hz signal to noise ratio not less than 20; amplification factor 10^7 V/A, and input duration 0.5-0.7 μsec.

In order to improve the noise screening, heteropolar pulses taken from the collecting and plus electrodes of the chamber were compared, with subsequent duration selection. The additional noise suppression amounted to 40 dB, with slight reduction of the recording efficiency (by approximately a factor of two).

For the intermediate and power monitoring ranges, the principle of measuring the chamber current by means of current-to-frequency conversion was preserved (Fig. 4b). It is possible to increase the conversion accuracy, linearity, and stability by separating the dosing and integration functions, using the method of periodic integration of the input current.

Great attention was paid to the effect that reduction of the insulation resistance of the communication cable link between the ionization chamber and the conversion unit has on the conversion error. The circuit ensures conservation of the parameters within 5% limits, with a reduction of the cable insulation resistance to 10^5 Ω.

The conversion factors, depending on the range of the measured current, may amount to $10^8 - 10^{10}$ Hz/A. The conversion error (linearity) is ±1%; the additional error with change of temperature of the surrounding medium amounts to not less than 0.5% per 10°C (for I_{in} = 10^{-8} A).

The functional processing units (FPU) of the data-measurement channels, because of the use of digital data processing methods in all ranges of variation of the reactor and period, have increased sensitivity, accuracy, stability, and lifetime parameters. The design of the functional units, using KMOP micropower series of microcircuits of medium and high integration with increased interference stability, allows the thermal regime of the equipment to be significantly eased and to be managed completely without additional adjustments during tuning and operation, and allows the maintenance suitability and interchangeability of individual components and units to be increased considerably.

The separation of the shaping circuits for the warning signals with respect to power and period in the structure of the functional processing units (Fig. 5) provides a significant increase of reliability of the channels. The calculated value of the time of operation to breakdown for the data-measurement channel amounted to 20,000 h.

A variation of the FPU design, with program-controllable units based on microprocessors (Fig. 6), was considered. In this case, several routes defined by the elementary base (series of BIS microprocessors), with assumed algorithm and architectural structure, are possible. Each of the routes has its advantages, which may prevail in specific production conditions.

27
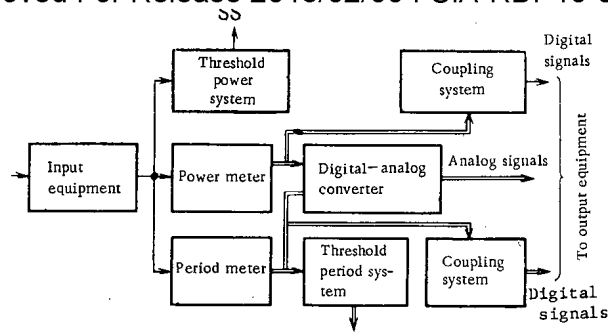
Fig. 5. Structural diagram of the digital
functional processing unit (FPU).
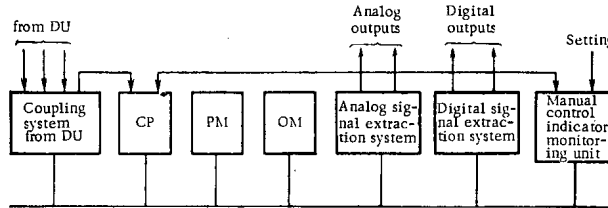
Fig. 6. Structural diagram of the FPU based
on microprocessors.

The unit provides simultaneous data processing in all ranges. Because of the different re-
quirements on accuracy and fast response in the startup and power ranges, and also because
in the power generation range uniformly distributed pulses arrive at the FPU input, and in the
startup ranges a statistically distributed stream of pulses arrive, in these ranges it is ad-
vantageous to use different methods of measuring the power and period.

The FPU consists of a coupling system with the detector units (DU), a central processor
(CP), a permanent memory (PM), an operative memory (OM), a system for the extraction of an-
alog and digital signals, a monitoring unit, indicators, and manual control. A busbar ar-
rangement for interchange with these is used in the FPU; all systems are linked with a single
trunk line.

The coupling system ensures electrical coupling of the FPU with the detector units, and
also contains the pulse counters and timer devices, essential for the input of data from the
DU and for time tracking. The central processor (CP) processes the data, and controls the
operation of individual systems of the unit and the interchange of data; the PM, with a cap-
acity of ~2 kbytes, serves for the storage of the FPU operating programs; and the OM, with a
capacity of ~256 eight-discharging layers, serves for the storage of the intermediate results
of processing. The analog signal extraction equipment converts codes into voltage and feeds
the signals to the pen recorder, RPL, APC, and computer. The digital signal extraction equip-
ment provides the delivery of data in digital form to the presentation system, and also issues
signals which exceed the threshold settings. The monitoring, indicator, and manual control
unit effects the control by automatic monitoring of the soundness of the FPU, indication of
the quantities being measured, the admission and transmission to the central processor of the
values of the settings from the control desk, and also the manual control of the different
operating regimes of the FPU, necessary for carrying out startup adjustment, preventive, and
maintenance operations. Regimes for the automatic monitoring of serviceability, such as mon-
itoring the serviceability of the detector units by the presence in the FPU of an input fre-
quency, and for continuous and test monitoring, are also provided for in the FPU.

The constitution of the complex was refined by taking account of the long-term structure
of the control and safety system, which provides for the presence of three safety systems (Fig.
7).

The NFME complex contains three subassemblies: The first and second main subassemblies
comprise three neutron flux measurement channels over the whole range of variation, including

28
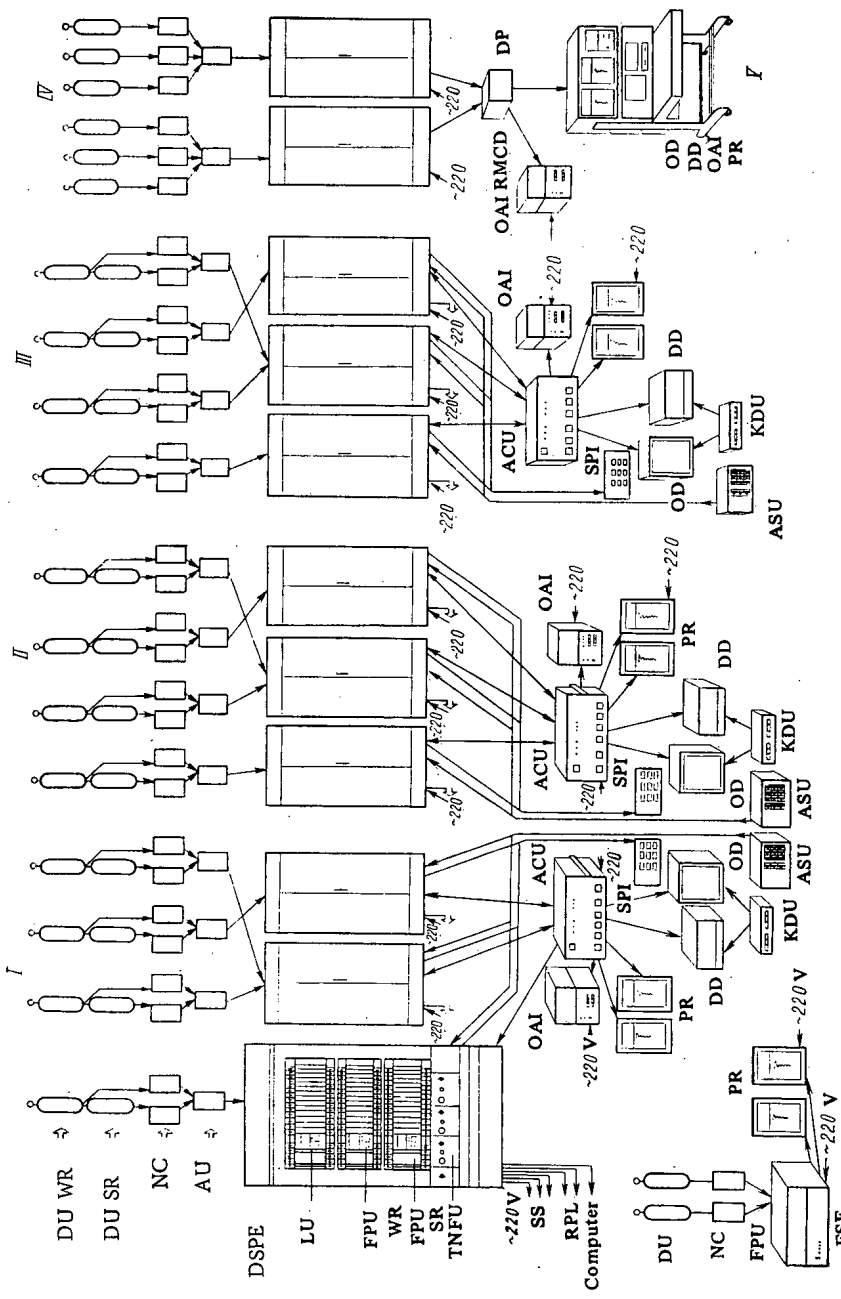
Fig. 7. Neutron flux monitoring equipment — NFME: I-III) subassemblies; IV) recharging monitoring system; V) duty physicist's moveable station; DU WR) working range detector units; DU SR) startup range detector units; NV) normalizing converters; AU) auxiliary units; DSPE) data storage and processing equipment; LU) logic unit; FPU WR) working range functional processing unit; FPU SR) startup range functional processing unit; TNFU) transformer and network filter unit; OAI) optoacoustic indicator; DD) digital display; PR) pen recorder; KDU) keyboard display unit; SPI) signal panel indicator; OD) operative display; ASU) assignment setting unit; OAI RMCD) optoacoustic indicator of the recharging machine control desk; DP) distribution panel; OD) operative display.

the first startup equipment (FSE) and the measurement channels of the fuel recharging monitoring system (FRMS); the FSE and FRMS channels are not involved in the third subassembly — monitoring of the reactor in the source range (SR), intermediate range (IR) and power range (PR) is effected by means of this subassembly. The measurement channel of each subassembly contains: a tandem wide-range detector unit, installed in one ionization chamber channel without transfer during operation, and an amplifier conversion unit (ACU) (one to each ionization chamber); a DSPE rack, including functional processing units and a logic unit; and an analog and digital data presentation equipment, and an assignment setting unit (ASU) with respect to power.

From the first and second subassemblies of the NFME issue three discrete scram signals (SS) according to "2 out of 3" logic, three discrete threshold safety signals (TS) to the control and safety panel room, and analog signals for the control and dumping of the reactor power (by the RPL and APC).

The power and period measurement channel data arrive at the digital indicators and pen-recorder potentiometers selectively through any measurement channel. The data presentation units from the three subassemblies are duplicated at both the UCP and at the RCP.

Centralized data extraction on a CRT screen is provided for in analog (histogram) and digital form from the first and second subassemblies.

The threshold settings with respect to the period are assigned in channel (within the DSPE), and the settings with respect to power in the startup range (SR and IR) are centralized from the assignment setting units in each "triplet"; in the PR the power settings are assigned individually.

The design of the measurement channels, by varying the composition of the basic equipment, allows conversion to shaping the warning signals by "2 out of 4" logic. Conversion to "2 out of 4" logic can be effected easily after introducing variations in the structure of the nuclear power station safety system, associated with the provision of a power supply system with cable cuttings and runs, and with the acceptance of the NFME signals by other systems.

CONCLUSIONS

Experience in the operation and commercial manufacture of third-generation NFME confirms the long-term prospects of the accepted constitution of the structure and the competence of the functions performed, in order to ensure the safety of nuclear power station reactors. The flexible and all-purpose structure of the data-measurement channels, by a simple means, allows the significant difference in the neutron flux monitoring ranges and operating conditions of the VVER-440 and VVER-1000 to be taken into account, and also allows the neutron flux in research reactors and critical assemblies to be monitored.

The high parameters concerning the reliability and metrological qualities have been confirmed, ensuring monitoring and control of the reactor power by the NFME signals during the running time, with sporadic calibration by the value of the thermal power.

Subsequent improvement of the structure and elevation of the technical parameters of the measurement channels are based on the extension of the range of application of the standard IC, the cables, and the use of digital processing methods. The achievement of new technical solutions will ensure elevated parameters of accuracy, stability, reliability, and noise suppression, and will reduce the power requirements of the equipment.

The combination of new technical solutions will make it possible to considerably simplify the layout of the reactor, and to increase the efficiency, reliability, and safety of nuclear power stations, taking into consideration possible extreme situations.

30

1. V. A. Sidorenko, Problems of the Operating Safety of VVÉR Reactors [in Russian], Atomiz-dat, Moscow (1977).
2. Regulations for the Safety of Nuclear Power Stations IBYa-04-74 [in Russian], Atomizdat, Moscow (1976).
3. Recommendations of the International Electrotechnical Commission. General Principles Relating to Equipment for Nuclear Reacotrs [in Russian], Publications 231, 232, and 323, Geneva (1967).
4. I. E. Burenko et al., in: Proceedings of a Symposium of Specialists of CMEA Member-Countries on "Strucutre of Systems of Equipment of Nuclear Instrument Manufacture" [in Russian], Moscow (1976), p. 13.
5. System of Unified Standard Designs of Aggregation Complexes for Hydroelectric Power Stations. Types and Basic Dimensions [in Russian], GOST 20504-81.
6. A. B. Dmitriev and E. K. Malyshev, Neutron Ionization Chambers for Reactor Technology [in Russian], Atomizdat, Moscow (1975).

INDUCED ACTIVITY OF CERTAIN CONCRETES IRRADIATED AT A 680-MeV PROTON ACCELERATOR

V. F. Kas'yanov, A. N. Kargin,
M. M. Komochkov, B. V. Man'ko,
and B. S. Sychev

UDC 539.16.04:621.039-78

One method of decreasing the induced activity at present-day accelerators is to use building and structural materials which are not highly activated in particular concrete. Nachtigall and Charalambus [1] investigated, in detail, the laws of formation of ^{24}Na in the concrete at the CERN accelerator. Estimates of the activation of the concrete shield of a proton accelerator reported in [2] showed that ^{24}Na made the largest contribution to the total dose rate from the induced activity. Experimental studies of the activation of concrete at the Berkeley betatron [3] led to the same conclusion.

Study of the induced activity of building and structural materials, including ordinary concrete with a density of 2300 kg/m³ [4, 5], showed that the principal radionuclides are ^{24}Na, ^{22}Na, ^{56}Mn, ^{54}Mn, and ^{7}Be, and that of these ^{24}Na and ^{22}Na present the greatest radiation hazard. It was shown in [6] that the induced activity of lime concrete was 3–10 times lower than that of granite concrete.

We present calculated and experimental values of the induced activity of concretes of various chemical compositions when irradiated in a field of scattered neutrons in the 680 MeV proton accelerator room. The flux of scattered neutrons at the places where the samples were irradiated at the JINR synchrocyclorton was measured with activation detectors [4]. The values of the neutron flux in various energy groups were used in the activation calculations.

The technological and chemical compositions of the concretes chosen for the study are listed in Table 1. Ordinary concrete with a density of 2300 kg/m³, the most commonly used shielding and structural material at accelerators, is taken for comparison. The chemical composition of Portland cement, the principal binder in concretes, is listed below by wt. % [7]:

Na	. . . 0,1	Al	. . . 3,05
K	. . . 1,1	Fe	. . . 2,37
Si	. . . 11,45	O	. . . 36,39
Ca	. . . 39,2	Other	. . . 0,68
Mg	. . . 3,01		
S	. . . 1,33	Loss in calcination. . 1,32	

31

TABLE 1. Technological and Chemical Compositions of Concretes Studied

Concrete	Input of material, kg/m³						Density, kg/m³	Content of elements, %														
	binder	fine aggregate	coarse aggregate	solvent (sealer)	admixture	plasticizer		Na	K	Si	Ca	Mg	S	Al	Fe	O	C	H	Ti	Mn	P	N
Original granite concrete	425 (portland cement)	480 (quartz sand)	1220 (crushed granite)	175 (water)	—	—	2300	1,17	2,63	28,56	9,06	0,80	0,29	3,9	1,62	50,26	0,54	0,82	0,22	0,09	0,04	—
Polymer granite concrete	184 (ÉD-5 epoxide resin)	598 (quartz sand)	1150 (crushed granite)	23 (toluene)	184 (silica flour) 37 (polyethylene-polyamine)	124 (coal tar)	2300	1,01	2,11	32,85	1,71	0,35	0,03	1,68	1,26	48,10	7,83	1,06	1,46	—	—	0,
Ordinary lime concrete	430 (portland cement)	398 (limestone sand)	1228 (crushed limestone)	244 (water)	—	—	2300	0,12	0,26	2,73	34,23	0,84	0,33	0,39	0,77	50,47	8,19	1,20	0,34	0,09	0,04	—
Polymer lime concrete	168 (ÉD-5 epoxide resin)	672 (limestone sand)	1000 (crushed limestone)	20 (toluene)	40 (polyethylene-polyamine)	100 (coal tar)	2000	0,12	0,07	0,72	32,8	0,34	0,10	0,12	0,39	46,42	17,18	1,09	0,10	—	—	0,

32

Fig. 1. Decay of induced activity of concretes after irradiation:
———) calculated, $\bigcirc$, $\bullet$, $\triangle$, $\square$) experiment; $\bullet$, $\triangle$) ordinary concrete
with granite and limestone aggregates; $\bigcirc$, $\square$) polymer concrete with
granite and limestone aggregates, respectively; Φ_T = 2.8•10^5 neu-
trons/cm^2•sec; Φ_P = 0.62•10^5; $\Phi_{E=2-20}$ MeV = 3.0•10^5; $\Phi_{E>20}$ MeV =
1.7•10^5.

In polymer concretes, Portland cement is replaced by an epoxide resin. Crushed lime-
stone is used because its chemical composition approximates that of marble ($CaCO_3$), which is
not highly activated [5, 8].

The specific induced activity Q of the concretes (mg-eq Ra/g) was calculated from the
expression

$$Q\,(t,\,\tau,\,n,\,k) = \frac{1}{8.4}\,\frac{1}{3.7\cdot10^7}\,\frac{0.602}{10^3}\,\sum_{(j)}\sum_{(m)}\sum_{i}F_{mk}\sigma_{ij}^{(m)}\eta_{jn}k_j^{(i)}\,\frac{1}{A_j}\,e^{-\lambda_i\tau}\,(1-e^{-\lambda_i t}),$$

where t and τ are, respectively, the irradiation and cooling times, sec; F_{mk}, neutron flux in
the m-th energy group in the k-th neutron distribution, neutrons/cm^2•sec; σ_{ij}^m, cross section
in mb (1 b = 10^{-28} m^2) for the formation of the i-th radionuclide from the j-th stable element
of atomic number A_j when bombarded with neutrons of the m-th energy group (these cross sec-
tions were taken mainly from [9, 10]; η_{jn}, weight content of the j-th element in the material
of the n-th composition, %; λ_i, decay constant of the i-th radionuclide; k_j^i, gamma constant
of the i-th radionuclide, (R/h)/(mCi/cm^2) (1 R = 2.58•10^{-4} C/kg; 1 Ci = 3.700•10^{10} Bq). The
calculated values of the specific activity Q (t, τ, n, k) are shown in Fig. 1.

Concrete samples cast in the form of cubes 40 mm on an edge were irradiated for 180
days in the field of scattered neutrons in the synchrocyclotron room. The induced activity
was measured with a spectrometer with a 36 cm^3 Ge(Li) detector and an AI-8000 pulse-height an-
alyzer. The spectrograms were processed on a Minsk-2 computer. Radionuclides were identified
by comparing the measured γ energies with tabulated values [10, 11]. The absolute values of
the induced activity of the concretes were found from a calibration: silver nitrate ($AgNO_3$)
of known specific activity was dissolved in a cube with an unsolidified mass of concrete hav-
ing a density close to that of the concretes under study. The efficiency of recording γ rays
was determined by measuring this sample on the spectrometer.

The measured and calculated values of the specific activity of the concretes studied are
compared in Fig. 1. The calculations took account of the contributions of the following radi-
onuclides identified in the irradiated samples: ^{24}Na, ^{22}Na, ^{56}Mn, ^{54}Mn, ^{52}Mn, ^{7}Be, ^{42}K, and
^{43}K. The total error in the measurements of the activity does not exceed 30%, taking account
of the error of the volume calibration.

The calculated and experimental results are in satisfactory agreement. The average var-
iance of these data is 1.5. The computational errors are a result of using inaccurate values
of the neutron flux, the reaction cross sections, and the chemical composition of the con-
cretes.

33

In summary, it was established that the principal radionuclides determining the induced activity of the concretes tested are the following: in the first 5 h after irradiation, ^{24}Na and ^{56}Mn; for τ = 5 h to 4 days, ^{24}Na; for τ > 4 days, ^{22}Na, ^{54}Mn, and ^{7}Be. The main contribution to the induced activity of the concrete comes from Na, Mn, Fe, Al, and Si, listed in order of decreasing contribution to the total specific activity.

The concretes studied are less highly activated than ordinary concrete. By replacing Portland cement by epoxide resin, and using the same aggregates, the induced activity was decreased by a factor of 1.5-2 for $\tau \leqslant 30$ days. By replacing the coarse and fine aggregates (crushed granite and quartz sand) by crushed limestone and sand, and retaining Portland cement as the binder, the activity of the concrete was decreased by a factor of 3-8 for the same values of τ. Finally, by replacing the Portland cement binder by epoxide resin, and the crushed granite and quartz sand aggregates by crushed limestone and sand, the induced activity of the concrete was 8-14 times smaller than that of ordinary concrete.

In conclusion, the authors thank V. M. Tsubko-Sitnikova, M. I. Fominykh, and E. T. Kondrata for making available the measuring complex and the Minsk-2 computer.

LITERATURE CITED

1. D. Nachtigall and S. Charalambus, CERN, 66-28, Geneva (1966).
2. T. Armstrong and J. Barish, Nucl. Sci. Eng., 38, 265 (1969), ORNL-TM-2630 (1969).
3. K. Goebel et al., CERN, 71-21, Geneva (1971).
4. V. F. Kas'yanov et al., JINR R16-8899, Dubna (1976).
5. V. F. Kas'yanov et al., JINR 16-12/375, Dubna (1979).
6. V. F. Kas'yanov and P. A. Lavdanskii, At. Energ., 45, 123 (1978).
7. D. L. Broder et al., Concrete in Nuclear Reactor Shields [in Russian], Atomizdat, Moscow (1966).
8. M. Barbier, Induced Radioactivity, North-Holland, Amsterdam—London (1969).
9. L. R. Kimel' and V. P. Mashkovich, Shielding Against Ionizing Radiations (Handbook) [in Russian], Atomizdat, Moscow (1972).
10. V. S. Barashenkov and V. D. Toneev, The Interaction of High-Energy Particles and Atomic Nuclei with Nuclei [in Russian], Atomizdat, Moscow (1972).
11. G. Erdmann and W. Soyka, Gamma Lines of Radionuclides, KFA (1974).

34

RADIATION CONDITIONS IN A 16-MeV ELECTRON MICROTRON ACCELERATOR

A. G. Belov, G. A. Komendantova,
Yu. G. Teterev, and A. P. Cherevatenko

Microtons [1] recently have been increasingly employed in science and technology. The 16-MeV microtron of the Joint Institute of Nuclear Research is used as the basic unit of neutron activation and γ activation analysis of geological samples [2] and has the following basic parameters:

Energy E_0 of the accelerated electrons	16 MeV
Average current of the accelerated electrons	up to 30 μA
Repetition frequency of the radiation pulses	50–800 Hz
Duration of Radiation Pulses	2.5 μsec
Efficiency of outputting the electron beam	⊳90%
Slowing-down target	2 mm tantalum
Beam power on the target	up to 0.48 kW
Neutron converter	Uranium + beryllium
Integral neutron yield	$3 \cdot 10^{11}$ neutrons/sec
Neutron moderator — graphite assembly with dimensions	$1 \times 1 \times 1$ m
Volume of the installation site	140 m³
Ventilation rate	1400 m³/h
Flow rate of the water cooling the microtron	2 m³/h

The electron beam, accelerated to 16 MeV, is extracted with the aid of a magnetic channel from the accelerator and directed with a rotating magnet either towards the center of a graphite cube (where the tantalum bremsstrahlung target and, transverse to it, the natural uranium neutron converter surrounded by beryllium are located) or to a channel at the end of which there is only the bremsstrahlung target (Fig. 1). Samples to be studied with neutron activation are placed into the graphite cube used for thermalization of photoneutrons. The microtron is mounted in a room on the second floor level of the Laboratory Building. Both the ceiling and the floor have a thickness of 1.6 m and are made of conventional concrete.

During the operation of the equipment, the microtron components at which electron losses occur during the electron acceleration and the outputting from the microtron and the bremsstrahlung target proper are sources of γ bremsstrahlung. Neutron sources are provided by the neutron converter and by the components of both the microtron and the equipment which are subjected to irradiation by γ quanta of an energy exceeding the threshold of photonuclear reactions ($E_{thr} = 10.8$ MeV in the case of copper). After switching off the accelerator, residual radioactivity persists in the components and in parts of the microtron, the bremsstrahlung target, and the converter. During the first few minutes after switching off the microtron, the uranium converter emits delayed fission neutrons.

The bremsstrahlung from the heavy target has a sharply pronounced angular distribution in a solid angle of about 15° in the direction of electron motion (at $E_0 = 16$ MeV) [3]. The angular distribution of the photoneutrons from the uranium converter can be considered isotropic [4], whereas the energy distribution resembles the fission spectrum with an average energy of ~1.2 MeV [5].

The goal of the present work was to obtain empirical information on the factors contributing to the radiation hazard and on the sources in the unit during its operation, and to clarify the possible use of the information in industrial equipment for the purpose of regular monitoring.

35

The high pulse duty factor (1000–8000) and the rather high limit energy of the γ quantum spectrum before and behind the shield result in conditions of measurement for which most of the standard instruments of radiation monitoring are not designed Therefore, it was investigated whether the readings of the dosimetry instruments are adequate under the conditions of microtron radiation, and the operational limits of the instruments were determined.

LiF TLD-700 thermoluminescence detectors of the Harshaw company were used as the basic dosimeter of the γ radiation [6, 7]. The TLD readings are not affected by the fact that the radiation is pulsed, and their dependence upon the radiation hardness does not exceed 20% in the case of bremsstrahlung with an effective energy of up to 10 MeV [8]. It is assumed that behind the shield and beyond the limits of the direct bremsstrahlung beam, equilibrium exists between the charged and the neutral components. Figure 2 shows the results of a comparison of TLD-700 readings with the readings of other γ radiation dosimeters: dosimeters making use of the RUP-1 gas discharge counter [9] or the DRG3-01, DRG3-03, and DRG3-04 scintillation detectors [10]. The scintillation dosimeters measure the bremsstrahlung dose rate adequately in the range $P_\gamma \leqslant 500$ μR$\cdot$sec^{-1} (1 R $= 2.58\cdot10^{-4}$ C/kg). It was a surprising finding that even the RUP-1 instrument with a γ detector having a dead time which is comparable to the pulse length of the microtron radiation renders correct readings at $P_\gamma \leqslant 40$ μR$\cdot$sec^{-1}. This fact seems to be associated with the low efficiency of γ quanta recording (at $P_\gamma \geqslant 40$ μR$\cdot$sec^{-1}, the RUP-1 substantially reduces the dose rate which can be measured).

A noticeable sensitivity to γ bresmsstrahlung of the microtron at $P_\gamma \geqslant 0.5$ μR$\cdot$sec^{-1} of the industrial DNA-1 neutron dosimeter [10] and the RUP-1 radiometer with neutron detector was established. In measurements behind the neutron shield, where, according to the results of measurements with nuclear emulsions [11] and of REM-2 recombination dosimeter measurements [12], there should be practically no neutrons (the measured coefficient of the radiation quality rendered the value KK ≈ 1), the RUP-1 instrument with neutron detectors recorded about 40,000 neutrons/(cm$^2\cdot$sec), whereas the DNA-1 instrument rendered a value of about 200 mbohr$\cdot$ h^{-1} regardless of which point was used in the measurements (1 bohr = 1 cSw). This result, obtained with the neutron instrument equipped with scintillation counters, can evidently explain the fact that the signals produced by powerful high-energy γ quantum radiation pulses exceed the discrimination threshold of the electronic circuits of those instruments.

The SNM-14 corona counters of slow neutrons are insensitive to nonpulsed γ radiation fields at $P_\gamma < 1500$ R$\cdot$h^{-1} [13]. The effect of pulsed bremsstrahlung of the microtron upon the operation of the counter placed at the center of a paraffin cylinder with a wall thickness of 120 mm was investigated. Such a detector is considered a dosimeter [14, 15].

The pulses obtained from the neutron detector were recorded with a scaler and, at the same time, observed on the screen of an oscilloscope which was synchronized with the trigger frequency of the microtron. Since the "lifetime" of neutrons before their recording is, in the paraffin cylinder, much longer than the duration of the bremsstrahlung pulse, the neutron pulses on the oscilloscope screen are statistically distributed, whereas the γ radiation pulses are synchronized with the frequency of microtron operation. The neutron detector was mounted in the hall of the microtron when the electron beam was extracted from the microtron and directed onto a slowing-down target surrounded by a lead trap. By varying the thickness of the lead walls, the flux ratio of γ quanta and neutrons could be changed. The P_γ value was measured with a DRG3-04 instrument. Up to an average counting rate of 10^4 sec^{-1} the neutron detector readings were linearly proportional to the electron current directed onto the bremsstrahlung target. At $P_\gamma = 500$ μR$\cdot$sec^{-1} on the scope screen there appeared a synchronizing pulse originaing from the bremsstrahlung pulse, but the pulse amplitude exceeded the level of the corona noise only by a factor of 2; the synchronizing pulse was still discriminated by the recording system having the threshold sensitivity recommended in the specification of the SNM-14 counter. In the case of microtron operation with a neutron converter in a graphite cube, nonlinearity resulting from counting losses was observed at counting rates in excess of $2.5\cdot10^4$ sec^{-1}.

An SNM-14 counter combined with a polyethylene moderator (wall thickness 124 mm and 0.6 mm cadmium layer at a depth of 55 mm in the moderating layer) was used as an active neutron dosimeter [16]. Indium-activation detectors in a paraffin sphere with a diameter of 280 mm [17] or in a polyethylene sphere with a diameter of 254 mm [13], as well as ^{6}LiF TLD together with ^{7}LiF TLD (TLD 600/700) in a polyethylene sphere with a diameter of 254 mm [18], were used as passive neutron dosimeters without counting losses.

36

Fig. 1

Fig. 2
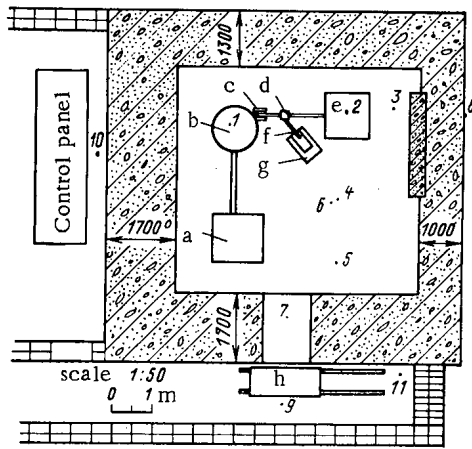
Fig. 1. Plan of the microtron site: a) high-frequency generator; b) microtron; c) outputting device with shield; d) switching magnet; e) graphite tube; f) γ channel; g) 20-cm-thick lead trap of the γ channel; h) roll door of brass (the figures denote the number of the point at which the radiation conditions were studied).
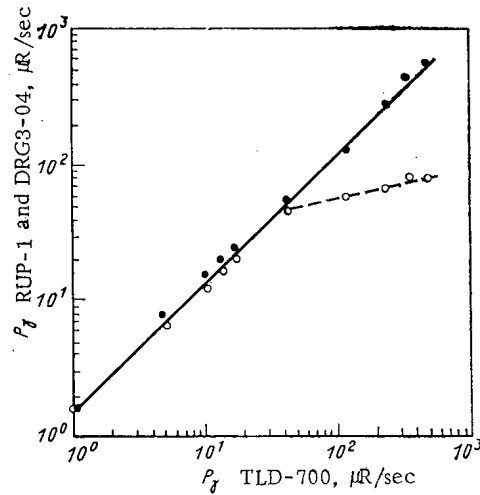
Fig. 2. Dosimeter readings in the microtron radiation field for instruments DRG3-01, DRG3-03, and DRG3-04 (●), and for RUP-1 with gamma detector (O), compared with readings for TLD-700.

Fig. 3

Fig. 4
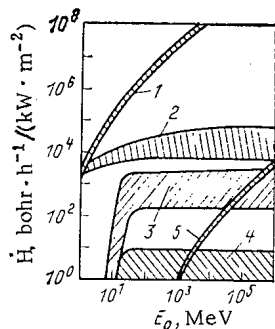
Fig. 3. Typical ratios of the equivalent dose rates $\dot{H}$ for various types of secondary radiation before the shield of electron accelerators of energy E_0: 1, 2) bremsstrahlung occurring under the angles 0° and 90° relative to the direction of the electron beam; 3) neutrons; 4) induced radioactivity; 5) muons (only under the angle 0°).
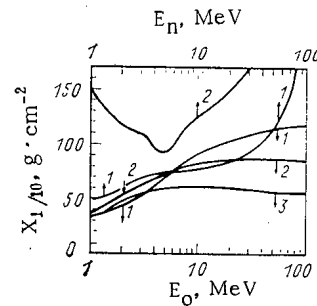
Fig. 4. Thickness values for tenfold attenuation in dependence upon the energy E_0 of accelerated electrons and the energy E_n of the neutrons: 1) conventional concrete; 2) steel; 3) lead.

The readings of the neutron dosimeters in the microtron radiation fields were verified by comparing with an equivalent dose determined from the energy spectrum of the neutrons. The neutron spectrum was restored by indium activation or with a TLD 600/700 pair in spherical polyethylene moderators of various diameters [19] and subsequent data processing with a program using the statistical regularization technique of [20]. Comparisons were made for microtron operation with a slowing-down target comprising a neutron converter and the graphite cube (mode 1), as well as for microtron operation with a bremsstrahlung target of the γ channel (mode 2). Neutrons with an energy below 1 keV dominate (~90%) in the spectrum of mode 1, whereas the spectrum is enriched by fast neutrons in mode 2. The readings were compared for all neutron detectors employed at points 7, 9, and 10 (Fig. 1); at points 3, 4, 5, and 6 the comparisons were made for detectors in the polyethylene sphere with the diameter of 254 mm.

37

It was observed that the SNM-14 neutron counter in the paraffin moderator with a wall thickness of 120 mm renders values which exceed the most probable dose by a factor of up to 10 in mode 1 and of up to 3 in mode 2. The SNM-14 counter in the combined polyethylene moderator renders values exceeding the most probable dose by a factor of up to 3 in mode 1 and at point 2 behind the rolling brass door in mode 2, whereas at the other points the readings of this counter in mode 2 coincide within the error limits with the most probable dose value.

When indium is used in the paraffin sphere with a diameter of 280 mm or in the polyethylene sphere with the diameter 254 mm, the values are too large by a factor of 2-2.5 in both modes of operation. The same value is observed with the TLD 600/700 pair in the polyethylene sphere with the diameter of 2.54 mm. Abnormally large readings of a dosimeter consisting of an SNM-14 counter in a cylindrical paraffin moderator seem to be related to the moderator design in the case of a "soft" neutron spectrum (the moderator comprises a transverse channel running through the center to accommodate the SNM-14 counter; therefore, the counter can be hit by slow neutrons which did not pass through the moderator).

RADIATION CONDITIONS

External Radiation. Bremsstrahlung is the main component in the radiation field of electron accelerators. This situation is illustrated in Fig. 3, which shows qualitatively typical ratios of equivalent dose rates normalized per unit power of the primary electron beam for various types of secondary radiation generated at a distance of 1 m from an unshielded target which is bombarded by electrons with the energy E_0 [21]. The width of the shaded area is affected by quantities such as the target material and the target thickness.

Figure 4 displays the length values for a tenfold attenuation of the equivalent dose in a broad bremsstrahlung beam for the cases of concrete, steel, and lead; the values refer to the angle 0° relative to the direction of the primary beam of electrons with the energy E_0 and are shown in dependence upon the energy of the electrons incident upon the heavy target [21]. Figure 4 also shows the length values for tenfold attenuation of the equivalent dose of neutrons in dependence upon the neutron energy E_n [22]. Obviously, in the case of concrete the length of the tenfold attenuation of the equivalent dose of bremsstrahlung generated by electrons with the energy $E_0 = 16$ MeV is about 100 g$\cdot$cm^{-2}, whereas in the case of photoneutrons with $E_n = 1$ MeV (average energy of the spectrum) the corresponding value is ~50 g$\cdot$cm^{-2}, i.e., the equivalent dose behind a concrete shield, as well as before the shield, results mainly from bremsstrahlung. The inverse situation is observed in the case of iron (steel, brass): the layer of tenfold attenuation of the equivalent dose of bremsstrahlung amounts to ~85 g$\cdot$cm^{-2} and to about 150 g$\cdot$cm^{-2} for 1 MeV neutrons; the irradiation conditions behind the shield are given only by the neutrons, not by the bremsstrahlung. Since the source of the secondary radiation of the electrons is local (slowing-down target—converter), a local shield, e.g., of lead, is conveniently employed for reducing the bremsstrahlung level in the hall; in this fashion the requirements to be satisfied by the main (concrete) shield can be reduced.

Local regions of bremsstrahlung unrelated to the target—converter were detected in the initial period of using the microtron as a radiation source. At an overall background level of ~0.1 μR$\cdot$sec^{-1} the value $P_\gamma = 15$ μR$\cdot$sec^{-1} was observed at the control panel (point 10; see Fig. 1) located opposite the microtron resonator. When the coil which adjusts the electron orbits and which is located near the resonator is poorly tuned, the P_γ value at point 10 increases up to 30 times. The distribution of the γ radiation dose rate behind the shield up to the wall which is perpendicular to the direction of the extracted beam was characterized by two peaks, which attests to still another local bremsstrahlung source besides the bremsstrahlung target. In order to establish this source, TLD dosimeters were exposed in the hall of the microtron (at 35 points) while the bremsstrahlung target was kept surrounded by a lead shield. As a result, a source was detected at the transition from the magnetic channel to the electron tube from which the beam with the final acceleration energy is extracted. In order to improve the radiation conditions, a local shield was inserted for the bremsstrahlung sources established: a 10 cm lead shield was placed inside the armored core of the microtron magnet opposite the resonator; the region of the transition from the magnetic channel to the electron tube was also protected by 10-cm-thick lead. Ten cm lead (along the path of the electrons) was inserted inside the graphite cube behind the slowing target—converter. This did not influence the distribution of both the thermal neutrons and the resonance neutrons inside the cube. The inner wall of the cube was laid out with 5-cm-thick lead bricks on a plane perpendicular to the beam axis. The wall portion which is perpendicular to the electron beam extracted toward the graphite unit e (see Fig. 1) was reinforced by 40 cm conventional

TABLE 1.   Neutron and γ Quanta Dose Rates
at Various Points of the Microtron Hall

Point of measurement (see Fig. 1)	Mode of operation	Neutrons, bohr·h^{-1}	γ radiation, $R \cdot h^{-1}$
1	1	20±10	1000
2	1	20±10	360
3	1	6,1±3,4	24
4	1	5,3±3,0	380
5	1	2,6±1,6	77
6	2	17,7±1,2	21
7	1	0,7±0,4	6
	2	3,9±0,4	18
8	1	—	$11 \cdot 10^{-3}$
9	1	$2,5 \cdot 10^{-3}$	$2 \cdot 10^{-3}$
	2	$(13,3\pm2,9) \cdot 10^{-3}$	$2,8 \cdot 10^{-3}$
10	1	$0,11 \cdot 10^{-3}$	$0,4 \cdot 10^{-3}$
	2	$(0,58\pm0,2) \cdot 10^{-3}$	$0,7 \cdot 10^{-3}$
11	1	$1,0 \cdot 10^{-3}$	$1,8 \cdot 10^{-3}$
	2	$(5,4\pm0,5) \cdot 10^{-3}$	$1,4 \cdot 10^{-3}$

TABLE 2.   γ Radiation Dose Rate at a Distance R from the Source Resulting from the Induced Activity of Microtron Elements, $\mu R \bullet sec^{-1}$

Time after stopping the microtron	On the surface of the graphite cube	Slowing-down tantalum target (R = 25 cm)	Near the magnet yoke above the resonator	Uranium converter (R = 50 cm)	Resonator (R = 30 cm)
10 min	50	2,2	1,2	120	1,2
30 min	36	0,9	1,0	—	0,6
1,5 h	15	0,6	1,0	—	0,25
10 h	2,2	0,4	<0,1	20	0,1
16 h	1,4	0,3	<0,1	—	<0,1
53 h	0,8	0,2	<0,1	1,6	<0,1
23 days	<0,1	<0,1	<0,1	1,6	<0,1

concrete (i.e., laid out with blocks).   Therefore, when the microtron was operated in mode 1, the γ radiation field behind the shield was practically homogeneous and the Pγ value decreased by a factor of about 50 relative to the maximum values.   In operation in mode 2, the bremsstrahlung target was protected by 20 cm lead disposed in the direction of the beam and by 15 cm lead on the sides.

The radiation levels at the points of monitoring are listed in Table 1 for the case of nominal operation of the microtron with an additional shield.   The neutron dose was estimated from the data of the neutron spectrum obtained with the multisphere technique of [19, 20]. The γ radiation dose in the hall of the microtron was measured with a TLD-700.

The integral neutron dose spectra observed at certain typical points of the microtron are shown in Fig. 5.   The "softest" neutron spectrum corresponds to operation in mode 1.   The neutron dose at points 9, 10, and 11 (see Table 1) was measured with a 10 inch moderator and increased by a factor of two to obtain the probable dose.

The "hardest" neutron spectrum is observed in mode 2 in the hall of the microtron.   Behind the shielding, the spectrum appears softened, but it is harder in a direction close to the direction of the primary electron beam.   The spectra at other points are of a type intermediate with respect to the curves shown in Fig. 5.   The dose rate of the neutrons and of the γ radiation near the building of the microtron amounted to 0.1–0.2 mbohr•h^{-1}.

It follows from Table 1 that the neutron dose behind the rolling brass door (see point 9 in Fig. 1) exceeds the dose of the bremsstrahlung radiation.   In such cases a shield or a labyrinth of about 0.5-m-thick conventional concrete should be placed before the entry.

Induced Activity.   The dose rate resulting from the induced activity was measured in the area of equipment elements at which the main electron losses occur, namely the slowing-down tantalum target, the uranium–beryllium converter of neutrons, the resonator, and the output-
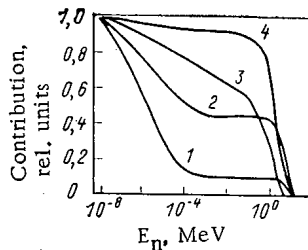
39

Fig. 5. Relative contribution of neutrons of energy E_n above a given energy to the total dose at the microtron: 1) points 3 and 4 (see Fig. 1), mode 1; 2) point 10, mode 2; 3) point 9, mode 2; 4) point 6, mode 2.

ting unit; measurements were also made near the graphite cube at the point at which a person stands while taking irradiated samples from the cube. It follows from the results of the measurements (Table 2) that the dose near the accelerator is given mainly by the activity of short-lived isotopes.

With the microtron disassembled and the resonator removed, P_γ inside the brass chamber and close to the walls amounted to 6-8 $\mu R \cdot sec^{-1}$ 10-15 min after switching off the microtron, but to only 0.3 $\mu R \cdot sec^{-1}$ after 17 days. Spectrometry performed with the aid of a Ge(Li) detector on the removed resonator showed only the presence of the ^{62}Cu ($T_{1/2}$ = 9.8 min) and ^{64}Cu ($T_{1/2}$ = 12.8 h) isotopes. When the dose rate near the uranium converter was measured 10 min after switching off the microtron, it was established that the main contribution to the short-lived component of the induced activity stems from ^{239}U radiation. Long-lived activity appears basically in that part of the uranium converter into which the beam of bremsstrahlung quanta enters (in Table 2, the P_γ value near this face of the uranium converter is listed). The opposite part of the converter is characterized by an activity which is lower by several orders of magnitude. The slowing-down target is replaced once every half year. The values listed in Table 2 refer to the end of its service life. One minute after switching off the microtron the dose rate of delayed uranium neutrons near the graphite cube amounts to about 3 mbohr$\cdot h^{-1}$, and it amounts to 0.2 mbohr$\cdot h^{-1}$ after 3 min.

Radioactivity of Air and Water. Activation of the air and the water was observed at E_0 > 10.55 MeV at the nitrogen of air and at E_0 > 15.67 MeV at the oxygen of the water, respectively. External radiation resulting from the radioactivity of the air and from the tubes with water (cooling system of the accelerator) is significantly weaker than irradiation caused by the induced activity of components and targets of the microtron. External radiation can be disregarded as a radiation hazard.

During operation, the concentration of radioactive aerosols in the hall of the microtron did not exceed $3.5 \cdot 10^{-16}$ Ci$\cdot$liter^{-1} (1 Ci = $3.700 \cdot 10^{10}$ Bq) in β activity and $1.7 \cdot 10^{-16}$ Ci$\cdot$liter^{-1} in α activity (background of the equipment). Inside the ventilation tube, at a distance of 3 m from the point of air intake from the hall, $P_\gamma \leqslant 50$ $\mu R \cdot h^{-1}$ immediately after switching off the microtron. Assuming that exchange ventilation does not take place, the calculated ^{41}Ar concentration amounts to ~$4 \cdot 10^{-10}$ Ci$\cdot$liter^{-1}, which is smaller than the admissible concentration of this isotope in the air of places of work by two orders of magnitude [23].

The value P_γ < 50 $\mu R \cdot h^{-1}$ was observed near the tube with the water for microtron cooling. A spectrometric analysis of the isotopes precipitated by iron hydroxide from 5 liters of water at pH = 8 was performed for 12 hours two days after taking a sample; measurements with a Ge-(Li) detector with a volume of 40 cm^3 did not reveal a measureable residual activity. Calculations made with the method of [24] have shown that the average annual concentration of radionuclides in the water cooling the microtron is below the admissible concentration of open water reservoirs when continuous operation of the microtron is assumed.

CONCLUSIONS

It could be concluded from our data that bremsstrahlung is the basic factor of radiation hazard during operation of a 16 MeV microtron. Although the dose rate behind the shield of the microtron hall can be significantly reduced with the aid of a local shield, the concrete walls should have a thickness of not less than 1.5 m. When a roll door of steel or brass is

40

employed, a concrete (or polyethylene) labyrinth should be provided before the door on the side of the hall. For the energies and power ratings of the electron beam indicated above, the level of the induced dose rate does not call for special measures in servicing, preventive maintenance, and repair work on the microtron although the induced activity of the uranium converter is rather high. The water cooling and ventilation systems of the microtron do not require any special elements for obtaining radiation safety, but considerable air exchange is necessary because a large amount of ozone is formed. Operational dosimetric monitoring of the radiation conditions on the microtron should be made for the γ radiation of the instrument with the DRG3-04 (or DRG3-01 and DRG3-03) instruments and for the neutrons with an instrument using a corona counter of neutrons together with a polyethylene moderator.

LITERATURE CITED

1. S. P. Kapitsa and V. N. Milekhin, The Microtron [in Russian], Nauka, Moscow (1969).
2. V. Ya. Vyropaev, JINR 14-9446, Dubna (1976).
3. Yu. N. Burmistenko et al., in: Accelerators [in Russian], Atomizdat, No. 10, Moscow (1968), p. 238.
4. V. N. Tsovbun, JINR 16-7104, Dubna (1973).
5. V. P. Kovalev, Secondary Radiation of Electron Accelerators [in Russian], Atomizdat, Moscow (1979).
6. K. Barker, Solid State Dosimetry, CRC Press, Ohio (1973).
7. M. Franz and V. Stolz, Solid-State Dosimetry of Ionizing Radiation [Russian translation], Atomizdat, Moscow (1973).
8. M. Ehrlich and C. Soares, NBS Technical Note 1119, Washington (1980).
9. B. N. Nemirovskii et al., Radiation Meters [in Russian], Atomizdat, Moscow (1972).
10. V. F. Kozlov, Handbook on Radiation Safety [in Russian], Atomizdat, Moscow (1977), p. 321.
11. M. M. Komochkov and M. I. Salatskaya, JINR R16-8175, Dubna (1974).
12. M. Zel'chinskii and K. Zharnovetskii, in: Neutron Monitoring, IAEA, Vienna (1967), p. 125.
13. L. S. Horn (Gorn) and B. I. Khazanov, Selective Radiation Meters [in Russian], Atomizdat, Moscow (1975).
14. De Pangher, J. Nucl. Instrum. Methods, 5, 61 (1959).
15. L. S. Zolin, JINR 2252, Dubna (1965).
16. Radiation Safety. Quantities, Units, Methods, and Instruments [in Russian], Atomizdat, Moscow (1974).
17. V. E. Aleinikov et al., JINR R16-6790, Dubna (1972).
18. J. Tuyn, in: Proc. 5th Int. Conf. on Luminescence Dosimetry, Sao Paolo (1977), p. 288.
19. V. E. Aleinikov et al., JINR R16-9123 [in Russian], Dubna (1975).
20. L.S. Turovtseva, "Solution of improperly stated inverse problems by statistical regularization (OBR-23 Program)," Preprint of the Inst. of Appl. Math., Acad. Science USSR (1975).
21. W. Swanson, Radiological Safety Aspects of the Operation of Electron Linear Accelerators, Technical Reports Series No. 188, IAEA, Vienna (1979).
22. M. M. Komochkov, JINR R16-7335, Dubna (1973).
23. Radiation Safety Standards NRB-76 [in Russian], Atomizdat, Moscow (1978).
24. M. M. Komochkov and Yu. G. Teterev, At. Energ., 34, No. 1, 17 (1973).

ELECTROMAGNETIC MASS SEPARATOR FOR RADIOISOTOPE SEPARATION

R. I. Lyubtsev, V. I. Orlov,
V. S. Belykh, A. G. Evdokimov,
V. N. Voichishin, G. A. Akopov,
V. Ya. Mishin, B. I. Rogozev,
M. K. Abdulakhatov, and E. M. Rubtsov

GENERAL CHARACTERISTICS OF THE SEPARATOR

The basic characteristics of the electromagnetic mass separator started up at the V. G. Khlopin Radium Institute are as follows:

Sector angle of the analyzing magnet, rad	2
Average radius of the ion trajectory, m	1.0
Distance from the foci to the effective boundary of the field, m	2.0
Ion current from the source, mA	1-10
Dispersion (for 1% $\Delta m/m_0$), mm	20
Resolution of mass peaks at half-height	1500
Relative enrichment	not less than 250

The mass separator was created based on the principles proposed in [1] and to a certain extent is analogous to the setup described in [2] and [3]. The difference lies in the fact that the mass separator examined here is intended for separation of radioactive isotopes. This determined the arrangement of the equipment and the remote control of its operation.

The working chamber, analyzing magnet, and vacuum system are situated in a special chamber (Fig. 1), equipped for first class work with radioactive substances. The vacuum system and the system for feeding the source of ions and other units and monitoring the operational regime of the setup are controlled from a control panel situated outside the zone where the work with the radioactive substances is performed. In order to simplify the periodic decontamination of the working chamber, a collapsible protective stainless steel liner is inserted into it.

In order to supply power to the analyzing magnet, a precision thyristor current source is used, which has considerable advantages over the usual generators. The instability of the current in the windings exciting the magnet in the case of prolonged operation does not exceed 0.02%. No devices are supplied at the source output for smoothing the current pulsations, but for current pulsation in the working region equal to 1.5%, the pulsation of the magnetic flux in the gap of the analyzing magnet does not exceed 10^{-3}%. This effect is explained by the smoothing action of the vortex currents in the massive magnetic circuit [4].

The setup is distinguished also by the fact that due to the interchangeable attachments on the pole end pieces, it is possible to separate isotopes of both heavy and medium mass (10-250 amu). The necessity for interchangeable attachments arises due to the change in the topography of the magnetic field in the gap of the analyzing magnet due to saturation of the steel in the pole end pieces when the current in the exciting windings changes. For this reason, in order to ensure focusing of the beam in the other mass range, it is necessary to change the shape of the pole edges.

We tuned the magnetic field of the setup by determining the topography of the field of a real magnet from the ion trajectories and correcting it [3]; the intensity of the field was measured by a method based on nutation of the total magnetic moment of protons [5]. The fine adjustment of the field was performed by the partial beam method [3] using a beam of lead ions. Due to the correction of the field, the resolution of the mass peaks at half-height reached 1500 with a quite good shape of the peaks. Measurement of the background between peaks showed that with the accumulation of nuclides, the relative enrichment will be of the order of 300.

In order to stabilize the regime of accumulation of isotopes and increase the quality of their separation, a two-electrode system for following the position of the beam was used in the setup [6].

An IR-la ion source, which is a universal double crucible source with an incandescent cathode, is used. In order to accumulate isotopes, a PP-1 detector is used [2].

The mass separator examined was used to obtain enriched preparations of ^{234}U and ^{119m}Sn.

SEPARATION OF URANIUM ISOTOPES

The starting substance for accumulating preparations of ^{234}U was uranium tetrachloride obtained by chlorinzation of U_3O_8 in the flow of carbon tetrachloride vapor. Purification was performed by sublimation in a vacuum.

In connection with the high hygroscopicity of uranium tetrachloride, after each separation operation it was necessary to decontaminate the source and to change the cathode. After contact with the atmosphere, a sharp decrease was observed in the electrical strength of the interelectrode gaps, and a degradation of the operational parameters of the tantalum cathode. When the source of ions was recharged with matter without removal from the working chamber (when the source was located in a dry nitrogen atmosphere), there was no disruption in its operation.

Stable and easily controlled operation of the ion source was achieved with a flow rate of matter of 140–160 mg/h. Such a flow rate of uranium tetrachloride was determined by an opening with a diameter of 1.2 mm in the output diaphragm of the crucible, whose working temperature was 320°C.

We checked the separation parameters in experiments on initial preparations with different content of ^{234}U, ^{235}U, and ^{238}U. The accumulation was conducted in copper accumulating boxes with slit dimensions 3 × 70 mm. Analysis of the preparations obtained showed that the coefficient of relative enrichment of neighboring isotopes was 250–270.

The utilization factor of matter (UFM) reached the highest values for large loads (7–9 g of tetrachloride, i.e., approximately 50 h of continuous operation) due to the relative shortening of the time for introducing the mass separator into the established working regime.

The starting preparation for accumulating ^{234}U was uranium with a content of 7.15 at.% of ^{234}U; the main impurity was ^{235}U. As a result of reprocessing, specimens of ^{234}U were obtained with isotopic purity up to 95·25%. The UFM for ^{234}U reached 4.8%, and the average value of the UFM for all reprocessing procedures was 4.4%.

Targets containing the preparations obtained were used in work on determining he nuclear-physical characteristics of ^{234}U [7, 8].

SEPARATION OF TIN ISOTOPES

Tin is a very inconvenient element to use in universal ion sources. With its low melting temperature, tin has a very high boiling temperature and cannot be used in an IR-la ion source. Tin chlorides and fluorides, on the contrary, have a very low boiling temperature. The most appropriate compound is tin dichloride $SnCl_2$; this is the compound chosen as the working substance.

The temperature at which the working pressure of tin vapor is created in the discharge chamber lies below the limit of the optimum temperature for the ion source. In order to decrease the conductivity of the vapor supply line, two diaphragms were mounted in the crucible with openings having diameter 0.8 mm. The substance was loaded into a quartz ampule, covered by a graphite plug with an opening with diameter 0.8 mm. Under these conditions, at a crucible temperature of 180–210°C, the flow rate of $SnCl_2$ vapor was in the range 70–90 mg/h, with satisfactory stability of the flow rate and controllability of the discharge. The ion current from the source in this case was 3–4 mA.

The resolution of the mass peaks at the focus of the setup, as in the range of heavy masses, is of the order of 1500; the UFM for separation of tin isotopes reached 7–10%. It should be noted that the UFM depends on the quality of the tin chloride prepared. If other tin compounds are present in the working substance, then this index decreases to 4–7%. The best indices were obtained with the use of a working compound purified by sublimation in a vacuum.

43
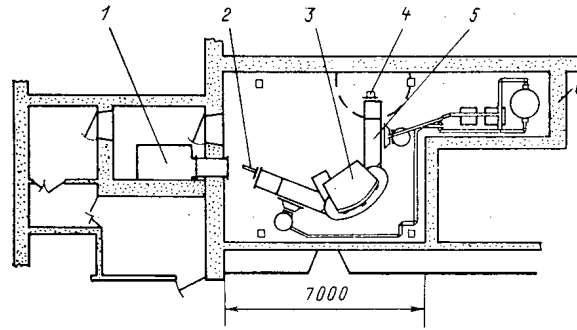
Fig. 1. Diagram of the arrangement of the equipment in the chamber: 1) box; 2) ion detector; 3) analyzing magnet; 4) ion source; 5) vacuum working chamber; 6) zone with maximum concentration of aerosols when the working chamber is opened (in the region of the ion source).
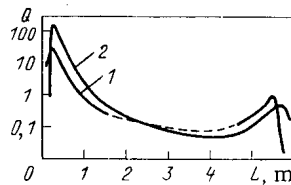
Fig. 2. Nature of the distribution of the surface contamination of the liner along the working chamber with separation of uranium (1) and tin (2) isotopes; the origin of the length of the working chamber is taken as the supporting flange of the ion source; the dashed line shows the interpolation of the section of the curve represented by the continuous line.

In order to accumulate ^{119m}Sn we used a mixture of isotopes with the following composition (at.%): 99.2 ^{118}Sn; 0.8 ^{119}Sn; 0.01 ^{119m}Sn; <<1 ^{113}Sn; <<1 ^{60}Co. The specific activity of the starting preparation was 0.5 Ci/g (1 Ci = $3.700 \cdot 10^{10}$ Bq). As a result of reprocessing, preparations of ^{119m}Sn were obtained with specific activity up to 40 Ci/g.

The tin isotopes were accumulated in copper accumulating boxes; the size of the input slit was 8 × 70 mm. The source operated in a stable steady-state regime for approximately 70% of the reprocessing time for a single charge. At the end of the separation process, in order to maintain the current from the source at a constant level, the power delivered to the crucible heater is gradually increased. Preparations of ^{119m}Sn obtained are intended for preparing Mössbauer sources.

RADIATION ENVIRONMENT

While performing radiationally dangerous work, involving breaking the hermetic seal of the working chamber (maintenance and decontamination of the ion source and liner, removal of accumulating boxes, etc.), we investigated the contamination of the air and the surfaces of the enclosure of the working zone, as well as the distribution of the surface contamination of the parts of the liner as a function of distance from the ion source (Fig. 2).

We analyzed the aerosol contamination of air at all stages of the isotope separation process. The aerosol concentration in the zone where the work was performed when the working vacuum chamber was opened increased with time in spite of the measures taken to reduce it: creation of a small flow of air directed into the chamber and use of polyethylene films to cover the ion sources and parts of the liner before they were transported. When evacuating the liner in the decontamination box after completion of the urnium isotope separation process, the aerosol concentration in the air in the zone noted in Fig. 1 (position 6) constituted 40 mBq/liter, with total activity of the reprocessed uranium equal to $4 \cdot 10^{8}$ Bq.

The total activity of the reprocessed ^{119m}Sn constituted 10^{11} Bq (2.5 Ci), but the aerosol emission into the atmosphere in the room was not observed over the entire duration of the work with this substance.

44

The activity of the surfaces in the enclosure of the working zone remained at the background level, with the exception of separate sections, where local contamination was noted up to 400 kBq/m^2 while working with uranium and tin.

The data examined lead to the conclusion that it is possible to use in the setup starting preparations with significantly higher activity. With some changes in the equipment, it is possible to enrich isotopes of such nuclides as plutonium, americium, and curium, as well as the fission products ^{85}Kr, ^{90}Sr, ^{93}Zr, ^{106}Ru, ^{135}Cs, ^{137}Cs, ^{144}Ce, for which, when it is necessary to obtain these preparations of high isotopic purity, electromagnetic separation, is apparently most efficient.

The nature of the distribution of the surface contamination of the liner in working with uranium and tin is shown in Fig. 2. The activity of the surfaces is shown along the ordinate axis in arbitrary units.

Thus, the S2 type electromagnetic mass separator permits separating radioactive isotopes in the interval 100–250 amu. The activity of the starting preparations for separation can reach 10 Ci and higher. The parameters of the separator achieved make it possible to separate isotopes with relative enrichment not less than 250. Isotopic preparations of uranium enriched in ^{234}U and tin enriched in ^{119m}Sn have been obtained.

LITERATURE CITED

1. A. F. Malov, V. A. Suzdalev, and E. P. Fedoseev, Zh. Tekh. Fiz., 35, No. 5, 914 (1965).
2. Production of Isotopes [in Russian], Atomizdat, Moscow (1973), p. 565.
3. A. F. Malov, V. A. Suzdalev, and E. P. Fedoseev, Prib. Tekh. Eksp., No. 2, 146 (1969)
4. L. A. Tikhomirov, "Investigation and development of thyristor precision constant current stabilizers for exciting magnetic fields," Author's Abstract of Candidate's Dissertation, LETI, Leningrad (1972).
5. A. I. Zhernovoi, Yu. S. Egorov, and G. D. Latyshev, Prib. Tekh. Eksp., No. 5, 71 (1958).
6. M. K. Abdulakhatov, G. A. Akopov, and V. S. Belykh, Preprint, V. G. Khlopin Radium Institute, RI-136, Leningrad (1980).
7. A. M. Geidal'man et al., in: Abstracts of Reports at the 30th All-Union Conference on Nuclear Spectrometry and Nuclear Structure, Nauka, Leningrad (1980), p. 149.
8. A. M. Geidal'man et al., Izv. Akad. Nauk SSSR, 44, No. 5, 927 (1980).

DETERMINATION OF THE COEFFICIENT OF ISOTOPE SEPARATION IN CHEMICAL EXCHANGE
BY THE METHOD OF MULTISTAGE EXTRACTION

S. D. Moiseev, V. A. Samoilov,
and Yu. I. Ostroushko

The method of multistage extraction of isotope mixtures [1-3] is widely used for determining the coefficient of separation of the isotopes in chemical-exchange processes; a diagram of the method is shown in Fig. 1.

The initial mixture, containing A_{init} and B_{init} moles of the isotopes in the mixture, is separated in the first extraction stage into two fractions, one of which contains $\overline{A}_1$ and $\overline{B}^1$ moles of the isotopes and is enriched in the isotope A being extracted. The second, the depleted fraction, contains A_1 and B_1 moles of these isotopes. After this, the fraction which has been enriched once already is subjected to a second enrichment, for which it is again separated into two fractions, which contains $\overline{A}_2$ and $\overline{B}_2$ moles (the enriched fraction) and A_2 and B_2 moles of the isotopes, respectively. After going through the required number of extraction stages, we obtain in the last enriched fraction a small amount of an isotope mixture $\overline{A}_n$ and $\overline{B}_n$ with such a large difference in isotopic composition from the initial mixture that it can be reliably detected with the currently available methods of analysis. To obtain an even greater difference in the isotopic composition of the final samples, we can carry out

---

a stage-by-stage extraction of the isotope mixture in the depleted branch as well. To do this, we subject the depleted fraction of the first stage to a multistage depletion process by separating it at each stage into an enriched and a depleted fraction, with removal of the enriched fraction at each stage. In this case we analyze the final enriched and depleted fractions. The presence of two branches in the experiment increases the accuracy of the analytic determination, but it makes the experiment much more complicated. Therefore, we have considered only the calculation of the enriching branch.

Despite the fact that in various studies devoted to the determination of the coefficient of separation of isotopes by multistage extraction the investigators considered essentially the same scheme for the process, the calculation formulas differ greatly, since they reflect different experimental conditions, and different assumptions are made in deriving the final formula. Thus, in [4] the calculation formula is obtained for the enriching branch for the case in which the initial amount of the isotope being produced is small and the amounts removed at all the stages are equal:

$$\alpha = \frac{t}{t-1+\sqrt[n]{\frac{x_0}{y_n}}}, \tag{1}$$

where α is the isotope separation coefficient; t, ratio of the number of moles in the depleted fraction to the total number of moles before the separation process in the stage under consideration; n, number of extraction stages; and x_0, y_n, respectively, the mole fraction of one of the isotopes in the initial mixture and in the final enriched fraction.

The authors of [3] propose a more accurate but also more difficult method of graphical analysis. The graphical construction in the coordinates y and x is carried out for given values of α and n; as a result, we can find the final mole ratio y_n of the isotopes in the mixture. If the calculated y_n does not agree with the experimental value, the calculation is repeated with a new value of α.

Another proposed calculation formula is a relatively simple one, in which we assume as an approximation that the products of the mole fractions of the isotopes in the equilibrium fractions at all the stages are equal [5]. For the enriching branch we have

$$\varepsilon = \frac{y_n - y_{init}}{\bar{y}(1-\bar{y})\sum_0^n \Theta_i}, \tag{2}$$

where $\bar{y} = 1/2(y_n + y_{init})$; $\varepsilon = \alpha - 1$ is the enrichment factor; and Θ_i, number of moles of the mixture which have been carried into the depleted fraction divided by the number of moles of the mixture which enter the stage under consideration. To obtain the corrected enrichment factor ε', the value of ε calculated by formula (2) must be divided by $1 - \varepsilon$, i.e.,

$$\varepsilon' = \frac{\varepsilon}{1-\varepsilon}. \tag{3}$$

In calculating the enriching branch, the product of the mole fractions of the isotopes in the equilibrium fractions is also set equal to the product of the average values of the mole fractions of the isotopes in the enriched fractions.

All the approximations made in the calculation formulas lead to corresponding errors in the calculations. In the proposed method for approximately calculating α we assume not that the amount of mixture removed is constant, as in [4], but that the amount of the isotope being extracted is constant, although in the removal during the experiment and in the analytic check of the removal we consider the sum of the isotopes, i.e., the assumption reduces to the equality $\Theta_{AB} \approx \Theta_A$.

The initial quantities for calculating α are the constant amount of isotope A removed into the second phase ($\Theta_A = A_i/A_{i-1} = const$) and the total enrichment in isotope A in the first phase after n extraction stages (β_Σ). To derive the calculation formula, we set up the following system of equations describing the conditions under which the extraction process is carried out:

$$\alpha = \frac{\bar{A_i}B_i}{\bar{B_i}A_i}; \tag{4}$$

46

$$\beta_i = \frac{A_i \; \overline{B}_{i-1}}{B_i \; \overline{A}_{i-1}} ; \tag{5}$$

$$\Theta_A = \frac{A_i}{A_{i-1}} ; \tag{6}$$

$$\overline{A}_{i-1} = \overline{A}_i + A_i; \tag{7}$$

$$\overline{B}_{i-1} = \overline{B}_i + B_i. \tag{8}$$

In this system Eqs. (4) and (5) determine α and β at stage i, and Eqs. (7) and (8) describe the balance with respect to each of the isotopes. Solving this system, we find

$$\alpha = \frac{1}{\Theta_A}(\beta_i - 1) + 1. \tag{9}$$

The total enrichment is determined by the following equations:

$$\beta_\Sigma = \frac{\overline{A}_n \; \overline{B}_{\text{init}}}{\overline{B}_n \; \overline{A}_{\text{init}}} = \frac{\overline{A}_1 \; \overline{B}_{\text{init}}}{\overline{B}_1 \; \overline{A}_{\text{init}}} \frac{\overline{A}_2 \; \overline{B}_1}{\overline{B}_2 \; \overline{A}_1} \cdots \frac{\overline{A}_n \; \overline{B}_{n-1}}{\overline{B}_n \; \overline{A}_{n-1}}, \text{i.e.}, \beta_\Sigma = \beta_1 \beta_2 \cdots \beta_n. \tag{10}$$

From Eq. (9) it follows that β_i at each stage is constant, since by the conditions of the experiment, Θ_A is taken to be constant. Consequently, $\beta_\Sigma = \beta_i^n$ or

$$\beta_i = \sqrt[n]{\beta_\Sigma}. \tag{11}$$

Taking account of (11), we can represent Eq. (9) in the form

$$\alpha = \frac{1}{\Theta_A}(\sqrt[n]{\beta_\Sigma} - 1) + 1. \tag{12}$$

If in the initial system of equations we replace Eq. (6) with the equation

$$\Theta_B = \frac{B_i}{B_{i-1}}, \tag{13}$$

i.e., if we take the extracted amount of the second isotope to be constant, we obtain the expression for α in a different form:

$$\alpha = \frac{\Theta_B \sqrt[n]{\beta_\Sigma}}{1 - \sqrt[n]{\beta_\Sigma}(1 - \Theta_B)}. \tag{14}$$

In order to verify the above formulas and compare them with previously published methods of calculation, we worked out a program of stepwise analytic calculation of the process of multistage extraction which simulates the real process. Using the analytic method, we calculated each extraction stage before the final isotope composition y_n was obtained. We then compared with the given value of y_n all the y_n obtained by different calculation methods. The initial quantities for the calculation are α, the separation factor in the chemical-exchange system; $\overline{A}_{\text{init}}$ and $\overline{B}_{\text{init}}$, the initial numbers of moles of the isotopes in the mixture; and Θ_{AB}, the relative amount of the isotope mixture extracted, at each contact in a given stage, from the initial number of moles, into the other phase. In this case

$$\frac{A_i + B_i}{\overline{A}_{i-1} + \overline{B}_{i-1}} = \Theta_{AB}. \tag{15}$$

Taking account of (7) and (8), we can write Eq. (4) in the form

$$\frac{\overline{A}_i (\overline{B}_{i-1} - \overline{B}_i)}{\overline{B}_i (\overline{A}_{i-1} - \overline{A}_i)} = \alpha$$

or

$$\overline{B}_i = \frac{\overline{A}_i \; \overline{B}_{i-1}}{\overline{A}_i + \alpha (\overline{A}_{i-1} - \overline{A})}. \tag{16}$$

Making use of (7) and (8), we can easily transform Eq. (15):

$$\frac{(\overline{A}_{i-1} + \overline{B}_{i-1}) - (\overline{A}_i + \overline{B}_i)}{\overline{A}_{i-1} + \overline{B}_{i-1}} = \Theta_{AB};$$

47

substituting B_i from Eq. (16), we obtain

$$1-\frac{\overline{A}_i}{\overline{A}_{i-1}+\overline{B}_{i-1}}-\frac{\overline{A}_i\,\overline{B}_{i-1}}{[\overline{A}_i+\alpha\,(\overline{A}_{i-1}-\overline{A}_i)]\,(\overline{A}_{i-1}+\overline{B}_{i-1})}=\Theta_{AB}. \qquad (17)$$

Equation (17) can be reduced to the form

$$k\overline{A}_i^2+b\overline{A}_i+c=0, \qquad (18)$$

from which we find A_i.

Thus, our stepwise analytic calculation consisted of the following: Knowing the initial amounts of the isotopes in the mixture, $\overline{A}_{init}$ and $\overline{B}_{init}$, we determined $\overline{A}_1$ and $\overline{B}_1$, then $\overline{A}_2$ and $\overline{B}_2$, etc.

To simplify the calculations, as in [5], we took $(\Theta_{AB})_i = (\Theta_{AB})_j = 0.5$ and $\varepsilon = 0.05$ and 0.1 for a number of initial isotope concentrations. The calculations were carried out for formulas (1), (2), (3), (12), and (14), and also for formula (14) using the total enrichment β'_Σ instead of β_Σ:

$$\beta'_\Sigma=\frac{1}{\beta_\Sigma}. \qquad (19)$$

For each formula investigated, we calculated the enrichment factor $\varepsilon = \alpha - 1$, with the aid of the previously obtained stepwise analytic calculations of the values y_n, i.e., the final isotope concentration in the mixture, and we also determined the relative error characterizing the accuracy of the formula $\delta\varepsilon = (\varepsilon - \varepsilon_0/\varepsilon_0)\cdot 100\%$; we found ε_0 from the conditions of formula (17) of the stepwise calculation. The calculated results are shown in Table 1. It can be seen that the accuracy of the calculation by formulas (2), (3), (12), (14), and (19) is affected not by the regions of isotope concentration but mainly by the separation factor α (or ε). When α increases by a factor of two, the accuracy of the indicated formulas is reduced also by a factor of almost two. On the other hand, the accuracy of formula (1) decreases sharply as α decreases. Moreover, it can be said that for any of the isotope concentrations considered, the highest accuracy is obtained by using formula (14) with the correction (19) — the largest relative error is +1.4%, which is little more than half the relative error of the other formulas.

Thus, it can be observed that the assumption $\Theta_{AB} \approx \Theta_A$ made in deriving formulas (12) and (14) leads to smaller errors in the calculations than the assumptions in formulas (1)-(3). We can estimate the error introduced by these assumptions, i.e., show the connection between Θ_{AB} and Θ_A, by using Eq. (17). Dividing the numerator and the denominator of the second term by $\overline{A}_{i-1}$ and of the third by $\overline{A}_{i-1}\overline{A}_{i-1}$, and writing $\overline{A}_i/\overline{A}_{i-1} = 1 - \Theta_A$, and $\overline{B}_{i-1}/\overline{A}_{i-1} = K$, we can write Eq. (17) as follows:

$$1-\frac{1-\Theta_A}{1+K}-\frac{(1-\Theta_A)\,K}{\{[(1-\Theta_A)+\alpha\,[1-(1-\Theta_A)]\}\,(1+K)}=\Theta_{AB}. \qquad (20)$$

After transformation, this equation reduces to the form

$$C\Theta_A^2+l\Theta_A+d=0. \qquad (21)$$

If, for example, we take $\overline{B}_{i-1} = 0.93$, $\overline{A}_{i-1} = 0.07$, $\alpha = 1.02$, and $\Theta_{AB} = 0.5$, then the value of Θ_A is equal to 0.4937, i.e., when Θ_{AB} is replaced by Θ_A, we have an error of 1.25%, which does not exceed the error of the usual chemical analysis conducted to determine Θ_{AB} at each stage.

Making use of Eqs. (12) and (14), we can take optimal conditions for conducting the experiment with multistage extraction for each concrete case. The choice of the conditions is determined by the accuracy of the isotope-analysis method, by the final amount of material required, and, lastly by the practically most acceptable ratio between the amount extracted at each stage and the number of stages.

For such an analysis we must specify the total enrichment β_Σ. It must be sufficient for obtaining the required accuracy. For example, we could specify $\beta_\Sigma = 1.05$.

One of the main problems that must be solved in carrying out the multistage extraction experiment is the choice of the optimal ratio between the amount of material extracted at each stage and the necessary number of stages. This ratio is determined by the equation
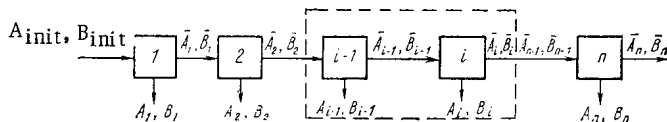
48

Fig. 1. Diagram of the process of multi-stage extraction of an isotope mixture.

TABLE 1. Extraction of the Isotope Mixture along the Enriching Branch

$10^2 \varepsilon$ given	u_{init}	u_n	Number of stages	$10^2 \varepsilon$ (1)	$\frac{\varepsilon-\varepsilon_0}{\varepsilon_0} 100\%$ (1)	$10^2 \varepsilon$ (2)	$\frac{\varepsilon-\varepsilon_0}{\varepsilon_0} 100\%$ (2)	$10^2 \varepsilon$ (3)	$\frac{\varepsilon-\varepsilon_0}{\varepsilon_0} 100\%$ (3)	$10^2 \varepsilon$ (12)	$\frac{\varepsilon-\varepsilon_0}{\varepsilon_0} 100\%$ (12)	$10^2 \varepsilon$ (14)	$\frac{\varepsilon-\varepsilon_0}{\varepsilon_0} 100\%$ (14)	$10^2 \varepsilon$ (14)	$\frac{\varepsilon-\varepsilon_0}{\varepsilon_0} 100\%$ (19)
5	0,0753	0,1048	15	5,21	+4,1	4,80	—3,996	5,04	+0,84	4,89	—2,00	4,89	—2,0	5,02	+0,4
5	0,2611	0,31051	10	4,33	—13,4	4,84	—3,18	5,09	+1,7	4,91	—1,84	4,91	—1,8	5,03	+0,6
10	0,2624	0,32071	6	9,72	—2,79	9,4	—5,9	10,39	+3,87	9,66	—3,4	9,66	—3,4	10,14	+1,4
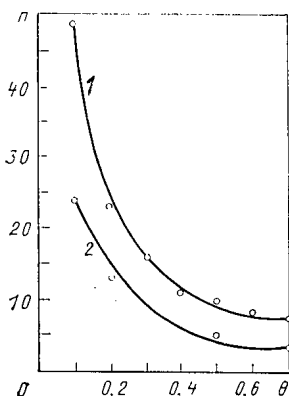
Fig. 2. Relation between the number of stages and the amount extracted at each stage when $\beta_\Sigma = 1.05$ for: 1) $\alpha = 1.01$; 2) $\alpha = 1.02$.

$$\beta_\Sigma = [\Theta_A (\alpha - 1) + 1]^n, \tag{22}$$

which follows from (12). We can consider two systems with $\alpha = 1.01$ and $\alpha = 1.02$. Figure 2 shows the two curves in the coordinates $n - \Theta$ corresponding to these systems. As can be seen, for the system with $\alpha = 1.01$ the total enrichment $\beta_\Sigma = 1.05$ can be obtained if at each stage we extract 10% of the isotope mixture entering it. In this case the number of stages is 49. A similar enrichment can be obtained if at each stage we extract 20% of the isotope mixture in the case of 24 extraction stages, or 70% of the isotope mixture in the case of 7 stages.

For a more effective system of chemical exchange with $\alpha = 1.02$, the enrichment $\beta_\Sigma = 1.05$ obviously can be attained by extracting 10% of the isotope mixture at each of 24 extraction stages, or 70% of the isotope mixture at each of three stages.

These relations follow from the general relation between β and Θ in the case of one-time contact. In this case, as can be seen from (22), for n = 1, the value of β varies linearly from 1 to α when Θ varies correspondingly from 0 to 1.

It is obviously desirable to construct the multistage-extraction experiment in such a way that the number of extraction stages will be a minimum. However, this is limited by the neeessity of obtaining a specified absolute quantity of the material in order to conduct the final isotope analysis with sufficient accuracy. For example, after 49 extraction stages, with extraction of 10% of the isotope mixture at each stage, from an initial isotope mixture of G_{init} = 1000 moles there remains G_{fin} = 6.0 moles, and after 7 extraction stages with extraction of 70%, there remains G_{fin} = 0.22 moles.

49

Thus, by using the proposed equations (12) and (14), we can conduct a preliminary analysis of the investigated system of chemical exchange in order to choose suitable conditions for the practical realization of the multistage extraction, and, determining β_Σ from the final composition of the isotope mixture, we can find the isotope separation factor α

LITERATURE CITED

1. A. M. Rozen and A. I. Mikhailichenko, Zh. Fiz. Khim., 64, No. 7, 1737 (1970).
2. G. M. Panchenkov, V. D. Moiseev, and A. V. Makarov, ibid., 31, No. 8, 1851 (1957).
3. G. K. Boreskov and S. G. Katal'nikov, ibid., 35, No. 6, 1240 (1961).
4. E. M. Kuznetsova, A. V. Makarov, and G. M. Panchenkov, ibid., 32, No. 11, 2641 (1958).
5. A. I. Mikhailichenko and O. F. Shcheglov, ibid., 62, No. 1, 164 (1968).

DEPTH DISTRIBUTION OF HYDROGEN IN METALS BY THE p-p SCATTERING METHOD

V. N. Kadushkin, Z. P. Kiseleva,   UDC 539.171.112
G. A. Radyuk, B. G. Skorodumov,
I. I. Trinkin, V. A. Shpiner,
P. K. Khabibullaev, and V. N. Serebryakov

In recent years interest in investigation of the metal-hydrogen system has intensified, this being associated with the solution of a number of problems in nuclear, thermonuclear, and hydrogen power engineering. For research on the behavior of hydrogen in metals there has been an intensive development of nondestructive nuclear-physical methods of measuring the depth distribution of hydrogen in materials, using neutrons and especially ions as the analyzing particles [1-4]. In our work we investigated the depth distribution of hydrogen in specimens of copper, titanium, and palladium by the method of proton-proton scattering with recording of the scattered particles in coincidences [2, 5].

The experimental setup for measuring the hydrogen concentration in the metals is shown in Fig. 1. The specimens to be studied and standard targets are mounted on a rotary table inside the scattering chamber. Figure 1 shows the case when the process of dissolution of hydrogen in palladium is investigated; a palladium wafer 100 µm thick is vacuum-sealed in a special cell which is filled with hydrogen to the required pressure.

A beam of 18-MeV protons, collimated into a filament 1 mm in diameter, enters the cell through an iron foil 30 µm thick. Silicon-lithium detectors D_1 and D_2, with an effective area diameter of 12 mm and a sensitive-region depth of 2 mm, and placed at an angle of $\pm 45°$ to the direction of the incident beam (angular aperture of detector ± 0.1 rad), record events of scattering on hydrogen contained in the palladium. Since coincidence events are selected, scattering on the material of the specimen is present in the spectra only in the form of random coincidences, since divergence of the scattered particles by an angle of 90° in the laboratory system of coordinates is attained only with p-p scattering. A detector M of the same kind was used to monitor the incident proton beam from the elastic peak of scattering from iron foil 7 µm thick.

The circuit for selecting coincidences consisted of two VF-3 time shapers, designed at the Institute for Nuclear Research, Academy of Sciences of the Ukrainian SSR, a time-to-amplitude converter, and a differential discriminator which controlled the linear transmission circuits in the spectrometric channels of the detectors. The energy spectra and the signal of the monitor were fed into an IVK-2 measuring-computer, recording coincident events in a field measuring 64 × 64 channels.

The time resolution of the pair of detectors was first checked with a thin hydrogen-containing target and then was checked with a compound target which made it possible to give the entire necessary energy range. The resolution was 5 and 18 nsec for the tin and compound targets, respectively.

The Detection Limit. The possibility of detecting hydrogen is determined by the relation between real and random coincidences. It was shown in [5] that a detection limit of 10^{-6} H atoms/Me atom was attained by using an accelerator with a continuous particle beam. We shall make an analogous estimate of this limit for the use of a cyclotron with a current-pulse repetition rate $\nu = 15$ MHz, operating in a modulated regime with a duty factor $\eta = 10$. The load factor of each detector is proportional to the differential cross section σ_p for the interaction of the protons with the material of the specimen,

$$N = k\sigma_p, \tag{1}$$

where k depends on the beam current, the solid angle of the detector, and the thickness of the specimen.

The number of real coincidences is determined by the hydrogen scattering cross section σ_H and the ratio of the number of hydrogen atoms to the number f of atoms of the matrix of the specimen:

$$n = k\sigma_H f. \tag{2}$$

The probability of detection of random coincidences per second is

$$n_r = N^2 \eta / \nu F^2, \tag{3}$$

where F is the part of the detector load that falls in the energy range in which cases of scattering on hydrogen are observed ($F \approx 0.1$).

Then

$$\frac{n}{n_r} = \frac{f\sigma_H}{F^2 k \sigma_p^2} \frac{\nu}{\eta} = \frac{f}{F^2 N} \frac{\nu}{\eta} \frac{\sigma_H}{\sigma_p}. \tag{4}$$

For nuclei of average mass $\sigma_H/\sigma_p \approx 1$ and with $N = 10^4 \ \mathrm{sec}^{-1}$, we have

$$f \sim 10^{-4} \frac{n}{n_r}, \tag{5}$$

i.e., reliable determination of hydrogen (when real coincidences exceed random coincidences tenfold) is possible only at a level of 10^{-3} H atoms/Me atom. The use of two-dimensional analysis increases the sensitivity by approximately an order of magnitude because of the scattering of random coincidences over the entire field. The advantage of using accelerators with a continuous beam and the necessity of reducing the duty factor of pulsed accelerators are obvious. With an increase in the detector load, the speed of the analysis improves, but the ratio of real to random coincidences increases.

Let us point out, moreover, that under real conditions the number of coincidences is always smaller than the value determined by formula (2). The number of real coincidences is n only for an infinitely fine beam and in the case of absolutely exact alignment of the beam—target—detectors system in the plane of the reaction. It is, therefore, necessary to work with the narrowest possible beam and to align the system carefully.

Resolution and Depth of Analysis. When the detectors are set up at an angle of $\pm 45°$, the energy E of a detected proton is related to the depth of the location of the hydrogen atom on which scattering occurs:

$$X = (2^{\beta+1/2} - 1)^{-1} [t2^{\beta+1/2} - \alpha (E_0^\beta - 2^\beta E^\beta)], \tag{6}$$

where α and β are constants from the known relation between the range of the particle and its energy for the given material ($R = \alpha E^\beta$); E_0 is the energy of the incident protons; t, thickness of the specimen; and X, depth at which proton collision occurred. Differentiating Eq. (6), we obtain

$$dE = dX \frac{2^{\beta+1/2} - 1}{\alpha \beta 2^\beta} \frac{1}{E^{\beta-1}}, \tag{7}$$

whence it follows that the depth resolution (energy shift dE when the depth changes by dX) depends on the energy E of the detected protons (or on the coordinate X). Formulas (6) and (7) enable the measured energy spectrum to be converted to the depth distribution by means of the relation
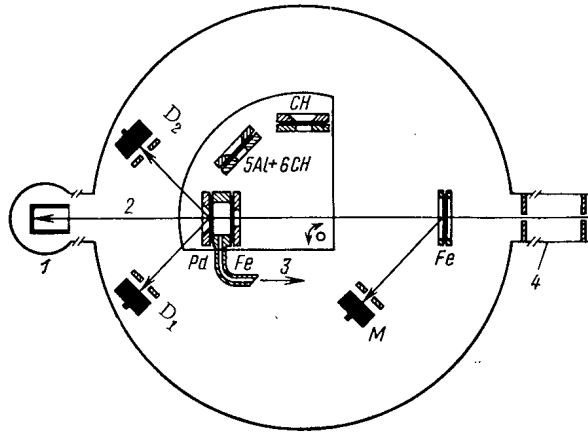
51

Fig. 1. Experimental setup: 1) Faraday cylinder; 2) protons; 3) to supply system; 4) collimator.

$$N(X) = N(E)\, dE/dX(E). \tag{8}$$

At an incident proton energy of 20 MeV for titanium the depth resolution with a spectrometer energy resolution of 200 keV will vary from 3 to 13 µm. In a real situation, however, the resolution is worse and varies little over the depth of the specimen. This is explained by the straggling of the energy losses and the influence of multiple scattering with a finite angular aperture $\Delta\Theta$ of the detectors in the horizontal plane. Let us elucidate the latter.

Because of multiple scattering, a particle can deviate from the initial trajectory and leave the specimen at a different angle within the limits of the angular aperture of the detector. This leads to different energy losses of particles emerging in different directions. If the mean free path of the particles in the specimen is l, then the maximum difference of the lengths of the trajectories is $l\Delta\Theta$ and, therefore, the energy of particles emerging from one and the same point of the specimen can differ by $\Delta E = l\Delta\Theta S$, where S is the mean stopping power of the material of the specimen. When l = 200 µm and $\Delta\Theta$ = 0.1 rad, the maximum change in the energy losses because of this reaches ~500 keV.

Meanwhile, it can be easily shown that the maximum path difference in the material of the specimen in the vertical plane is $l(\Delta\varphi)^2$, i.e., identical deterioration of the resolution is obtained when

$$l\Delta\Theta = l(\Delta\varphi)^2. \tag{9}$$

It is thus clear that it is better to work with the detector diaphragms in the form of vertical slits whose dimensions are determined by the solid angle and formula (9).

The maximum thickness of the specimens is determined by the energy E_0 of the accelerated protons, the energy threshold E_{thr} in the spectrometric channels of the detectors, the angular aperture of the detectors, and the stopping power of the material under study:

$$t_{max} = \alpha \cos(\Theta + \Delta\Theta)\{[E_0 \cos^2(\Theta + \Delta\Theta)]^\beta - E_{thr}^\beta\}; \tag{10}$$

for $\Delta\Theta$ = 0.1 rad, E_0 = 20 MeV, and E_{thr} = 1 MeV for titanium , copper, and palladium, t_{max} = 180, 100, and 90 µm, respectively. The use of vertical slits instead of round diaphragms, with the size of the solid angle preserved, leads to a decrease in $\Delta\Theta$ and, therefore, to an increase in the maximum depth of analysis.

Allowance for Multiple Scattering. Since the methods of detecting hydrogen are based on correlation measurements, because of multiple scattering the greater the thickness of the material traversed by the particles en route to the detectors, the greater the coincidence counting losses. In [5] it was found that the number of coincidences decreases exponentially when specimens with a uniform hydrogen content are used. Investigations carried out with various materials showed that with uniform distribution of hydrogen inside the specimen the number of coincidences detected can be written as
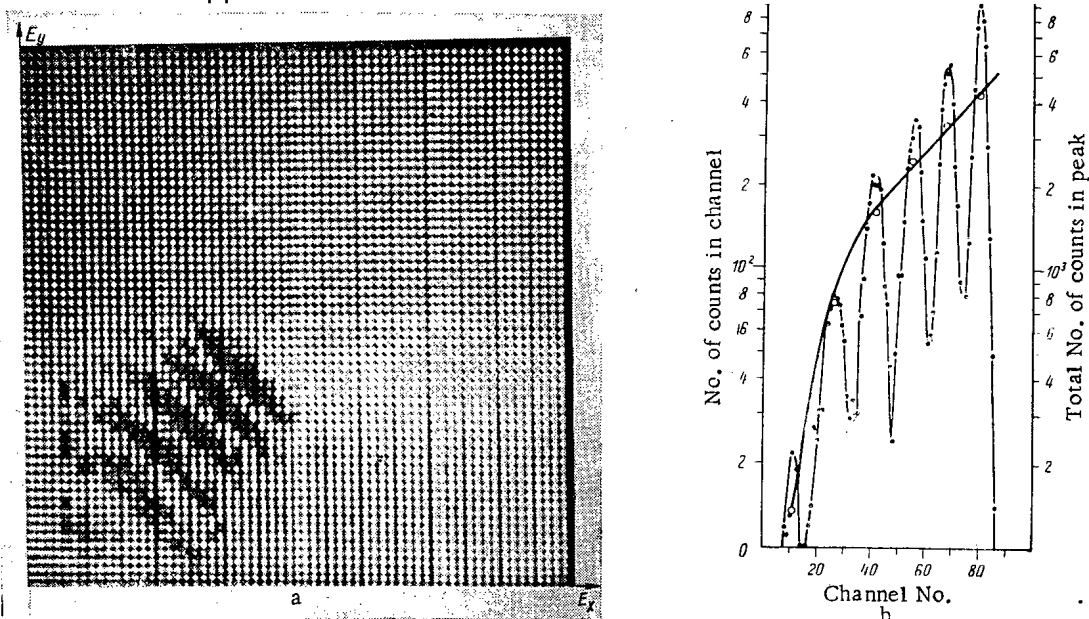
Fig. 2. Energy spectrum of coincidences, obtained on a target of six polystyrene films, with five layers of 50-μm aluminum foil interposed between them: a) screen of graphic display — the dark lines correspond to the six polystyrene films, the first corresponding to the film at the exit of the beam from the target, while the sixth (poorly visible with the given interpolation) corresponds to the film on the entrance side of the target; b) projection on axis of total energy (right-hand scale for the solid line), carried out by eye according to the bright points (totals of counts at the peaks) — the dark spots represent the number of counts in the channel.

$$N = N_0 \exp \left(-\delta \langle \chi^2 \rangle \right), \tag{11}$$

where $\langle \chi^2 \rangle$ is the rms angle of multiple scattering, and δ is a constant determined by the geometry of the measurements. When the detectors have a small angular aperture the constant δ attains large values, which leads to substantial counting losses for a large thickness of the specimen.

For small energy losses ΔE the angle of multiple scattering depends linearly on the value of these losses:

$$\langle \chi^2 \rangle \sim \Delta E / E. \tag{12}$$

For "thick" specimens or large energy losses the angle of multiple scattering can be estimated by integrating this expression over the entire thickness:

$$\langle \chi^2 \rangle \sim \int_0^l \frac{dE}{E} = -\ln \left(1 - \frac{\Delta E}{E} \right). \tag{13}$$

For our geometry ($\Theta = \pm 45°$) we have

$$\langle \chi^2 \rangle \sim \frac{1}{\beta} \ln \left[1 - \frac{(l-X) v^{\beta+1/2}}{\alpha E_0^\beta - X} \right]. \tag{14}$$

It follows from formulas (11)-(13) that energy spectra obtained for specimens containing hydrogen which is uniformly distributed over their depth will be exponential at low energy losses (on the right-hand part of the spectrum).

Figure 2a shows a photograph of the graphic display of the IVK-2 after recording the two-dimensional energy spectrum of p–p coincidences from a compound target consisting of six 18-μm polystyrene foils and five 50-μm aluminum foils. The energy spectra of the coincidence-controlled detectors D_1 and D_2 were applied to the X and Y axes of the analyzer. In Fig. 2b this spectrum has been projected onto the axis of the total energy, which is proportional to the sum of the channel numbers along the analyzer axes. The shape of the solid line drawn

53
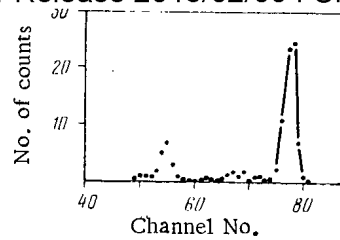
Fig. 3. Energy spectrum of coincidences,
obtained from a copper specimen.
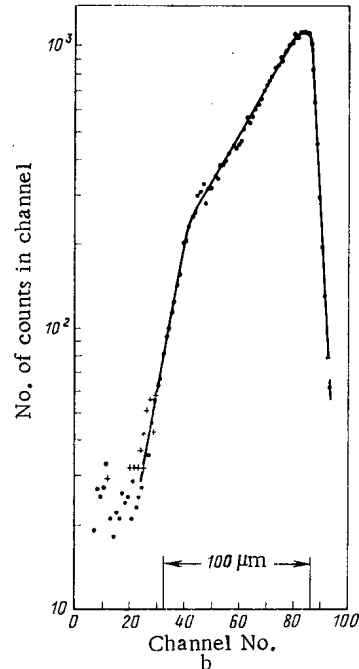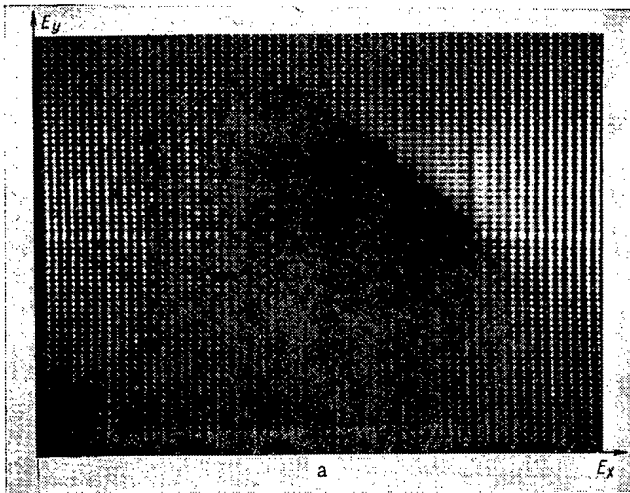
Fig. 4. Energy spectrum of coincidences, obtained from a palladium specimen: a)
screen of graphic display; b) projection onto axis of total energy.

through the points corresponding to the sum of events in each peak of the spectrum confirms
the conclusion as to the influence of multiple scattering on the shape of the energy spectrum.
We point out that not only multiple scattering, but also the geometry of the setup and the
thresholds in the channels of the spectrometer, in accordance with formula (10), have an ef-
fect in reducing the heights of the two peaks on the left. The change in the distance between
peaks indicates a change in the resolution over the depth of the specimen in accordance with
formula (7), but as the energy decreases the peaks broaden because of straggling and multiple
scattering, and this leads to practically the same resolution over the entire depth of the
specimen.

Results of Measurements. The atomic concentration of hydrogen can be calculated with
the aid of IVK-2, either directly during data acquisition or upon completion of the exposure,
from the relation

$$\frac{\partial c}{\partial X} = \frac{1}{n_{\mathrm{Me}}} \frac{M_s}{M} \frac{n_s}{N_s(K)} \frac{dN}{dK} \frac{dK}{dE} \frac{dE}{dX} (E), \tag{15}$$

where n_{Me} is the number of atoms per cm^2 of matrix material; M_r/M, ratio of monitor counts
in measurements with the standard target and the specimen; n_r, number of hydrogen atoms per
cm^2 in the reference polystyrene film:

$$N_s(K) = \exp\left\{\ln N_s(K_1) + \frac{K - K_1}{K_2 - K_1}[\ln N_s(K_2) - \ln N_s(K_1)]\right\} \tag{16}$$

standard function assuming exponential variation of the shape of the energy spectrum when the
specimen has a uniform hydrogen content; $N_s(K_1)$, $N_s(K_2)$, numbers of counts in the peaks from
polystyrene films with which an unhydrogenated wafer of the material under study is faced in
standard (calibration) measurements; dN/dK, instrumental spectrum obtained by processing the
two-dimensional field of events by summing them along the lines $K_X = K_Y$ in the region of local-

54

ization of scattering from hydrogen; $K = K_X + K_Y$, $K_2 - K_1$, interval in the instrumental spectrum occupied by hydrogen in the specimen under study; dE/dK, energy value of the analyzer channel as determined from the spectrum from the compound target (see Fig. 2); and dE/dX (E), stopping power of the material of the specimen for protons of energy E.

From the instrumental spectrum dN/dK we calculated the background of random coincidences, determined in each cell of the two-dimensional field from the "cross" of random coincidences from elastic scattering on the material of the specimen, which was always present in the two-dimensional spectra outside the region of localization of events corresponding to hydrogen.

The hydrogen content was determined for titanium, copper, and palladium. Before the measurements, the titanium wafer, 110 μm thick, was exposed on one side to the action of low-energy hydrogen ions in a glow-discharge plasma. After the measurements, it was found that the hydrogen content was approximately uniform over the entire depth of the titanium wafer, with a slight predominance of hydrogen in the surface layers. The details of these investigations were published earlier [3].

Seven copper specimens, rolled to a thickness ~100 μm, were studied. Since the specimens contained very little hydrogen, the problem consisted in determining the total hydrogen content. The dominant features in the spectrum investigated (Fig. 3) are surface peaks, apparently contaminated with oil from the vacuum system; accordingly, the hydrogen content of the specimen was determined from the total number of counts in the 15 channels between the peaks. The advantages of the method are clear, making it possible, as it does, to determine the true content of hydrogen in the specimen, eliminating extraneous contamination of the surface. The highest hydrogen content in the copper specimens was $(6.9 \pm 0.9) \cdot 10^{-4}$, while the lowest was $(0.4 \pm 0.1) \cdot 10^{-4}$ H atoms/Cu atom ($1.1 \cdot 10^{-5}$ and $0.06 \cdot 10^{-5}$ g H/g Cu).

Figure 4 gives a two-dimensional spectrum and its projection onto the axis of total energy, as obtained by measuring the hydrogen concentration in a palladium wafer 100 μm thick, one side of which was in contact with hydrogen at 100 kPa and room temperature for five days, while the other side was in contact with the vacuum space of the scattering chamber. Hydrogen did not appear on the entrance side, since the thickness of the palladium wafer exceeded t_{max}.

The total hydrogen content in the membrane was 0.05 ± 0.01 H atoms/Pd atom, which is substantially less than the equilibrium ratio of 0.7 H atom/Pd atom. Moreover, the exponential form of the spectrum in Fig. 4b, as mentioned above, indicates a uniform distribution of hydrogen over the depth of the membrane. The result obtained apparently confirms the paramount role of surface processes preceding the dissolution of hydrogen in palladium. A palladium surface not subjected to any special treatment impedes the processes of dissolution and outgassing of hydrogen, but if the surface is overcome, then the entire volume is quickly filled, as evidenced by the absence of a concentration gradient when the hydrogen-palladium system is not in equilibrium.

LITERATURE CITED

1. I. Ziegler et al., Nucl. Instrum. Methods, 149, 19 (1978).
2. K. P. Artemov et al., At. Energ., 34, No. 4, 265 (1973).
3. T. D. Radzhabov et al., At. Energ., 51, No. 1, 57 (1981).
4. M. I. GUseva et al., At. Energ., 51, No. 2, 126 (1981).
5. B. Cohen, C. Fink, and J. Degnan, Appl. Phys., 43, No. 1, 19 (1972).

APPARATUS FOR DETERMINING THE DIRECTION OF FLOW OF UNDERGROUND
WATER REVEALED BY A DRILLED WELL

I. G. Skovorodnikov   UDC 550.823.08

The determination of the direction of motion of underground water is an important problem
in hydrogeological and engineering-geological investigations. Electrical [1], thermal [2],
and radioisotopic [3, 4] methods are used for this purpose. Their common disadvantage is the
long duration of the observations and the necessity for having, as a rule, several drilled
wells, intersecting the flow being studied. Another known method is based on the use of dif-
ferent mechanical indicators of the flow direction. The advantage of this method is the short
duration of the measurements and the possibility of performing them in a single well, reveal-
ing the underground water. The disadvantages of mechanical devices lie in the discrete method
for measurements and in the low sensitivity to the flow velocity. For example, the sensitiv-
ity of one such device, the DAU-6 apparatus [5], is ~10 m/day.

Another device for determining the direction of flow, free of these disadvantages (see
Fig. 1), has been developed at the Department of Ore Geophysics at the Sverdlovsk Mining In-
stitute. The setup consists of a deflector, fixed to the lead screen, and a magnetic needle
with the radioactive isotope deposited on it. A ring-shaped cut is made in the screen with a
monotonically increasing width, while the needle is placed in the nonmagnetic hermetically
sealed chamber. The chamber is fixed rigidly to the screen and serves as a float, decreasing
the mass of the screen in the fluid. The rotational axes of the deflector and the needle co-
incide. The detector in the radiometer is enclosed by a cylindrical screen for protection
from scattered radiation from the source so that the radiometer detects only the direct radia-
tion passing straight through the cut in the screen. The device is placed along the axis of
the well with the help of three centering springs. In the well intersecting the flow of un-
derground water, the deflector is situated along the direction of motion of the underground
water, while the magnetic needle is oriented along the magnetic meridian. The angle between
the deflector and the needle, i.e., the magnetic azimuth of the flow, is determined from the
intensity of the exposure dose of radiation passing through the cut into the screen and de-
tected by the radiometer. At the same time, the increment to the width of the cut, depending
on the angular coordinate, is such that the intensity of the exposure dose of radiation pass-
ing through the cut varies linearly, as shown on the calibration curve (see Fig. 1c).

The device can be made in the form of an attachment to a series logging radiometer, which
will ensure widespread use in geological prospecting organizations. Calculations have been
performed for the setup, and such basic structural parameters as the type and intensity of
the radioactive source on the magnetic needle, thickness of the screen, dimensions of the cut
in the screen, dimensions of the nonmagnetic hermetically sealed chamber, area of the deflec-
tor, etc., have been justified for the setup. The sensitivity of the setup to the velocity of
flow has been calculated.

^{137}Cs was chosen as the source of γ radiation. This source has a long half-life (33
years) and gives a quite soft γ radiation (0.66 MeV) [6], which permits using a thin lead
screen. The intensity of the source must be such that the intensity of the exposure does
created by it is at least two orders of magnitude greater than the average radioactivity of
rocks. This permits neglecting the effect of the natural γ radiation on the results of meas-
urements.

The distance between the source and the detector of radioactivity is taken as 10 cm,
which corresponds to the optimal length of the collimating channel [7]. Taking into account
these conditions, it was found that the required quantity of radioactivity is 50 µCi (1 Ci =
$3.700 \cdot 10^{10}$ Bq). In calculating the thickness of the screen it was assumed that the screen
must attenuate the radiation from the source by not less than a factor of three. Based on
the known attenuation law for a narrow beam of γ radiation in matter [7] and the mass coeffi-
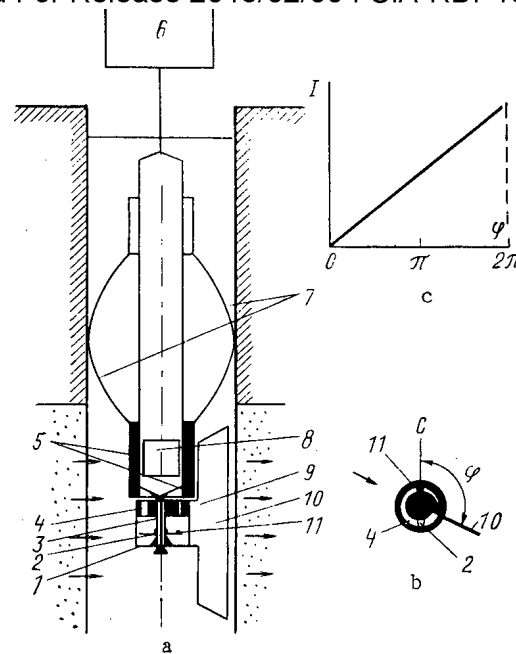
Fig. 1. Device for determining the direction of flow of under-
ground water: a) longitudinal section; b) transverse section of
the screen with cut; c) dependence of the intensity of the ex-
posure dose of radiation on the magnetic azimuth of the flow;
1) nonmagnetic hermetically sealed chamber; 2) magnetic needle;
3) axis of rotation of deflector and magnetic needle; 4) ring-
shaped cut; 5) cylindrical screen; 6) surface measuring block of
the radiometer; 7) centering springs; 8) radiometer detector; 9)
lead screen; 10) deflector; 11) radioactive isotope.
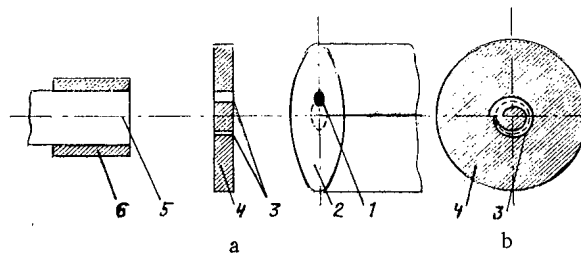
Fig. 2. Diagram of the experiment to check the functioning of
the setup: a) general view of the setup; b) screen with cut; 1)
reference source of γ radiation; 2) rotating drum; 3) ring-shaped
cut; 4) lead screen; 5) detector in the radiometer; 6) cylindrical
screen.

cient of absorption in lead, equal to 0.107 $g^{-1} \cdot cm^2$ for γ, it was calculated that the thick-
ness of the screen is 1 cm. The absorbing action of the fluid, filling the well, can be ne-
glected. The thickness of the side walls of the cylindrical screen, protecting the detector
in the radiometer from scattered radiation from the source, can be taken as 0.5-0.7 cm. The
equation for calculating the width of the ring-shaped cut in the screen according to the
fixed dimensions of the detector, thickness of the screen, and the distance between the
source, the screen, and the detector was given in [8]. For a NaI(Tl) crystal diameter, serv-
ing as the detector, equal to 25 mm, screen thickness of 1 cm, and distance to the source of
10 cm, the largest width of the cut is 6.25 mm.

The dimensions of the nonmagnetic hermetically sealed chamber were chosen so that the
mass of the entire mobile block of the setup, including the deflector, screen with the cut,
and hermetically sealed chamber with the magnetic needle, is completely compensated by the
pushing force acting on this block in the water-filled well. This permits greatly decreasing

57
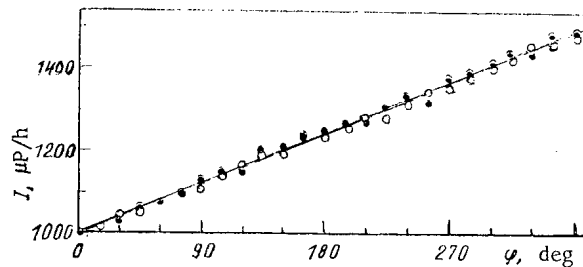
Fig. 3. Dependence of the intensity of the exposure dosage of radiation on the angle of rotation of the drum with clockwise (●) and counterclockwise (○) rotation.

the force of friction on the axis of the deflector and increasing the sensitivity of the set-up. The calculations show that with a deflector area of 60 cm^2 the setup can provide a sensitivity to flow velocity not higher than 1.0 m/day.

The apparatus was tested in order to estimate the possible accuracy of observations. In a laboratory experiment we used a scintillation SRP-68-01 radiometer [9] and a reference radium source of γ radiation with intensity 85 μCi (Fig. 2). The source was placed on the end face of a rotating drum. The flat lead screen with thickness 1 cm with the ring-shaped cut with monotonically varying width is placed at the center between the drum and the detector of the radiometer to which the cylindrical lead screen is attached for protection from scattered radiation. The average radius of the cut in the screen (6.25 mm) equals one-half the radius of the radiation detector and the distance of the center of the standard from the axis of rotation of the drum. The maximum width of the cut is also 6.25 mm, and the minimum width is zero. In order to construct the cut exactly, one half the increment of the width of the cut is marked along its radius every 10° on both sides of the center line of the cut:

$$\frac{\Delta r}{2} = \frac{6.25 \cdot 10}{360 \cdot 2} = 0.087 \text{ mm.}$$

The axis of rotation of the drum was superposed with the center of the ring-shaped cut and the longitudinal axis of the detector in the radiometer, after which the drum was rotated from the narrow part of the cut with stops every 10°. Then the measurements were repeated in the opposite direction of rotation of the drum.

When the drum was stopped, the indications of the recording instrument of the radiometer were recorded (Fig. 3). The transition from the count n in the scale divisions of the radiometer to the intensity of the exposure dose of radiation I was made using the calibration curve of the fifth subzone of the CRP-68-01 radiometer used in the experiment.

The absolute σ_q and relative ε_q mean-square errors in the measurements were calculated from the experimental results. It turned out that σ_q = 39 μP/h and εq = 3% (1 P = 2.58·10^{-4} Q/kg). The accuracy of the measurements was estimated by another method as well. The increment to the intensity of the exposure dose of radiation per unit angle of rotation of the drum was determined from the calibration curve (see Fig. 3):

$$C = \frac{\Delta I}{\Delta \varphi} = \frac{1480 - 1000}{360} = 1.3 \frac{\mu P/h}{\text{deg}}.$$

The value of a division on the radiometer scale on the fifth subzone of the measurements constitutes, according to the calibration curve, 50 μP/h. Since the measurement along the radiometer scale can be made with an accuracy of 1/4 divisions, i.e., 12.5 μP/h, the angle of rotation can be estimated from the indications of the radiometer with error ~10°. This accuracy is completely acceptable for practical purposes, since even for the best modern tiltmeters for wells the error in measuring the azimuth of the curvature of the well is not less than 4-5°.

Based on calculations and experiments, a design was developed for a device determining the direction of flow, in the form of a compact attachment to a logging Zond-1 radiometer with the well apparatus Almaz-3 with a diameter of 36 mm [9]. The length of the attachment is 420 mm. The minimum diameter of the well studied is 110 mm and the depths are up to 1000 m.

58

LITERATURE CITED

1. B. K. Matveev, Geophysical Methods for Studying the Motion of Underground Waters [in Russian], Gostoptekhizdat, Moscow (1963).
2. A. A. Ogil'vi, Electrometrical Methods and Thermometric Investigations in Studying Permeation from Reservoirs in Fractured Rock [in Russian], Moscow State Univ. (1970).
3. Radio-Isotopic Methods in Engineering Geology and Hydrogeology [in Russian], Atomizdat, Moscow (1977).
4. N. V. Churaev and N. I. Il'in, Radio-Indicator Methods for Investigation the Motion of Underground Waters [in Russian], Atomizdat, Moscow (1973).
5. É. Ya. Kipko, V. I. Kipko, V. I. Singalevskii, and V. I. Khamlai, Inventor's Certificate No. 311139, Byull. Izobret., No. 624, 145 (1971).
6. Well Nuclear Geophysics. Geophysicists Handbook [in Russian], Nedra, Moscow (1978).
7. V. A. Artsybashev, Nuclear Geophysical Prospecting [in Russian], Atomizdat, Moscow (1972).
8. I. G. Skovorodnikov, At. Energ., $\underline{41}$, No. 2, 146 (1976).
9. L. V. Gorbushina, Radiometry and Nuclear Geophysics [in Russian], Nedra, Moscow (1974).

EFFECT OF BORATION ON THE ACTIVITY INDUCED IN CONCRETES BY PROTON BOMBARDMENT

V. F. Kas'yanov, A. N. Kargin,
M. M. Komochkov, and M. F. Mitin

UDC 539.16.04:621.039-78

It was shown in [1-4] that the induced activity of concrete is lowered by a factor of 2-10 by the addition of 0.1-0.8 wt.% of boron. In experiments at the JINR synchrocyclotron we have determined the dependence of the induced activity of concretes on the boron content and have analyzed the economic effect of boration.

We irradiated borated concretes at characteristic locations in the accelerator room: at point 1 protons and high-energy neutrons predominated; at point 2 the flux of thermal and intermediate neutrons was about equal to the flux of fast and ultrafast neutrons [5]. The technological composition of the concretes is shown in Table 1.

Samples of borated and ordinary concretes 40 mm on an edge were irradiated at points 1 and 2 for 7.4 h and 180 days. The induced activity of the samples was measured with a 36 cm^3 Ge(Li) detector and an AI-8000 pulse-height analyzer. It was found that ^{24}Na made the main contribution to the γ activity of the concretes during the first four days after irradiation of the samples. The values of the activity of the concretes studied are shown in Table 2. The total error of the measurements did not exceed 30%.

At point 1, where high-energy neutrons and protons predominate, boration of the concretes is ineffective: within the limits of error of the measurements the values of the activity are practically the same for all the concretes. At point 2, where thermal and intermediate neutrons make a significant contribution to the activation of the concretes, the addition of 15-45 kg of boron per m^3 of granite concrete lowered the induced activity by a factor of 3-7, while the addition of 15-60 kg of boron per m^3 of lime concrete decreased the activity by a factor of 5-10. Boration of a large mass of concrete may double this effect, since the thermal neutron flux inside an ordinary concrete shield is twice as large as at the shield surface [1, 6].

We analyzed the economic effect of boration by comparing estimates of the minimum cost per m^2 of shield surface. In comparing different shields we used the following formula [7-9] to calculate the cost C_i in rubles:

$$C_i = K_i + E_n t_i (K_i' + K_i'') - \frac{1}{P_2 + E_n} u,$$

where K_i is the estimated cost of construction and assembly work, rubles; K_i', capital investment in the construction branch, rubles; K_i'', combined capital investment in the building design and detail branch, rubles; t_i, length of time the funds are used, yrs; E_n, normative

TABLE 1. Technological Composition of Concretes with a Density of 2300 kg/m^3

Kind of concrete	Input of materials, kg/m^3				
	Portland cement	sand	stone	water	boron carbide
Ordinary granite concrete	425	481	1219	175	—
Ordinary carbonate concrete	430	398	1228	244	—
Borated carbonate concrete (amt. boron, kg/m^3)					
15	427	396	1219	240	18
30	423	393	1210	237	37
45	421	391	1200	235	53
60	416	386	1192	235	71

TABLE 2. Activity of Concretes Observed Directly After Irradiation, mg-eq. Ra/g

Point of irradiation	Concrete	Amount of added boron, kg/m^3				
		0	15	30	45	60
1	Granite concrete	$7,7 \cdot 10^{-5}$	$6,6 \cdot 10^{-5}$	$6,9 \cdot 10^{-5}$	$7,0 \cdot 10^{-5}$	$6,8 \cdot 10^{-5}$
1	Lime concrete	$1,5 \cdot 10^{-5}$	$2,1 \cdot 10^{-5}$	$2,0 \cdot 10^{-5}$	$1,6 \cdot 10^{-5}$	$1,6 \cdot 10^{-5}$
2	Granite concrete	$4,3 \cdot 10^{-5}$	$1,5 \cdot 10^{-5}$	$1,1 \cdot 10^{-5}$	$6,3 \cdot 10^{-6}$	*
2	Lime concrete	$2,1 \cdot 10^{-5}$	$3,8 \cdot 10^{-6}$	$3,2 \cdot 10^{-6}$	$2,3 \cdot 10^{-6}$	$2,0 \cdot 10^{-6}$

*Not measured.
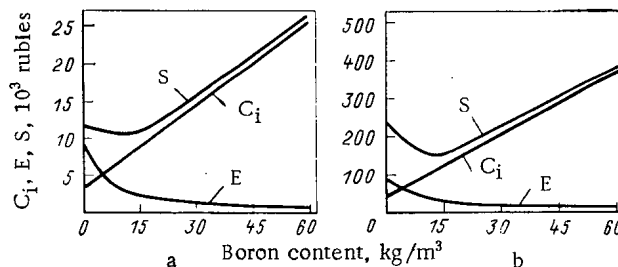
Fig. 1. Cost of constructing a borated concrete shield for:
a) the JINR 680 MeV synchrocyclotron; b) a tunnel-type proton accelerator; C_i is the cost of constructing a concrete shield; E is the economic effect of lowering the level of induced activity by borating the concrete; $S = C_i + E$ shows the optimum boration.

coefficient of effectiveness of the capital investments; P_2, deduction from capital expenditures for renewal of building materials; and u, annual cost of operating with the various shields, rubles per unit time.

It is planned to construct the biological shield of blocks of various sizes: 4 × 2 × 1, 2 × 2 × 1, 2 × 1 × 1, 1 × 1 × 1, and 1 × 1 × 0.5 m. The location is the first territorial region of the Moscow oblast. The aggregate for the concrete is limestone — a local building material. By comparing the estimated costs of materials for blocks of various standard sizes, it was found that per m^3 of concrete a biological shield can be constructed most cheaply of 4 × 2 × 1 m blocks.

The estimated costs of various 4 × 2 × 1 m concrete shields are listed below:

60

Ordinary carbonate concrete: 240.0
Borated carbonate concrete (amt. boron, kg/m^3): 0

       15.. 712.0
       30.. 1223.0
       45.. 1646.0
       60.. 2120.0

To determine the economic effect of lowering the induced activity of concretes by bora-tion, we estimated the cost of 1 rem as applied to working conditions at the JINR synchrocy-clotron. Taking account of additional wages, additional leave, special diet, pension, and medical service, we found the value 360 rubles/rem, which we used in constructing borated con-crete shields for the JINR 680 MeV synchrocyclotron and for a high-energy proton accelerator of the tunnel type with a staff of 100.

Figure 1 shows the calculated cost of constructing a shield of concrete blocks, the econ-omic effect of lowering the induced activity by borating the concrete, and the combined curve, whose minimum shows the optimum boration.

The following input data were assumed for the 680 MeV JINR synchrocyclotron shield, aver-age dose rate of occupational radiation, 2.5 rem/h, contribution of induced activity of con-crete walls to total dose rate in working areas of main experimental room, 10%; thickness of layer of borated concrete wall, 10 cm; height of borated wall, 5 m; perimeter of walls, 132 m.

For a tunnel-type proton accelerator the following input data were assumed: maximum ad-missible dose rate of occupational irradiation, 5 rem/h; contribution of induced activity of concrete walls to total dose rate in maintenance regions of the accelerator beam transport tunnel, 50%*; volume of concrete shield, 1000 m^3.

Figure 1 shows that the optimum boration of a concrete shield is 15 kg of boron per m^3 of concrete. The addition of more boron is inexpedient, since the added cost of such con-cretes is not justified by the small decrease in induced activity.

LITERATURE CITED

1. D. Nachtigall and S. Charalambus, CERN, 66-28 (1966).
2. W. Gilbert et al., UCRL 19368 (1969).
3. T. Armstrong and J. Barich, Nucl. Sci. Eng., 40 428 (1970); ORNL-TM-2768 (1969).
4. V. F. Kas'yanov et al., JINR 16-12/375, Dubna (1979).
5. V. F. Kas'yanov et al., P16-8899, Dubna (1975).
6. L. N. Zaitsev, M. M. Komochkov, and B. S. Sychev, Fundamentals of Accelerator Shielding [in Russian], Atomizdat, Moscow (1971).
7. Procedure for Determining the Economic Effectiveness of Using New Technology, Inventions, and Innovations in the National Economy [in Russian], Ékonomika, Moscow (1977).
8. Operating Instructions for Determining the Economic Effectiveness of Using New Technol-ogy, Inventions, and Innovations in the Building Materials Industry [in Russian], VNII-nauchnotekhnicheskoi Informatsii i Ekonomika Promyshlennosti Stroitel'nykh Materialov, Moscow (1978).
9. "Instructions for determining the economic effectiveness of using new technology, inven-tions, and innovations in construction," SN-509-78 NIIekonomika Stroitel'stva, Moscow (1979).
10. H. Patterson and R. Thomas, Accelerator Health Physics, Academic Press, New York-London (1973).

---

*From estimated contribution of induced activity of concrete walls to total dose rate in tun-nel of a 3 GeV proton accelerator [10].

RADIATION CREEP IN 09Kh16N15M3B STEEL AT STRESSES EXCEEDING THE ELASTIC

LIMIT

A. S. Kruglov, V. N. Bykov, and Yu. M. Pevchikh   UDC 621.039.531

Torsion in a thin-walled tube has been used [1] to examine the creep in 09Kh16N15M3B steel in the austenitized state in a reactor at stresses at or above the yield point. The tests were performed in the central loop channel of a BR-10 at neutron flux densities of $6 \cdot 10^{14}$ and $8 \cdot 10^{14}$ neutrons/cm$^2 \cdot$sec and E > 0; the rates K of defect formation were $3.1 \cdot 10^{-7}$ and $4.1 \cdot 10^{-7}$ displacements/atom$\cdot$sec. At the flux density of $6 \cdot 10^{14}$ neutrons/cm$^2 \cdot$sec, the measured temperature in response to the radiation heating was $(470 \pm 5)°C$, while at $8 \cdot 10^{14}$ neutrons/ cm$^2 \cdot$sec it was $(500 \pm 5)°C$. Initially, the specimen was irradiated in the unstressed state at 470°C, and after a damage dose of 5 displacements/atom had been attained the creep tests were begun. The stress was applied in steps covering the plastic-strain range. The nominal yield point $\sigma_{0.05}$ was defined during test at 470°C after the accumulation of about 7 displacements/atom and was 250-270 MPa.

The results show that step loading throughout the stress range was accompanied by nonstationary creep for 20-30 h, after which the deformation rate stabilized (Fig. 1). The logarithm of the creep rate $\dot{\varepsilon}$ and the stress intensity σ were calculated from measurements on the shear strain γ and the tangential stress τ with allowance for the plasticity relations: $\varepsilon = \gamma/\sqrt{3}$ and $\sigma = \tau\sqrt{3}$. Figure 1 shows that the creep within the reactor is dependent on the stress. At stresses below the yield point, the creep is of radiation type, and the rate is proportional to the stress [2]. In that case, the creep modulus defined as the deformation referred to unit stress and damaging dose was $6.9 \cdot 10^{-12}$ Pa^{-1} (displacements/atom)$^{-1}$ at 470°C or $7.8 \cdot 10^{-12}$ in the same units at 500°C. Above the yield point, the mode of deformation alters sharply and the dependence of $\dot{\varepsilon}$ on σ is close to exponential. At both temperatures, the following applies to a first approximation

$$\frac{\dot{\varepsilon} \, [h^{-1}]}{K[disp./atom \cdot h]} = A\,(T)\, e^{0.029\sigma[MPa]}, \tag{1}$$

where A(T) is a temperature-dependent factor. On raising the temperature from 470 to 500°C, the value of $\dot{\varepsilon}/K$ increases by about 170%, whereas at stresses less than the yield point the increase is only 13%. The temperature sensitivity of the creep thus changes considerably when the yield point is exceeded.

To determine the nature of the creep activation at stresses exceeding the yield point, we performed an experiment in the OK-70 channel of the BR-10, which was fitted with an electrical heater. A specimen of analogous steel was tested in creep in uniaxial tension at 290 and 365°C at stresses above $\sigma_{0.2}$. The σ dependence of $\dot{\varepsilon}$ in that case was exponential, and the exponent was 0.024 instead of 0.029 in (1). In one of the loading cycles, the reactor was shut down, while the temperature was maintained with the electric heater. Therefore, the stress level and the temperature were maintained, but there was no neutron flux, and the creep rate decreased by more than a factor of 100. In 200 h of tests, no deformation was observed, whereas deformation occurred within 10-15 h under irradiation. It has therefore been established that creep in this steel in this temperature range is radiation-stimulated when the yield point is exceeded. This agrees with published data [3], according to which the expected rate of thermal creep in a reactor is about $3 \cdot 10^{-7}$ h^{-1} at $\sigma = 365$ MPa and T = 500°C, while the measured value is $6.7 \cdot 10^{-5}$ h^{-1}.

Although the creep is initiated by irradiation, raising the temperature substantially accelerates the deformation. The factor A(T) in (1) can be put in the following form for 09Kh16N15M3B steel:

$$A\,(T) = Ce^{-Q/kT}, \tag{2}$$
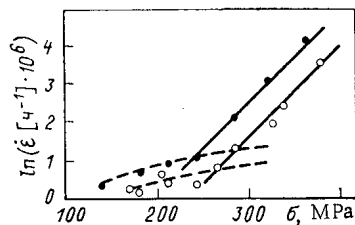
Fig. 1. Dependence of the rate of radiation-induced creep in 09Kh16N15M3B steel on stress: $\circ$, $\bullet$) from experiment at 470°C and K = 3.1• 10^{-7} displacements/atom•sec and 500°C and K = 4.1•10^{-7} displacements/atom•sec, respectively; ——) and ---) by calculation from (1) and (2) and from the creep modulus, respectively.

where C = 3.7•10^{-2}; k is Boltzmann's constant; and Q is activation energy, which in the present case is about 1.1-1.2 eV. This value of Q is about 1/3 of the self-diffusion activation energy and is closer to the activation energy characteristic of vacancy migration.

It has thus been found that the radiation creep in 09Kh16N15M3B steel is dependent on the stress and changes when the yield point is exceeded. There is simultaneously an increased effect from temperature on the creep rate, but thermal processes are not the primary cause of the deformation, at least in the stress and temperature ranges used.

LITERATURE CITED

1. A. S. Kruglov et al., Zavod. Lab., No. 1, 1048 (1980).
2. A. S. Kruglov et al., At. Energ., 51, No. 3, 189 (1981).
3. A. S. Kruglov et al., ibid., 50, No. 5, 342.

63

PLASTIC SCINTILLATORS FOR RECORDING FAST NEUTRONS

D. V. Viktorov, L. A. Gorbunov,
I. M. Rozman, A. M. Sirenko,
and V. M. Shoniya

Plastic scintillators containing neutron-active nuclides have been described in [1]. The characteristics of these scintillators are given by the activity of the nuclides, which is induced during the exposure in the neutron field under inspection. The activity is determined from the counting rate of β particles by extrapolation; the 4π geometry of counting makes it unnecessary to use many correction coefficients. It has been shown that good results are obtained when the extrapolation starts from the 90% level of the count of the total number of decays. This condition can be satisfied in practice when the limit energy of the β spectrum exceeds several hundred keV and when the scintillator is characterized by a sufficiently high light yield.

The goal of the present work was to test whether plastic scintillators with fluorine admixtures (SPS-A1) and iodine admixtures (SPS-A2) are suitable for detecting neutrons with an energy of about 15 MeV. For this purpose the scintillators were exposed in a known neutron field and the cross section of the (n, 2n) reactions at fluorine and iodine was determined from the induced activity. The values obtained were compared with published data.

Experiment. The plastic scintillators were prepared by thermal polymerization. n-Terphenyl and POPOP were used as luminescent additives. The fluorine and iodine concentrations were $m_F = 3.78 \cdot 10^{20}$ and $m_I = 3.83 \cdot 10^{19}$ atoms/cm^3, respectively. The plastic scintillators were employed in the form of cylinders (diameter 2R = 25 mm and height L = 10 mm) with a polished surface. The light yield of the plastic scintillators was 0.36 relative units according to All-Union State Standard 23077-78.

The scintillators were irradiated with neutrons generated in the ^{3}H(d, n)^{4}He reaction. Accelerated deuterons (180 kV) were incident under an angle of 55° with respect to the normal upon a tritium-scandium target with a diameter of 14 mm. The neutron yield Y could be determined from the count N_α of the accompanying α particles. A scintillation counter with a 0.3-mm-thick CsI(Tl) crystal was used; the counter was mounted at an angle of 90° relative to the direction of the deuteron beam [2]. The solid angle for recording α particles was $\Omega_\alpha = 4.18 \cdot 10^{-6}$ sr (counting rate $1.1 \cdot 10^4$ sec^{-1}). According to [3], we have

$$Y = 1.005 \frac{4\pi}{\Omega_\alpha} N_\alpha . \tag{1}$$

For the irradiation the plastic scintillators were put into a position coaxial with the target of the generator at a distance b = 91.3 mm (to the center of the plastic scintillator). The neutron energy was 14.7 ± 0.1 MeV. The irradiation had a duration ϑ = 60 min in the case of SPS-A1 and 4 h in the case of SPS-A2.

The activity of ^{18}F (half-life $T_{1/2}$ = 110 min) and of ^{126}I ($T_{1/2}$ = 13 days) was measured after 50 min and 1 day, respectively. For this purpose the plastic scintillators were placed on the cathode of an FÉU-110 photomultiplier (optical contact on liquid paraffin; teflon reflector) and the integral scintillation spectra were recorded. The unknown activity was determined from the half-life; the absolute count was determined by extrapolation to the zero discrimination level. The lowest discrimination level corresponded to the energies 28 and 35 keV for SPS-A1 and SPS-A2, respectively. The Compton spectrum was used to calibrate the spectrometer in terms of energy [4]. Two plastic scintillators with fluorine (seven series of irradiation measurements) and seven plastic scintillators with iodine were tested.

Results. In our experiment the absolute counting rate was numerically equal to the rate with which electrons were generated in the plastic scintillator by ^{18}F or ^{126}I decay, i.e.,

the absolute counting rate was equal to the product of the activity A of the radionuclide and the number ε of electrons in a single decay:

$$N_\beta = \varepsilon A_\beta.$$

The activity at the end of the irradiation is represented as

$$A(\vartheta) = \lambda \sigma m \frac{K_1 K_2}{4\pi} Y_{eff} \Omega_{PS}, \tag{2}$$

where λ is the decay constant of the radionuclide; σ, cross section of the radionuclide-generation reaction; K_1, K_2, coefficients accounting for the anisotropy of the neutron emission and its attenuation in the components of the target chamber of the generator; Y_{eff}, effective neutron yield of the generator; and Ω_{PS}, effective solid angle under which the plastic scintillator was irradiated. We therefore obtain

$$Y_{eff} = \int_0^\vartheta \frac{dY}{dt} \exp[-\lambda(\vartheta - t)]\, dt; \tag{3}$$

$$\Omega_{PS} = \frac{2\pi}{\Sigma_0 L} \int_0^\beta [1 - \exp(-\Sigma_0 Z)] \sin\omega\, d\omega, \tag{4}$$

where Σ_0 denotes the sum of the macroscopical cross sections of all reactions of a neutron with the nuclides of the plastic scintillator;

$$Z = \begin{cases} \dfrac{L}{\cos\omega} & \text{for } 0 \leqslant \omega \leqslant \alpha = \operatorname{arctg} \dfrac{R}{B + L/2}; \\[2ex] \dfrac{R}{\sin\omega} - \dfrac{b - L/2}{\cos\omega} & \text{for } \alpha \leqslant \omega \leqslant \beta = \operatorname{arctg} \dfrac{R}{b - L/2}. \end{cases}$$

In our "geometry"

$$\frac{1}{4\pi} \Omega_{PS} = 0.00444 \tag{5}$$

(according to (5), $\Sigma_0 \approx 0.10$ cm^{-1}, and the σ_m values to be expected do not exceed $1 \cdot 10^{-4}$ cm^{-1}), $K_1 = 1.0461$ [6], and $K_2 = 0.96$. The Y_{eff} value is obtained by recording the increase in the α count during irradiation:

$$Y_{eff} = C_\alpha N_{\alpha,\,eff} = C_\alpha \int_0^t \frac{dN_\alpha}{dt} \exp[-\lambda(\vartheta - t)]\, dt, \tag{6}$$

where $C_\alpha = 2.98 \cdot 10^6$ according to Eq. (1).

Thus, we obtain for the determination of σ,

$$\sigma = \frac{7.56 \cdot 10^{-5}}{\lambda \varepsilon m} \frac{N_\beta}{N_{\alpha,\,eff}}. \tag{7}$$

The results are listed in Table 1. The ε values were taken from the table of [7]. The contribution (0.068) from the internal conversion electrons was taken into account in the case of ^{126}I. The cross section figures coincide with the data of [8].

However, it should be noted that the mean-square deviation σ does not include a possible systematic error in the Ω_α value. Therefore, an additional comparison was made with copper activation in the $^{63}Cu(n, 2n)^{62}Cu$ reaction, for which a cross section of $(558 \pm 11) \cdot 10^{-27}$ cm^2 was assumed [8]. Copper disks (diameter 9 mm, thickness 1 mm) were irradiated at a distance of 53.5 mm from the target. The activity of ^{62}Cu was determined by counting the photons of the annihilation radiation with the aid of a spectrometer containing a 40×40 mm NaI(Tl) crystal. The efficiency of the spectrometer was experimentally determined with the aid of a calibrated ^{22}Na source from an OSGI equipment and with calculations according to [9]. The values $1.81 \cdot 10^{-3}$ and $1.83 \cdot 10^{-3}$, respectively, were obtained.

By comparing the results in the determination of the ^{62}Cu activity (five samples) with Eq. (2), the value $K_1 K_2 C_\alpha = (2.95 \pm 0.12) \cdot 10^6$ was obtained, or, in place of Eq. (7), we have

65

TABLE 1. Experimental Results of the Determination of the Reaction Cross Section

Activation reaction	λ, sec^{-1}	ε	$\dfrac{N_\beta}{N_{\alpha,\,\text{eff}}}$, sec^{-1}	σ, 10^{-27} cm^2		
				according to Eq. (7)	according to Eq. [8]	according to Eq. (8)
$^{19}\text{F}\,(n,\,2n)\,^{18}\text{F}$	$1{,}052 \cdot 10^{-4}$	0,97	$(2{,}57 \pm 0{,}10) \cdot 10^{-5}$	$50{,}4 \pm 2{,}0$	$54{,}1 \pm 5{,}4$	$50{,}8 \pm 2{,}7$
$^{127}\text{I}\,(n,\,2n)\,^{126}\text{I}$	$6{,}16 \cdot 10^{-7}$	0,54	$(2{,}72 \pm 0{,}06) \cdot 10^{-7}$	1614 ± 36	1655 ± 55	1629 ± 70

$$\sigma = \frac{7{,}63 \pm 0{,}28}{\lambda \varepsilon m}\, 10^{-5}\, \frac{N_\beta}{N_{\alpha,\,\text{eff}}}. \tag{8}$$

The σ values are listed in the table.

CONCLUSIONS

The results of the present work confirm the usefulness of the extrapolation of activity measurements on ^{18}F and ^{126}I nuclei formed inside a plastic scintillator irradiated with fast neutrons. Accordingly, plastic scintillators with additions of fluorine or iodine can be successfully used for measuring a neutron flux F. In a stationary field of monoenergetic neutrons or in the case of linear plastic scintillator dimensions significantly smaller than the free path length of a neutron (see Eq. (2)), we have

$$F = \frac{\vartheta A\,(\vartheta)}{\sigma M\,[1 - \exp(-\lambda\vartheta)]}, \tag{9}$$

where M denotes the number of fluorine or iodine nuclides in the plastic scintillator.

Obviously, when the exposure is not too long, plastic scintillators with fluorine are to be preferred. Let us note that the high energy threshold (above 12 MeV) of the $^{19}\text{F}(n, 2n)^{18}\text{F}$ reaction makes it possible to use the ^{18}F activity to determine the number of primary interactions of 14–15 MeV neutrons with the nuclides of plastic scintillators of even larger dimensions. This is important for dosimetric applications.

The authors thank K. A. Kovyrzin and E. N. Bokeriya for their help in preparing the scintillators.

LITERATURE CITED

1. E. E. Baroni et al., At. Energ., 31, No. 5, 508 (1971).
2. D. V. Viktorov, I. M. Rozman, and A. M. Shcherbakov, At. Energ., 31, No. 1, 49 (1971).
3. T. Fewell, Nucl. Instrum. Methods, 61, No. 1, 61 (1968).
4. D. V. Viktorov, I. M. Rozman, and T. S. Tsulaya, Prib. Tekh. Eksp., No. 3, 266 (1972).
5. A. Del Guerra, Nucl. Instrum. Methods, 135, No. 2, 337 (1976).
6. The Physics of Fast Neutrons [in Russian], Vol. 1, Atomizdat, Moscow (1963).
7. Table of Isotopes, 7th ed., Wiley, New York (1978).
8. Z. Böldy and J. Csikai, Atomic Energy Reviews [in Russian], Vol. 11, No. 1, 153 (1973).
9. N. A. Vartanov and P. S. Samoilov, Techniques in the Practice of Gamma Scintillation Spectrometry [in Russian], Atomizdat, Moscow (1964).

INCREASED EFFICIENCY OF UTILIZATION OF THE NEUTRON FLUX IN NEUTRON-ACTIVATED

SETUP WITH CENTRALIZED POSITIONING OF THE CALIFORNIUM SOURCE

B. S. Vakhtin and G. A. Kuznetsov   UDC 543.53

Ampule neutron sources based on ^{252}Cf are currently widely used in different areas of science and industry: in physics, geology, mining, medicine, metallurgy, etc. [1]. However, the number of elements identified by the neutron activation method using these sources is limited mainly to those elements that enter into the nuclear reaction (n, γ) for thermal neutrons (aluminum, sodium, manganese, and others). Analysis of elements entering into reactions (n, p) and (n, α) with fast neutrons is complicated or impossible, since for many elements the thresholds for these reactions are high (e.g., 3.9 MeV for silicon, 4.9 MeV for iron, etc.), while the average neutron energy of californium sources is $\bar{E}_n = 2.34$ MeV. For this reason, in order to realize the nuclear reactions (n, p) and (n, α) in neutron activation analysis, polonium–beryllium or plutonium–beryllium sources, which have a harder neutron spectrum ($\bar{E}_n = 4.0–4.5$ MeV).

In most designs of neutron activation setups, the neutron sources are placed outside the specimen: with irradiation by thermal neutrons in the moderator, or with irradiation by fast neutrons in the cavity behind the cadmium screen. Even in the most favorable case, when with irradiation by fast neutrons the source is up against the specimen, not more than one half of its radiation is used: part of the neutrons does not participate in the activation of the specimen and leaves the zone of activation.

One method for increasing the utilization efficiency of the neutron flux is the central geometry, i.e., placement of the source inside the specimen. An analogous problem was solved in developing the neutron resonance setup [2].

In order to clarify the possibility of the application of californium sources in neutron activation analysis based on fast neutrons, an experiment was performed, which involved 2–3 fold successive irradiation of specimens by fast and thermal neutrons from plutonium–beryllium and californium sources in different geometries, detection of their induced activation in the region of the photopeaks chosen for analysis, and the comparison of the data obtained. The specimens consisted of quartz glass powder (100% silica) and a mixture of chemically pure aluminum oxide and calcium carbonate (10% alumina). These elements were chosen based on the following factors: The threshold of the nuclear reaction (n, p) on silicon equals 3.9 MeV, i.e., higher than $\bar{E}_n$ of the source with the soft spectrum (californium), and is approximately equal to $\bar{E}_n$ of the source with the hard spectrum (plutonium–beryllium). The ^{28}Al formed has a convenient half-life ($T_{1/2} = 2.3$ min) and emits 1.78 MeV γ rays, which can be detected with high efficiency by a sodium–iodide scintillation detector. The utilization efficiency for a californium source for identifying aluminum, entering into the reaction (n, γ) on thermal neutrons with the formation of the same ^{28}Al, was estimated in the same experiment.

The irradiation block of the neutron activation setup with the plutonium–beryllium sources [3] is a metallic vessel with a 70×70 cm cross section and height 50 cm, filled with water (Fig. 1). An assembly of two blocks, situated coaxially one on top of another, is placed in the center of the vessel: the upper block, consisting entirely of Plexiglas, is the thermal neutron block; the lower block is hollow and is the fast neutron block. An axial cylindrical opening with diameter 70 mm serves as a working channel, in which a holder with the sample is placed for irradiation. The specimen is fixed at a height relative to the neutron sources situated at a distance of 1.5 cm from the working channel in a position for irradiation by thermal neutrons with the help of a Plexiglas insert. In the fast-neutron irradiation position of the specimen the insert is removed, and the neutron sources are repositioned into the lower position, up against the cadmium screen.
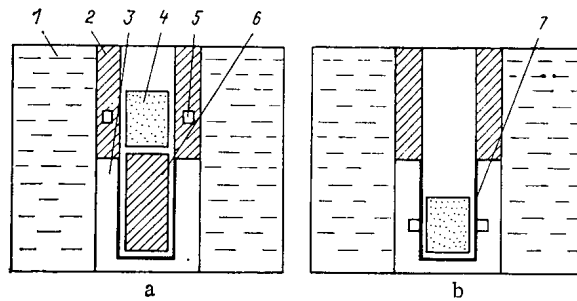
67

Fig. 1. Irradiation block of neutron activation setup with externally positioned neutron sources in the position for irradiation by thermal (a) and fast (b) neutrons: 1) water; 2, 3) block of thermal and fast neutrons; 4) holder with specimen; 5) neutron source; 6) insert; 7) cadmium screen.

TABLE 1. Counts for Specimens Analyzed for Silicon and Aluminum Using Different Neutron Sources

Source	Quantity	Yield, 10^6 neutrons/sec	Position of sources relative to specimen	Specimen studied	Count per 1 g %, counts*	
					f.n.	t.n.
Pluto-nium–beryllium	2	8,6	Outside	SiO_2—100%	0,251	0,160
				Al_2O_3—10%	0,025	1,023
				SiO_2—100%	0,050	0,048
				Al_2O_3—10%	0,030	1,88
Califor-nium	2	6,0	Outside	SiO_2—100%	0,206	—
	1	3,0	Inside holder with specimen in cadmium screen	Al_2O_3—10%	0,050	—
	1	3,0	Inside holder with specimen in moderator	SiO_2—100%	—	0,206
				Al_2O_3—10%	—	1,76

*After irradiation by fast (f.n.) and thermal (t.n.) neutrons.

The measuring apparatus consists of a scintillation detector (single crystal of sodium iodide, activated by thallium, with a diameter of 160 and height of 200 mm with a pit having a diameter of 70 mm, and a FÉU-49 photomultiplier) and a recording apparatus (an AI-128-2 pulse height analyzer and a BZ-15M digital printing setup. To decrease the background the detector is placed in a lead housing with a wall thickness of 10 cm.

The irradiation time in all the experiments was 6 min, the interruption time was 20 sec, and the measurement time was 5.4 min (according to a AI-128-2 timer). The interruption between irradiations of the specimens by the fast and thermal neutrons was not less than 1 h.

The summed values of the number of pulses recorded in the region of the photopeak of ^{28}Al, referred to the output of the neutron source 10^6 neutrons/sec, mass 1 g, and 1% content of the oxide of the element (for the time of 5.4 min), were used as the characteristics of activation of silicon and aluminum under different conditions.

Table 1 presents the counting rates for 1 g % silica and alumina with fast- and thermal-neutron irradiation of specimens from plutonium–beryllium and californium sources situated outside the specimen. Thus, from the plutonium–beryllium sources the counting rate for silica according to fast neutrons is 0.251 counts; for alumina according to the thermal neutrons the counting rate is 1.023 counts. In an analogous geometry, for californium sources the count for silicon decreased by a factor of five (to 0.05 counts), and for aluminum it increased to 1.88 counts.
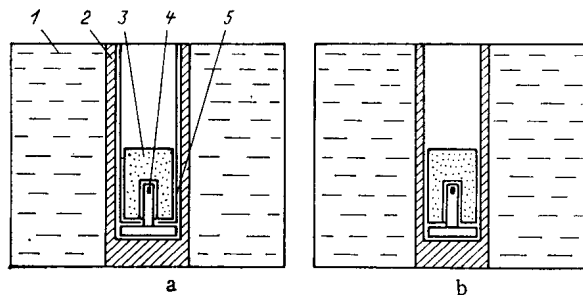
68

Fig. 2. Irradiation block of neutron-activation setup with central positioning of the source at the position of irradiation by fast (a) and thermal (b) neutrons: 1) water; 2) Plexiglas; 3) holder with specimen; 4) neutron source; 5) cadmium screen.

The next experiment was performed with a californium source in the central geometry. The source of neutrons in this irradiation block is located in the holder, placed at the bottom of the working channel. The holder of the source with diameter 12 and height 50 mm is attached to the foundation, which has a diameter equal to the diameter of the channel (Fig. 2). The holders for the specimens are the same as in the preceding setup. Vertical channels are extended to one half the height of the holder at the bottom. When the holder is placed in the working channel for irradiation, it is placed with its channel on the holder with the neutron source, and the source turns out to be inside the specimen. The fast neutron flux in this case is used almost in a 4π geometry.

The results obtained with irradiation of standard silicon and aluminum specimens in the central geometry are also presented in Table 1. As can be seen from the table, the count from activation of silicon by fast neutrons from a californium source was equal to 0.206 counts, i.e., it is four times greater than from two of the same sources positioned outside the specimen and comparable to the count with activation by neutrons from two plutonium–beryllium sources with approximately the same yield. The activation of aluminum by thermal neutrons from a californium source in this geometry is almost two times higher than from plutonium–beryllium sources.

Thus, for simultaneous neutron activation determination of silicon and aluminum, californium sources with output of not more than 10^7 neutrons/sec can be used. In this case, the activation of aluminum by thermal neutrons is increased almost by a factor of two compared to the effect from the plutonium–beryllium sources with the same yield. For the silicon analysis, the loss in activation is small (20–25 rel. %) and can be compensated by the use of a source with a somewhat higher yield.

LITERATURE CITED

1. I. K. Shvetsov, At. Energ., 41, No. 3, 223 (1976).
2. B. S. Vakhtin, and E. M. Filippov, ibid., 31, No. 2, 161 (1971).
3. B. S. Vakhtin, V. S. Ivanov, and G. A. Kuznetsov, ibid., 43, No. 4, 298 (1977).

ADDITIONAL RADIATION FACTORS IN HIGH-CURRENT ELECTRON ACCELERATORS

L. F. Belovodskii, V. D. Egerev,
N. I. Zavada, P. L. Komarov,
N. A. Mishin, A. V. Pilipenko,
and M. D. Volodin

The direct discharge of a pulsed high-voltage generator into a vacuum diode is preferably used in high-current electron accelerators of the first generation. One of the accelerators of this type is the MIG-5000 [1], which at a distance of one meter from the target renders a bremsstrahlung dose rate of up to $0.28 \cdot 10^8$ C/(kg·sec) at a pulse duration $\tau_i = 10^{-6}$ sec and a current of about 10^4 A. The pulsed operation of the vacuum diode and its mounting behind a radiation-protection shield reduce the radiation in industrial installations to the admissible levels. Only the activity induced by γ-n reactions was considered as an additional source of radiation hazard. However, since the quantum energy is low ($E_\gamma^{max} = 2.5$ MeV), this factor can be disregarded.

A double pulse-shaping line is used between the pulsed voltage generator and the vacuum diode in accelerators of the second generation. This principle implies a reduction of the pulse length at practically unchanged integral characteristics so that the bremsstrahlung dose rate can be increased. The scheme has been employed in the modernization of the MIG-5000 (ORION-1) accelerator, wherein at a current of 100–400 kA and $\tau_i = 10^{-7}$ sec the dose rate increased by a factor of 10 [2]. The much higher current in the vacuum diode, the phase before the pulse, pinching of the current channel, and self-isolation of the electron beam can cause changes in the radiation conditions. Indeed, when an accelerator operated with a maximum prepulse [3] is switched on, neutrons are generated and induced activity appears in the components of the vacuum diode [4]. These phenomena have not been observed in the accelerators of the first generation. When the energy (W_{st}) stored in the double pulse-shaping line is increased, the neutron yield increases too and reaches about 10^9 neutrons/pulse at $W_{st} = 60$ kJ.

The highest intensity of the induced activity is observed at the cathode. The half-life period ($T_{1/2} \approx 10$ min) and the energy spectrum ($E_\gamma = 0.511$ MeV) allow the determination of the type of the radionuclide (^{13}N). This indicates that ^{12}C(d, n)^{13}N, ^{12}C(p, γ)^{13}N, ^{13}C(p, n)^{13}N reactions dominate. In addition to ^{13}N there appear the products of (p, n) and (d, n) reactions at the elements present in the cathode composition [4]. In the large majority of cases, these elements are β^+-emitters.

The composition of the ion beam, the source of which is the anode plasma, is given by a $\sim 10^{-5}$-cm-thick organic coating and the hydrogen absorbed by the anode material [5]. Protons dominate in such an ion source. The deuteron concentration (0.015%) in the beam is given by the abundance of deuterium in natural hydrogen. Abnormally high neutron yields and high induced activity are associated with up to 10–15% of particles with an energy $qU_{vd} \leqslant E_i \leqslant 12$ MeV in the ion beam, where q denotes the charge of an ion and U_{vd} denotes the voltage generated by the double pulse-shaping line at the vacuum diode [4]. In this case the (p, n) reaction is possible in addition to the (d, n) reaction, because $E_i^{\alpha\ nom} = 3.12$ MeV (^{13}C).

The problems of the energy spectrum and composition of the ion beam and of the anisotropy, spectrum, and total yield of the neutrons have been described in [4]. The authors have also treated the distribution of the induced activity over the elements of the vacuum-diode assembly.

The induced activity makes it necessary to investigate additional factors of radiation hazard. It should be noted that the anode plasma in the vacuum diode can have both the natural composition or an enrichment by deuterons. In the first mode of operation, when the energy stored by the ORION-1 equipment is close to the nominal value, the yield can reach $2 \cdot 10^{10}$ neutrons/pulse. A neutron yield was not observed in similar situations in equipment of the first generation. In the second mode of operation, 10^{11} neutrons/pulse were obtained

with a stored energy W_{st} ~ 40 kJ, whereas the corresponding figure was ~10 neutrons/pulse in the first-generation equipment [4]. Since the reaction products are the same in both modes of operation, the considerations concerning radiation factors will be based on measurement results for a yield of $2 \cdot 10^{10}$ neutrons/pulse in the case of deuteron-enriched plasma and with a stored energy W_{st} = 40 kJ ($\sim 0.1 W_{nom}$).

Additional factors of radiation hazard originate from the activity induced in the elements of the vacuum-diode assembly, γ radiation arising from the slowing down and the annihilation of the positrons emitted by the reaction products, and radioactive gas. In order to investigate the induced activity, polyethylene and Lavsan foils, as well as nickel and copper foils, were applied to the surfaces of the cathode. The energy spectra of the particles emitted and the decay rate of the reaction products were determined. It was established in the measurements that an activation is observed on both the cathode and the inner surface of the discharge chamber. The activation density has its maximum in the area of the main discharge where the average activity reaches $1.5 \cdot 10^7$ Bq ($0.4 \cdot 10^{-3}$ Ci) at a cathode area of 75 cm^2. The activation products applied by evaporation of the cathode target to the surface of the discharge chamber reach a maximum activity of $(1-3) \cdot 10^4$ Bq/cm^2.

A sealed USIT-1-2V measuring chamber with a IUM-2-1eM ("Aktiniya") rate meter were used to measure the resulting gas products of the activation process in the vacuum-diode volume (V = 1.5 m^3). The chamber was connected to the vacuum diode and, along with it, evacuated to the working pressure of $6.6 \cdot 10^{-4}$ Pa ($5 \cdot 10^{-5}$ mm Hg). After a discharge, the pressure in the diode increases to 1.33–13.3 Pa as a consequence of gas liberation from the target. The products obtained migrate into the measuring chamber with the smaller volume. At an average concentration of the ^{13}N gas with Q = $7.4 \cdot 10^2$ Bq/liter, measured after pressure leveling, the total activity of the gas phase was $1.1 \cdot 10^6$ Bq.

The β^+ activity causes annihilation quanta. Therefore, after a pulse, the inner surface and the electrodes of the vacuum diode are γ radiation sources with E_γ = 0.511 MeV. At an overall concentration of $2 \cdot 10^{10}$ nuclei formed, the flux of the annihilation quanta at a distance of one meter from the target can reach $3.3 \cdot 10^5$ cm^{-2}, which corresponds to a dose of $0.23 \cdot 10^{-7}$ Ci/kg after each pulse.

The relative contribution of the various radiation factors to the irradiation of the personnel of the installation was assessed on the basis of experimental data (see Table 1). Obviously, the irradiation of the hand wrists in a disassembly of the vacuum diode is the main irradiation factor. On the first glance, the doses observed after each pulse are low, but if the mean annual operation of an installation of this type is about 1000 pulses, the radiation dose will significantly exceed the tolerable value. When the ORION-1 accelerator is operated with the nominal energy supply and the conditions of the operation with ions are optimized the above values will be increased by 1-2 orders of magnitude. This implies an even more significant deterioration of the radiation conditions.

Reducing the time of contact with the targets and of their disassembly after each exposure (when a considerable part of the radioactive material decays) is one of the fundamental ways of reducing the irradiation dose. However, this approach is in some cases inconsistent with the requirements of the experiment. In order to reduce the dose generated by annihilation radiation, additional shielding of the vacuum diode should be introduced. In our

TABLE 1. Contribution of the Ions to the Irradiation of the Personnel in a High-Current Electron Accelerator

Type of interaction	Interaction factors	Irradiation dose*		Interaction conditions
		after one pulse	per year	
Induced β^+ activity of the construction materials	Irradiation of hand wrists	$3 \cdot 10^{-2}$	30	Disassembly of the vacuum diode and contact with the inner surfaces during 1-2 min after a pulse
Gaseous activation products	Internal irradiation	$1 \cdot 10^{-4}$	0,1	Leakage of the vacuum diode and emanation of gas into premises with a volume of 60 m^3
Annihilation radiation	External irradiation	$1,6 \cdot 10^{-5}$	$1,6 \cdot 10^{-2}$	Servicing of the vacuum diode during 20 min after a pulse

*Considered in relation to the values acceptable according to radiation safety standards.

71

opinion, it is very problematic to reduce the ion currents with the available pumping tech-
nology, because experience has shown that in the case of small intervals between pulses, the
neutron yield and the activity decrease gradually, but vanish completely when the interval
is increased to 20-30 min.

Thus, in second-generation accelerators with operating currents close to the critical
value, there can appear substantial changes in the radiation conditions, and it is therefore
necessary to consider additional radiation factors in the irradiation of the personnel and to
take the corresponding organizational measures.

LITERATURE CITED

1. K. F. Zelenskii et al., Prib. Tekh. Eksp., 4, 175 (1969).
2. K. F. Zelenskii et al., Pis'ma Zh. Tekh. Fiz., 5, No. 4, 239 (1979).
3. N. V. Belkin et al., Pis'ma Zh. Tekh. Fiz., 5, No. 3, 169 (1979).
4. N. I. Zavada et al., At. Energ., 51, No. 1, 19 (1981).
5. I. N. Slivkov et al., Electrical Breakdown and Discharge in Vacuum [in Russian], Atomiz-
    dat, Moscow (1966).

HELIUM BLISTERING OF NICKEL WITH A TEMPERATURE GRADIENT IN THE SURFACE LAYER

M. I. Guseva, S. M. Ivanov, Yu. V. Martynenko,   UDC 621.039.531
and A. I. Ryazanov

The amount of heat reaching the first wall in a fusion reactor may vary from 10 to 100
W/cm^2 in accordance with the type of reactor (hybrid or pure) and the performance of the di-
verter. Then the temperature gradient in the wall material, which may be stainless steel or
an aluminum alloy, may be ~20°C/cm and ~100°C/cm, correspondingly.

In this connection we have examined the radiation blistering of nickel with a temperature
gradient in the surface layer. The surface was exposed to He^+ ions of energy 40 keV and was
also exposed to an electron beam of power about 100 W/cm^2 (electron energy E = 0.8 keV). For
comparison, experiments were performed with He^+ alone (E = 40 keV) with a nickel target heated
by thermal radiation, which provided an isotropic temperature distribution through the thick-
ness. The measurements were made with a target surface temperature in the range 400-850°C.
The angles of incidence of the He^+ and electrons on the target were 12°. In most of the ex-
periments, the doses were the same at 10^{18} ions/cm^2 with a current density of $1.8 \cdot 10^{14}$ ions/
cm$^2 \cdot$sec. The irradiation was performed in an ILU-3 accelerator [1]. The nickel specimens
were rods of diameter 0.8 cm and length 1.5 cm and had been annealed at 850°C for 1 h before
irradiation and then chemically polished. The target temperature and the temperature gradient
were checked by means of two thermocouples at distances of 1 and 11 mm from the irradiated
end surface.

A scanning electron microscope was used to examine the surface topography after helium
implantation. Figures 1 and 2 show photomicrographs of nickel irradiated with helium ions un-
der two conditions at different temperatures. In both cases there is the same effect on the
topography as the temperature increases: flaking—high-temperature blistering—formation of
pores, which agrees with the results of [2]. On the other hand, both irradiation conditions
lead to characteristic features in the structure. With an isotropic temperature distribution,
a porous surface is formed at 700°C with a dose of 10^{18} ion/cm^2 (pore diameter 0.15-0.5 µm,
density about 10^9 cm^{-2}), while on irradiation at 600°C one gets dome-shaped blisters of regu-
lar form of diameter from 0.5 to 2 µm, while a porous structure develops over the surface,
including the tops of the blisters, when the dose is increased to $3 \cdot 10^{18}$ ion/cm^2. In the case
of a temperature gradient at the surface ΔT = 70 deg/cm with a dose of 10^{18} ion/cm^2 and temp-
erature of 680°C, one gets high-temperature blistering (d = 0.5-2 µm), and an increase in dose
to $3 \cdot 10^{18}$ ion/cm^2 raises the blister density (the character of the surface damage does not al-
ter). Raising the irradiation temperature to 810°C produces surface pores at 10^{18} ion/cm^2.

to formation of a porous surface to higher temperatures.

Also, the transition from blistering to a porous surface is dependent not only on temperature, but also on dose. In a certain temperature range at low doses (10^{18} ion/cm^2) there is blistering, while a porous surface arises at higher doses ($3 \cdot 10^{18}$ ion/cm^2).

The effects of temperature on the erosion by helium ions have been explained [2] in terms of expansion of the defect and interstitial-ion distribution curve arising from the diffusion of point defects and helium atoms. The increase in the thickness of the bubbles with high helium pressures reduces the region of elastic deformation at the top of a blister. This reduces the rigidity N of the blister cover and a transition occurs from flaking to the formation of blisters, while a further increase in temperature reduces the size of the blisters in accordance with [3]

$$d \sim \sqrt{N/\sigma},$$

(1)

where $\sigma = \int_0^t \sigma_{rr}(x)\, dx$ is the integral stress in the top of a blister; $\sigma_{rr}(x)$, stress at depth x; and t, thickness of the top of a blister. At high temperatures, the distribution $\sigma(x)$ becomes of step type, and at depth t, where $\sigma(x)$ attains its maximum, one gets pores instead of cracks, which extend to the surface. The distributions of the bubbles and of $\sigma(x)$ may be in fluenced by the migration of the bubbles in response to stress and temperature gradients along with the effects from diffusion of the point defects and helium atoms.

An expression has been derived [4] for the speed of a vacancy pore of radius R in the presence of temperature and stress gradients, where allowance was made for the motion of adsorbed atoms and vacancies over the surface of a pore.

If we consider the motion of bubbles with high gas pressures ($p \approx 0.1E$, where E is Young's modulus) [5], we have to consider some specific factors. The energies of formation for adsorbed atoms and vacancies ε^*_A and ε^*_V at the surface of a bubble differ from the corresponding quantities for the case of an empty pore ε^*_{oA} and ε^*_{oV}, since energy ωp is consumed or released when an adsorbed atom or a vacancy is produced in a gas bubble (ω is the volume of one vacancy or adsorbed atom). Then $\varepsilon^*_A = \varepsilon^*_{oA} + \omega p$ and $\varepsilon^*_V = \varepsilon^*_{oV} - \omega p$, i.e., the adsorbed-atom concentration in the bubbles decreases, while the vacancy concentration increases, and one can assume that the bubbles move, in the main, by vacancy migration over the surface. Allowance must be made for the effects of the temperature gradient on the vacancy concentration at the surface and also on the vacancy diffusion coefficient D_V [4].

One also has to consider the change in free energy of the bubble $\Delta\mathscr{F} = \frac{\partial\mathscr{F}}{\partial T}\nabla T\delta R$ when it moves a distance δR in a variable temperature field. The free energy $\mathscr{F}$ of a bubble is [5] the free energy of the gas and that of the deformed crystal around the bubble having a high gas pressure. As the vacancy displacement δr is related to δR by $\delta r = (-1/n)\delta R$, where n is the number of vacancies in the bubble, while the number of helium atoms in the bubble is m = qn (where q may be 3-4 [5] or even 6 [6]), the displacement of a vacancy over the surface of a bubble is accompanied by consumption of the energy $\Delta u = \frac{1}{n}\frac{\partial\mathscr{F}}{\partial T}\nabla T\delta r = qs\nabla T\delta r$, where s is the entropy per helium atom in a bubble. The results of [4] and the above arguments give us the bubble speed as

$$V = -\frac{2a}{RT}\nabla T D_V C_V \left\{ +\frac{\varepsilon^*_V - Q_V}{T} + qs \right\},$$

(2)

where a is the linear size of a vacancy; R, bubble radius; C_V, vacancy concentration at the surface; and Q_V, heat of vacancy transfer [7]. It follows from (2) that for $Q_V < \varepsilon^*_V + qsT$ the bubbles migrate to the region of lower temperature, i.e., into the specimen. If this situation occurs, the profile of the stress $\sigma(x)$ moves into the specimen and in accordance with [4] there is an increase in the temperature of transition from blistering to flaking.

On the other hand, if there are two competing processes (point-defect diffusion, which expands the profile of $\sigma(x)$, and bubble motion, which moves the $\sigma(x)$ curve away from the surface), and if the first process predominates at a sufficiently high temperature, then one gets a step distribution of $\sigma(x)$ and the transition to a porous surface.
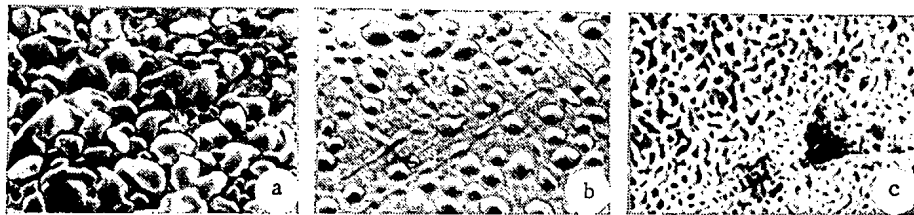
73

Fig. 1. Topography of nickel irradiated by helium ions in the presence of temperature gradient at various temperatures ($D = 10^{18}$ ion/cm^2); a) 400°C, $\nabla T = 50$ deg/cm ($\times 1000$); b) 710°C, $\nabla T = 70$ deg/cm ($\times 2000$); c) 810°C, $\nabla T = 70$ deg/cm ($\times 3000$).
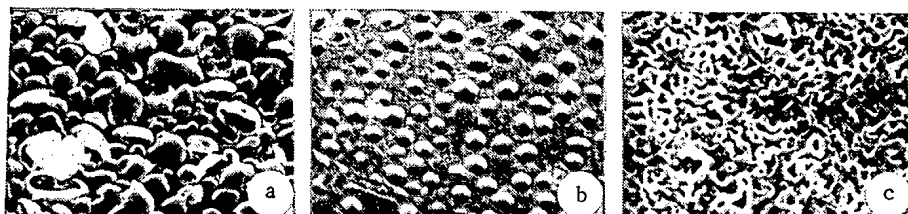

Fig. 2. Topography of nickel irradiated by helium ions with a homogeneous temperature distribution ($D = 10^{18}$ ion/cm^2) and temperatures of: a) 400°C; b) 600°C; c) 700°C. Magnification as in Fig. 1.

The temperature for transition from flaking to high-temperature blistering is less sensitive to the temperature gradient, because the bubble speed is small at the lower temperature.

Although a temperature gradient increases the temperature range in which blistering is observed, it does not, on the whole, substantially change the role of blistering in the erosion of the first wall of a fusion reactor.

LITERATURE CITED

1. V. M. Gusev et al., Prib. Tekh. Eksp., No. 4, 19 (1968).
2. V. M. Gusev et al., Preprint IAE-3133, Moscow (1979).
3. M. Risch, J. Roth, and B. Scherzer, in: Proc. Int. Symposium on Plasma Wall Interaction, Commission of the European Communities, Pergamon, New York (1977), p. 391.
4. A. Ryazanov and L. Maksimov, Rad. Effects, 54, 195 (1981).
5. Yu. V. Martynenko, Rad. Effects, 45, 93 (1979).
6. W. Wilson, H. Baskes, and C. Bisson, Phys. Rev., B13, 2470 (1976).
7. I. Eshelby, Solid-State Phys., 3, 79 (1956).

TAKING ACCOUNT OF THE BACKGROUND OF NATURAL NEUTRON RADIATION IN DETERMINING
THE COMPOSITION OF A MIXTURE OF FISSILE NUCLIDES FROM DELAYED NEUTRONS

B. P. Maksyutenko, A. N. Mironov,   UDC 539.107.574.336:621.039.54
V. S. Nesterenko, and Yu. F. Balakshev

The problem of suppressing the background from accompanying processes in recording ion-izing radiation arises fairly frequently. In determining the composition of a mixture of fis-sile nuclides in spent reactor fuel from the fall in the delayed-neutron flux [1], a pronounced background may be produced by instantaneous neutrons in the spontaneous fission of isotopes of plutonium, curium, californium, etc.

The physical properties of this radiation, which may be used to suppress the background, will be considered here. The delayed neutrons are isolated: they are randomly distributed over time. The distribution of fission events in spontaneous fission is also random, but neu-tron pairs, triads, etc., in a second, third, etc., appear at the same time. Therefore, if an apparatus is constructed from several detectors included in a coincidence circuit, and separate recordings are made of the individual neutrons in one channel, and dyads, triads, etc., in a second, third, etc., the count from delayed neutrons and the smallest fraction of the background will be recorded in the first channel. Taking into account that the probabil-ity density of the emission of a number of instantaneous neutrons is approximately described by a Gaussian [2], it may be estimated, e.g., for ^{252}Cf, that the number of neutron pairs is around seven times larger than the number of individual neutrons, while the number of triads is ~20 times larger, and the background may be considerably suppressed. For plutonium and curium isotopes these values will be lower but still appreciable. All the foregoing is valid if the efficiency of the detectors is close to 100%.

It is impossible to realize this means of suppressing the background with the detectors usually used for this purpose (gas proportional counters filled with ^{3}He or ^{10}BF$_3$), because of their low efficiency with respect to both instantaneous and delayed neutrons. To increase the efficiency, the detector unit is surrounded with polyethylene. Pairs, triads, etc. of instan-eous neutrons are desynchronized here because of the different delay times, and the background which they produce is determined by random coincidences. Therefore, in the given case, what should be considered is not suppression of the background, but taking it correctly into ac-count, i.e., determining it more accurately, which involves measuring it for a longer time.

A sharp increase in the efficiency of the apparatus causes another complication: count-ing errors due to multiple coincidences, which occur especially at the beginning of recording the intensity drop in the delayed-neutron flux. In this case, the use of a coincidence scheme proves useful. Thus, if all the detectors are connected to one input of the preamplifier with a count rate of ~40,000 sec (this may occur with a large number of fissile materials) and a resolution time $\tau = 5 \cdot 10^{-6}$ sec, the counting error is ~20%. If separate amplification chan-nels are used for each detector, however, and the channel outputs are fed to a multiple coin-cidence circuit, the true number of counts may be readily determined as

$$N = \sum_{k=1}^{m} k N_k,$$

where k is the channel number, and N_k the number of counts in it.

The detector of the system which we created consists of six proportional counters filled with ^{3}He to 15 atm* (Fig. 1). For each counter, separate amplification, discrimination, and pulse-formation channels are used, as shown in Fig. 2. Recording is performed in six chan-nels: in the first, single pulses are recorded; in the second, coincidences of two neutrons;
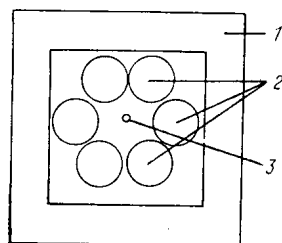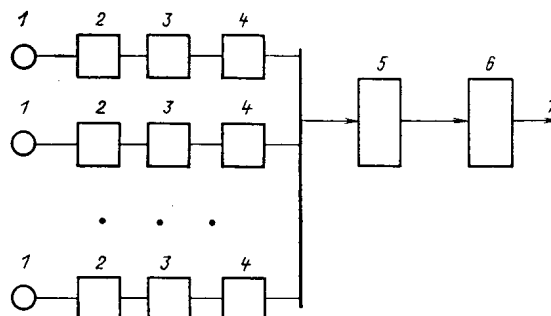
---

*1.5·10^6 Pa.

Fig. 1.

Fig. 2

Fig. 1. Experimental geometry: 1) polyethylene; 2) detector; 3) source.

Fig. 2. Structural diagram of the measurement system: 1) detectors; 2) preamplifier; 3) amplifier; 4) discriminator; 5) multiinput coincidence circuit; 6) multichannel counter; 7) physical measuring center (PMC).
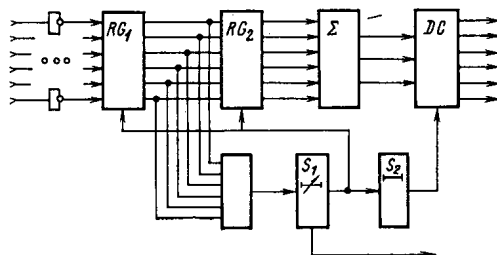

Fig. 3. Functional diagram of the multiinput coincidence circuit.

TABLE 1. Count Rate in Channels with Different Sources ($\tau = 5 \cdot 10^{-6}$ sec), sec^{-1}

Channel	^{252}Cf without moderator	^{252}Cf with moderator	Pu–Be with moderator
1	4353,7 ±2,6	23458 ±45	22751 ±52
2	85,6 ±1,4	8243 ±29	7806 ± 6
3	0,91±0,15	983,7±6,2	873 ±11
4	—	102,1±1,1	82,4± 0,2
5	—	4,13±0,24	8,2±0,2
6	—	—	—

etc. The channel of each counter is tuned so that pulses from all γ quanta of amplitude less than the amplitude of the superthermal neutrons are discriminated.

A functional diagram of the six-input coincidence circuit is shown in Fig. 3. Input pulses are passed through inverters to the register RG_1. Through the OR circuit, the first detector-signal coincidence reaching the apparatus triggers the first delay and formation circuit S_1, which produces the signal " gate-1." The delay of the latter with respect to the input signal is 0.2-5 µsec. From the leading edge of the gate-1 signal, the discharge corresponding to that input of the device to which the detector signals are fed during the time interval between the leading edge of the first detector signal and the leading edge of the gate-1 signal is passed to the second register RG_2 [3]. This interval is also the resolution time of the coincidence circuit.

The gate-1 signal also serves to trigger the second delay and formation system S_2 and to set the register in the initial state. From the end of this signal, the register is ready for a new cycle of operation. The intrinsic "dead" time of the coincidence circuit is determined by the duration of the gate-1 signal and is 50 nsec. The summator Σ, consisting of three 155IM2 microcircuits, ensures the summation of a number of units in the output code of the register RG_2. The binary code of the result of the gated decoder DC (155ID4) is transformed into positional code. Circuit S_2 produces the signal gate-2, delayed with respect to the signal gate-1 by the time necessary for compensation of the delay in the second register and summator.

76

nel counter [4], ensuring eight recounts in each channel and matching with the recording apparatus of the measurement center. The basic recount apparatus and information store employed is the working store of the measurement center, each cell of which acts as an individual recount circuit.

Table 1 gives the measurement results. The ratio of the count rate in the second channel to the count rate in the first for a system without a moderator is no more than 2%, while for a system with a moderator it is as much as 34%. In the third column of Table 1, the results of experiments with neutrons from a Pu—Be source are given. In this case, there is a random time distribution of the emitted neutrons, and the proportion of counts in the second channel with respect to the proportion in the first is as for a ^{252}Cf source with a moderator.

LITERATURE CITED

1. B. P. Maksyutenko, M. Z. Tarasko, and A. A. Shimanskii, At. Energ., 45, No. 1, 63 (1978).
2. V. P. Rudakov, At. Energ., 4, No. 3, 315 (1958).
3. E. Vinkler, V. M. Grebenyuk, and V. G. Zinov, Prib. Tekh. Eksp., No. 2, 109 (1979).
4. A. N. Mironov, V. S. Nesterenko, and S. I. Chubarov, in: Materials of an All-Union Conference on Automation of Scientific Research in Nuclear Physics [in Russian], Kiev (1976), p. 205.

USING THE VARIATIONAL METHOD OF CALCULATING PLASMA EQUILIBRIUM IN A TOKAMAK
FOR THE CONSISTENT SOLUTION OF PROBLEMS OF THE EVOLUTION OF EQUILIBRIUM
AND HEAT TRANSFER

V. K. Kolesnikov and V. D. Khait

UDC 621.039.61:533.9

Recent years have seen the development of methods of calculating plasma equilibrium in a tokamak based on reducing the two-dimensional Gred—Shafranov equilibrium equation to a system of ordinary differential equations for parameters determining the form and position of the magnetic surfaces (displacement, ellipticity, triangularity, etc. [1-4]). These methods allow the problems of heat and particle transfer and stability to be effectively combined with the problem of the evolution of equilibrium. The need for the correlation of these problems was noted in [1], where the basic principles of this process were considered.

In the present work, on the basis of the variational method of calculating equilibrium proposed in [2] and numerically realized for the model of "inscribed ellipses" [4], the results of combined solution of the problems of heat transfer and plasma equilibrium are given. With the aim of developing a scheme for the calculation and elucidation of the basic effects due to the mutual influence of transport phenomena and equilibrium, and also in view of the presently existing indeterminacy in the transfer coefficients, the tendency is to simplify the problem as much as possible in the part relating to transport phenomena.

The single-component model of a plasma with a single temperature of ions and electrons is used. Heat conduction with a constant coefficient ("Alcator scaling") is regarded as the only mechanism of heat loss. The only heat source considered is the power introduced in the plasma using a fast-atom injector, which is assumed to be uniformly distributed over the volume. The diffusion equation of the plasma is not considered, and the density is taken to be a specified quantity, constant over the cross section.

The equilibrium problem requires that the plasma pressure p and longitudinal current I be specified as a function of the surface ("radial") coordinate (taken in the form of the meridional cross-sectional area f of the given magnetic surface). In [1], the evolution of equilibrium was considered in connection with the diffusion of magnetic fluxes and the redistribution of the current, without taking account of the evolution of the pressure. In contrast to this, attention is concentrated here on the correlation of the evolution of equilibrium and heat transfer, and the current distribution is taken to be specified.

Neglecting convective terms, the mean heat-transfer equation over the magnetic surface [1] is as follows:

$$\frac{\partial \tau}{\partial t} = \frac{4}{R + fR'} \frac{\partial}{\partial f} \left(fRK \frac{\partial \tau}{\partial f} \right) + Q. \tag{1}$$

The units of length, time, and energy used here are $\sqrt{f_\Sigma}$ (f_Σ is the area of the boundary cross section), $3nf_\Sigma / 2\pi\varkappa$, energy, and $f_\Sigma j_0^2 / nc^2$ ($j_0 = I'|_{f-0}$; the prime denotes the derivative with respect to f), respectively; $3Q/2$ is the dimensionless power of the injector in the calculation for a single ion; $R(f)$, cylindrical coordinate of the center of the cross section of the given magnetic surface; and τ, dimensionless temperature associated with the "current beta"

as follows: $\beta_I = 2c^2 f_\Sigma \int_0^{f_\Sigma} \tau \, df / I^2 (f_\Sigma)$.

The coefficient K in Eq. (1) characterizes the influence of toroidality on the heat transfer associated with the shift and deformation of the magnetic surfaces, which are simultaneously isothermal surfaces

$$K = \frac{1}{4\pi f} \oint \frac{r}{R} |\nabla f| dl = \frac{\text{ch } \eta}{\pi} \times \int_0^\pi \frac{(1 + \sqrt{f/e^\eta \pi R^2} \cos \vartheta)(1 + \text{th } \eta \cos 2\vartheta) \, d\vartheta}{1 + 2 |\sqrt{\pi e^\eta f} R' \cos \vartheta - f\eta' \cos 2\vartheta}, \tag{2}$$

where the integral in the first part of the equation is taken along the contour of the cross section of the given magnetic surface. The second part of the equation corresponds to the model of inscribed ellipses with a semiaxis ratio e^η and depends explicitly on the functions $R(f)$, $\eta(f)$ determined by the equilibrium.

Equation (1) is solved with the boundary condition that the temperature must vanish at a certain specified (boundary) magnetic surface ($R = R_\Sigma$, $\eta = \eta_\Sigma$).

The following calculation scheme is used: From a specified initial distribution $\tau(f)$ — with specified $I(f)$ — the equilibrium is calculated, and the functions $R(f)$ and $\eta(f)$ are determined. After calculating K, Eq. (1) is solved, i.e., the new (in terms of the time step Δt) distribution $\tau(f)$; from this distribution, the equilibrium is again determined and then Eq. (1) is solved, etc.

In the evolution process the energetic lifetime is determined, taking the dimensionless form

$$\tau_E = \int_0^1 \tau (R + fR') \, df \bigg/ \left[QR_\Sigma - \frac{\partial}{\partial t} \int_0^1 \tau (R + fR') \, df \right]. \tag{3}$$

Two series of calculations are performed. In the first case, with the injector "switched off," the initial distribution $\tau(f)$ and β_I are specified and, in the first time step, the lifetime and the influence on it of the character of the distributions $\tau(f)$ and $I(f)$ are determined, as well as β_I at various aspect ratios. The results of calculating τ_E, referred to τ_0, with $\beta_I = 0$ and an aspect ratio $A = \sqrt{\pi R^2 e^\eta \Sigma / f_\Sigma} \gg 1$ are shown in Fig. 1 as a function of β_I / A. For different current and pressure distributions, from $I' = \text{const}$, $p' = \text{const}$ to strongly peaked distributions with an error of up to 5%, all the points lie close to curve 1. The points for the case $e^\eta \Sigma = 1.5$ lie as close to this curve. It is evident that there is a pronounced drop in τ_E when $\beta_I \gtrsim A$.

The dependence of the asymmetry coefficient of the heat flux at the boundary, i.e., the flux-density ratio at the external outline of the torus ($\vartheta = 0$) and at the internal outline ($\vartheta = \pi$) on β_I / A is also shown in Fig. 1. Points for different A and the current and pressure distributions again lie close to a single curve (curve 2).

In the second series of calculations, the approach to steady thermal conditions (from an initial state with a low temperature) is traced for various values of the injector power Q and current distribution. The dependence of τ_E (curve 1) and β_I (curve 2) in steady conditions on the normalized injector power $Qj_0^2 f_\Sigma / I_0^2$ is shown in Fig. 2 for two current distributions.

78
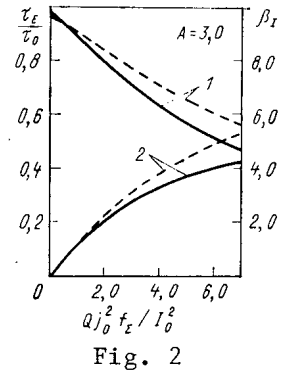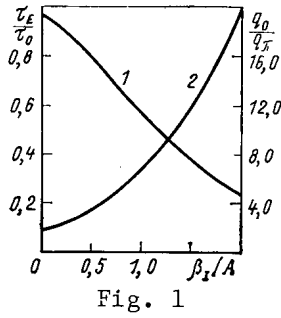
Fig. 1   Fig. 2

Fig. 1. Dependence of the energetic lifetime and asymmetry coefficient of the heat flux on β_I/A.

Fig. 2. Dependence of the energetic lifetime and β_I in steady conditions on the normalized injector power for I' = const (continuous curves) and $I = 5I_0 f/(1 + 4f)$ (dashed curves).

Note that the numerical problem of the approach to steady conditions, requiring multiple calculations of the equilibrium configuration, takes about 1 min on the BESM-6 computer. It should also be said that the model of inscribed ellipses does not adequately describe equilibrium at a large value of β_I close to limiting with respect to equilibrium. The limiting values of β at the level 2A obtained in calculations for this model are evidently too high.

LITERATURE CITED

1. L. E. Zakharov and V. D. Shafranov, Preprint IAE-3075, Moscow (1968).
2. V. D. Khait, Fiz. Plazmy, 6, 871 (1980).
3. L. Lao, S. Hirshman, and R. Wieland, Phys. Fluids, 24, 1431 (1981).
4. V. Khait and V. Kolesnikov, in: Proceedings of the Tenth European Conference on Controlled Fusion and Plasma Physics, Vol. 1, Rep. B-8, Moscow (1981).

79

COUNTER WITH A PLASTIC SCINTILLATOR FOR MEASURING HIGH-ENERGY NEUTRON

SPECTRA

V. E.   Aleinikov, M. M. Komochkov,   UDC 539.1.83
A. V. Solodilov, and G. N. Timoshenko

The methods and means which are presently employed for dosimetry and protective measures on high-energy accelerators and for measuring the energy distribution of neutrons are characterized either by low sensitivity (threshold detectors [1]) or by a small information content at high energies (Bonner spectrometer [2-4]) or they are designed for a specific direction of neutrons only [5]. We describe below a method of measuring the energy spectra of neutrons in the energy range 15-500 MeV; the method is basically free of the shortcomings listed above.

The efficiency of a scintillation detector S_n for neutrons in the energy range 5-500 MeV was calculated with the Monte Carlo method with the program of [4] (based on [6-10]) for various energy thresholds T of recording in units of the electron energy. A plastic polystyrene scintillator with a diameter and height of 120 mm was used as the detector for the neutron counter S_n. The neutron counter [11] was surrounded by a protective scintillator $\overline{S}$ in the form of a cup viewed by another photomultiplier connected in anticoincidence with the counter S_n to suppress the recording of the charged component of the radiation field. The measurements were reduced to create the instrument-induced spectrum set resulting from events of the form $S_n + \overline{S}$ in an analyzer, the scale of which was calibrated in units of electron energy. The method of determining the neutron spectra was based upon measurements of counter readings at various thresholds T_i of recording. A quantity of the form

$$N(T_i) = \sum_{j \geqslant l_i} n_j$$

is used for the readings of the neutron counter, where n_j denotes the number of counts in the j-th analyzer channel, and l_i denotes the analyzer channel number corresponding to the threshold T_i (i = 1, 2, ..., m). The neutron spectrum $\varphi(E)$ can be determined by solving the following Fredholm integral equation of the first kind:

$$N(T_i) + \sigma N(T_i) = \int_0^{E_{max}} \varepsilon(E, T_i) \Phi(E) \, dE. \qquad (1)$$

The notation is interpreted as follows: $\delta N(T_i)$ is the error of a measurement $N(T_i)$; $\varepsilon(E, T_i)$, energy dependence of the neutron recording efficiency of the counter S_n with the threshold T_i; and E_{max}, maximum neutron energy.

Equation (1) can be numerically solved on a computer with, say, the statistical regularization method of [12]. In order to check the possibilities offered by the method, several qualitatively different spectra were restored. The procedure is as follows. The selected test spectrum $\Phi_t(E)$ was analytically given and the values

$$N_t(T_i) = \int_0^{E_{max}} \varepsilon(E, T_i) \Phi_t(E) \, dE \qquad (2)$$

were calculated. Thereafter Eq. (1) was solved for $\Phi(E)$ at

$$N(T_i) = N_t(T_i).$$

The $\delta N(T_i)/N(T_i)$ values were assumed as 0.05, 0.10, and 0.15. Figure 1 shows the results of a comparison for test spectra of the form

---

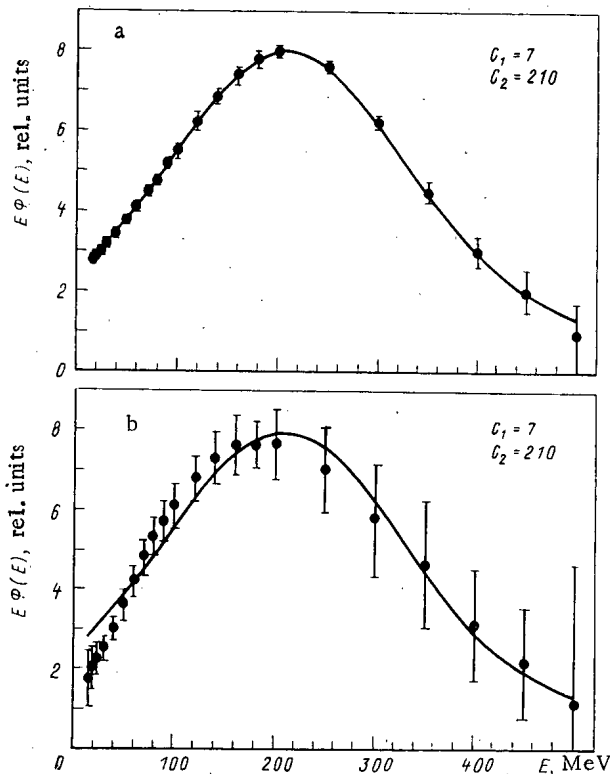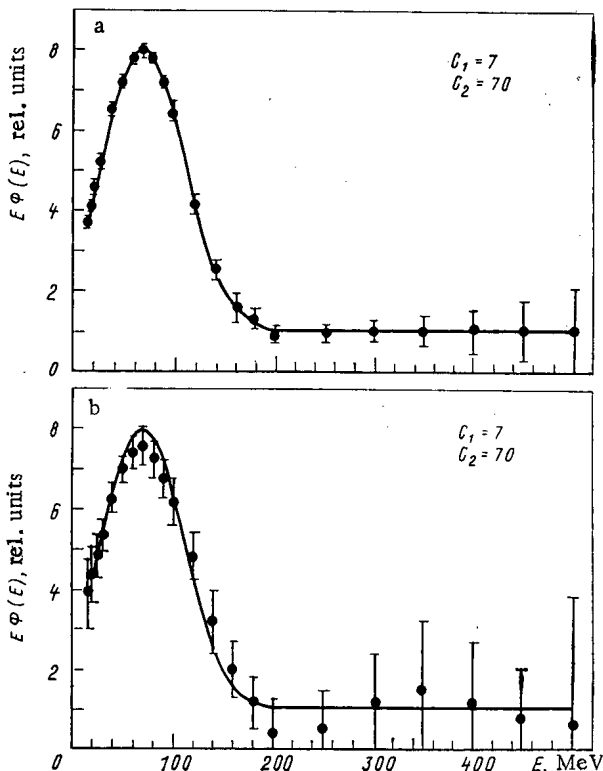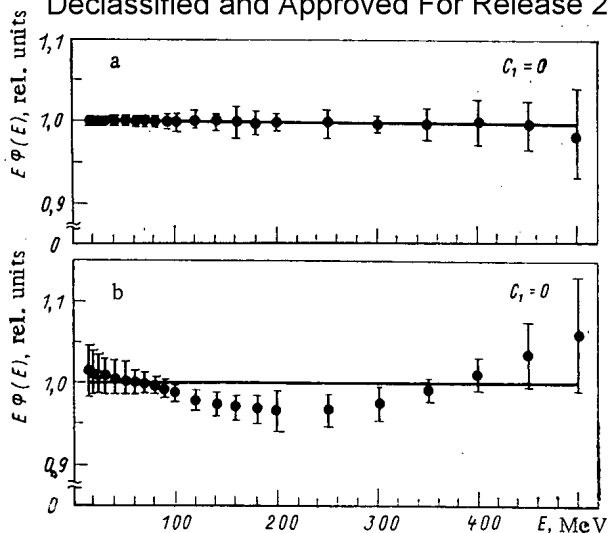0038-531X/83/5401- 0080$07.50   © 1983 Plenum Publishing Corporation

Fig. 1. Results of restoring the neutron test spectra given by the function of·Eq. (3) for $\delta N(T_i)/N(T_i)$ = 0.15: a) counter readings not randomized; b) counter readings randomized (g = 0.15).

$$\Phi_t(E) = \left\{ 1 + C_1 \exp\left[-\left(\frac{E - C_2}{EC_3} \right)^2 \right] \right\} E^{-1}, \tag{3}$$

where C_1 = 0 and 7, C_2 = 70 and 210, and C_3 = 0.8. In order to verify the stability of the solution, the same spectra were restored with randomized $\tilde{N}_t(T_i)$ and $\delta\tilde{N}_i(T_i)$ values which were determined from a recurrence relation simulating the correlation between the various $N(T_i)$ values. The correlation of $N(T_i)$ results from the method of defining $N(T_i)$ through the instrument-dependent spectrum of the analyzer:

$$\left\{ \begin{array}{l} \tilde{N}_t(T_m) = N_t(T_m) + \rho_m g N_t(T_m); \\ \tilde{N}_t(T_i) = \tilde{N}_t(T_{i+1}) + N_t(T_i) - \\ \quad - N_t(T_{i+1}) + \rho_i g [N_t(T_i) - N_t(T_{i+1})]; \end{array} \right.$$

81

$$\begin{cases} \delta\widetilde{N}_t(T_m) = g\widetilde{N}_t(T_m); \\ \delta\widetilde{N}_t(T_i) = V\overline{\delta^2\widetilde{N}_i(T_{i+1}) + g^2[\widetilde{N}_t(T_i) - \widetilde{N}_t(T_{i+1})]^2}; \end{cases}$$

$$i = m-1, \; m-2 \ldots 2, \; 1,$$

where ρ_i denotes the values of a random quantity with a normal distribution, average zero, and dispersion one; we have $|\rho_i| \leqslant 1$; and g = 0.05, 0.10, and 0.15. A comparison of the test spectra with the restored spectra has shown that usually the calculated spectra correctly describe the given test spectra within the error limits of the restoring method. Therefore, there is reason to assume that the proposed method can be used for neutron spectrometry in scattered radiation fields and at neutron energies of 15 to 500 MeV. The upper limit of the energy range is given by the lack of accuracy in calculating the efficiency of the neutron detector at neutron energies above the threshold of meson generation and also by the form of the response function at high energies. Estimates show that for neutron energies below 500 MeV, the contribution of π mesons, generated in the scintillator, to the neutron detector efficiency does not exceed 5%.

LITERATURE CITED

1. V. E. Aleinikov et al., JINR R-16-81-102, Dubna (1981).
2. R. Bramlett, Nucl. Instrum. Meth., 9, 1 (1960).
3. V. E. Aleinikov et al., JINR R-16-8176, Dubna (1974).
4. V. E. Aleinikov et al., JINR R-16-9870, Dubna (1976).
5. K. O'Brien and I. McLaughlin, Nucl. Instrum. Methods, 32, 63 (1965).
6. N. Stanton, COO-1545-92 (1971).
7. R. Edelstein et al., Nucl. Instrum. Methods, 100, 355 (1972).
8. D. Hermsdorf et al., Nucl. Instrum. Methods, 107, 259 (1973).
9. R. De Leo et al., Nucl. Instrum. Methods, 119, 559 (1974).
10. M. McNaughton et al., Nucl. Instrum. Methods, 116, 25 (1974).
11. V. E. Aleinikov et al., JINR, R-16-80-453, Dubna (1980).
12. L. S. Turovtseva et al., Preprint Inst. Prikl. Mat. (Preprint Inst. of Applied Mathematics), No. 30 (1971).

MEASUREMENT TECHNIQUES
Izmeritel'naya Tekhnika
Vol. 25, 1982 (12 issues) $400

MECHANICS OF COMPOSITE MATERIALS
Mekhanika Kompozitnykh Materialov
Vol. 18, 1982 (6 issues) $330

METAL SCIENCE AND HEAT TREATMENT
Metallovedenie i Termicheskaya Obrabotka Metallov
Vol. 24, 1982 (12 issues) $420

METALLURGIST
Metallurg
Vol. 26, 1982 (12 issues) $435

PROBLEMS OF INFORMATION TRANSMISSION
Problemy Peredachi Informatsii
Vol. 18, 1982 (4 issues) $320

PROGRAMMING AND COMPUTER SOFTWARE
Programmirovanie
Vol. 8, 1982 (6 issues) $135

PROTECTION OF METALS
Zashchita Metallov
Vol. 18, 1982 (6 issues) $380

RADIOPHYSICS AND QUANTUM ELECTRONICS
Izvestiya Vysshikh Uchebnykh Zavedenii, Radiofizika
Vol. 25, 1982 (12 issues) $400

REFRACTORIES
Ogneupory
Vol. 23, 1982 (12 issues) $380

SIBERIAN MATHEMATICAL JOURNAL
Sibirskii Matematicheskii Zhurnal
Vol. 23, 1982 (6 issues) $495

SOIL MECHANICS AND FOUNDATION ENGINEERING
Osnovaniya, Fundamenty i Mekhanika Gruntov
Vol. 19, 1982 (6 issues) $380

SOLAR SYSTEM RESEARCH
Astronomicheskii Vestnik
Vol. 16, 1982 (4 issues) $275

SOVIET APPLIED MECHANICS
Prikladnaya Mekhanika
Vol. 18, 1982 (12 issues) $400

SOVIET ATOMIC ENERGY
Atomnaya Énergiya
Vols. 52–53 (12 issues) $440

SOVIET JOURNAL OF GLASS PHYSICS AND CHEMISTRY
Fizika i Khimiya Stekla
Vol. 8, 1982 (6 issues) $175

SOVIET JOURNAL OF NONDESTRUCTIVE TESTING
Defektoskopiya
Vol. 18, 1982 (12 issues) $485

SOVIET MATERIALS SCIENCE
Fiziko-khimicheskaya Mekhanika Materialov
Vol. 18, 1982 (6 issues) $345

SOVIET MICROELECTRONICS
Mikroélektronika
Vol. 11, 1982 (6 issues) $195

SOVIET MINING SCIENCE
Fiziko-tekhnicheskie Problemy Razrabotki Poleznykh Iskopaemykh
Vol. 18, 1982 (6 issues) $420

SOVIET PHYSICS JOURNAL
Izvestiya Vysshikh Uchebnykh Zavedenii, Fizika
Vol. 25, 1982 (12 issues) $400

SOVIET POWDER METALLURGY AND METAL CERAMICS
Poroshkovaya Metallurgiya
Vol. 21, 1982 (12 issues) $435

STRENGTH OF MATERIALS
Problemy Prochnosti
Vol. 14, 1982 (12 issues) $495

THEORETICAL AND MATHEMATICAL PHYSICS
Teoreticheskaya i Matematicheskaya Fizika
Vols. 50–53, 1982 (12 issues) $380

UKRAINIAN MATHEMATICAL JOURNAL
Ukrainskii Matematicheskii Zhurnal
Vol. 34, 1982 (6 issues) $380

Send for Your Free Examination Copy

RUSSIAN JOURNALS IN THE PHYSICAL AND MATHEMATICAL SCIENCES

AVAILABLE IN ENGLISH TRANSLATION

ALGEBRA AND LOGIC
Algebra i Logika
Vol. 21, 1982 (6 issues) $270

ASTROPHYSICS
Astrofizika
Vol. 18, 1982 (4 issues) $320

AUTOMATION AND REMOTE CONTROL
Avtomatika i Telemekhanika
Vol. 43, 1982 (24 issues) issues) $495

COMBUSTION, EXPLOSION, AND SHOCK WAVES
Fizika Goreniya i Vzryva
Vol. 18, 1982 (6 issues) $345

COSMIC RESEARCH
Kosmicheskie Issledovaniya
Vol. 20, 1982 (6 issues) $425

CYBERNETICS
Kibernetika
Vol. 18, 1982 (6 issues) $345

DIFFERENTIAL EQUATIONS
Differentsial'nye Uravneniya
Vol. 18, 1982 (12 issues) $395

DOKLADY BIOPHYSICS
Doklady Akademii Nauk SSSR
Vols. 262–267, 1982 (2 issues) $145

FLUID DYNAMICS
Izvestiya Akademii Nauk SSSR,
Mekhanika Zhidkosti i Gaza
Vol. 17, 1982 (6 issues) $380

FUNCTIONAL ANALYSIS AND ITS APPLICATIONS
Funktsional'nyi Analiz i Ego Prilozheniya
Vol. 16, 1982 (4 issues) $320

GLASS AND CERAMICS
Steklo i Keramika
Vol. 39, 1982 (6 issues) $460

HIGH TEMPERATURE
Teplofizika Vysokikh Temperatur
Vol. 20, 1982 (6 issues) $400

HYDROTECHNICAL CONSTRUCTION
Gidrotekhnicheskoe Stroitel'stvo
Vol. 16, 1982 (12 issues) $305

INDUSTRIAL LABORATORY
Zavodskaya Laboratoriya
Vol. 48, 1982 (12 issues) $400

INSTRUMENTS AND EXPERIMENTAL TECHNIQUES
Pribory i Tekhnika Eksperimenta
Vol. 25, 1982 (12 issues) $460

JOURNAL OF APPLIED MECHANICS AND TECHNICAL PHYSICS
Zhurnal Prikladnoi Mekhaniki i Tekhnicheskoi Fiziki
Vol. 23, 1982 (6 issues) $420

JOURNAL OF APPLIED SPECTROSCOPY
Zhurnal Prikladnoi Spektroskopii
Vols. 36–37 (12 issues) $420

JOURNAL OF ENGINEERING PHYSICS
Inzhenerno-fizicheskii Zhurnal
Vols. 42–43, 1982 (12 issues) $420

JOURNAL OF SOVIET LASER RESEARCH
A translation of articles based on the best Soviet research in the field of lasers
Vol. 3, 1982 (4 issues) $95

JOURNAL OF SOVIET MATHEMATICS
A translation of Itogi Nauki i Tekhniki and Zapiski Nauchnykh Seminarov Leningradskogo Otdeleniya Matematicheskogo Instituta im. V. A. Steklova AN SSSR
Vols. 18–20, 1982 (18 issues) $680

LITHOLOGY AND MINERAL RESOURCES
Litologiya i Poleznye Iskopaemye
Vol. 17, 1982 (6 issues) $420

LITHUANIAN MATHEMATICAL JOURNAL
Litovskii Matematicheskii Sbornik
Vol. 22, 1982 (4 issues) $205

MAGNETOHYDRODYNAMICS
Magnitnaya Gidrodinamika
Vol. 18, 1982 (4 issues) $325

MATHEMATICAL NOTES
Matematicheskie Zametki
Vols. 31–32, 1982 (12 issues) $400